2D/3D ALUMINA NANOPLATELET SLIT-PORE MEMBRANES.

Yiting He

A thesis submitted in partial fulfillment of the requirements for the

Master's in Applied Science degree in Chemical Engineering

Department of Chemical and Biological Engineering

Faculty of Engineering

University of Ottawa

Statement of Contributions and Collaborators

I hereby declare that I am the sole author of this thesis. I performed all the experiments and the data analysis. All the preparation work, sample analyses, data analysis and some of the permeability experiments were performed by me under the supervision and guidance of Dr. André Y. Tremblay. I have written the chapters contained in this thesis.

Some of the twinned alumina nanosheets were synthesized by Mohamad Elian (Co-op). He also performed some of the permeability experiments presented in Chapter 5.

Dr. Andre Y. Tremblay supervised this thesis project and provided continual guidance and support. He also made many editorial comments and corrections to the written work presented. His day-to-day guidance, discussion and never ending support have resulted in tremendous improvements to the thesis.

Abstract

Oil pollution and spills cause serious damage to marine ecosystems and coastal environments. Currently, oily waters recuperated form a spill must be shipped onshore for treatment. This limits the volume of water that can be treated during a spill. There is a need to develop technologies to treat oily waters below 15 ppm (parts per million) at the site of the spill. Synthetic membrane technologies are widely used in water treatment and purification. They can offer an on-site solution to contaminated oily water treatment in oil production and spills.

The suitability of a membrane for use in this application is determined by the type of material used in its fabrication. Compared to polymeric membranes, inorganic membranes are inert to microbiological degradation, offer high chemical and thermal resistance, and can easily be backflushed and cleaned once fouled. However, inorganic membranes consisting of metal oxides are heavier and more expensive than polymeric membranes, due to their bulky and brittle ceramic support layers. This limits their application when the overall weight of a process unit is of concern.

A newly developed 2D/3D material, named twinned alumina nanosheets (TAN), has recently been used to make dynamic membranes. The nanoplatelets forming TAN have a length of 4 µm, a width of 1 µm, and a thickness of 100 nm. They have a very high permeability, a 0.2 µm-pore size and a porosity up to 88% due to their low nanosheet volume. These unique characteristics make TAN a very promising material to form membrane selective layers. However, they must be supported on a very open layer in order to take advantage of their high porosity. In this work, a composite membrane was produced with a selective layer of 2D/3D alumina nanoplatelets deposited onto stainless steel meshes and ceramic supports. The structure of the TAN in the selective layer was reinforced with binders. The main objective of this work was to verify the adhesion of the TANs onto the support.

The crystallization of TAN was optimized to obtain an open 2D/3D structure. This structure was then deposited on a stainless-steel mesh. The mesh was pretreated by electrochemical etching to achieve a re-entrant surface. The mesh was immersed in an etching solution and placed parallel to a conductive graphite plate under a constant electric potential of 5V for 4 min.

Aqueous solutions of silica sol and colloidal silver were tested as binding agents. They were deposited on the mesh with TAN and sintered for 4 hrs. Experiments were performed on testing stainless steel meshes with different opening sizes and comparing different calcination temperatures. The best sintering temperature was 800°C for a mesh with an opening size of 35µm.

The synthesized membrane was challenged with a suspension of 10 ppm bentonite clay at a constant pressure of 100 mbar. The integral structure of a TAN membrane produced with a 2.5wt% silica binder was maintained after backflushing. The 2.5wt% silica membrane had a high flux and the particle filtration process for this membrane was modelled as pore constriction and intermediate blocking, indicating that backflushing provided the deep cleaning of pores. According to the SEM images, the 2.5wt% silica membrane preserved the integral structure of the TAN, while the pores tended to fill with silica at higher silica concentrations. The effective pore size of the 2.5wt% silica membrane was estimated to be the smallest, which is approximately 0.53 µm. The 7.5wt% silica membrane had half the permeate flux of the other membranes, because of the high concentration of binder filling the pores of the TAN selective layer. The SiO_2 binder had a positive effect in reinforcing the TAN particles.

The flux of the membrane did not increase after backflushing indicating that the selective layer of the membrane was securely bound to the stainless steel mesh. The membrane exhibited flux decline between backflushings indicating that particles were retained on its surface. SEM images

taken after the filtration showed that this membrane completely released bentonite particles form its pores.

Tests were also performed with a membrane having two TAN coatings on the wire mesh. This reduced the flux but did not improve the retention of fine particles. Colloidal silver was found to be a poor binding agent as particles were released particles from its selective layer. Silica was a highly successful binding agent while colloidal silver was not. TAN was also successfully deposited onto ceramic supports. It was also retained on top of the membrane after backflushing.

The results of this work demonstrate that TANs reinforced and bound with silica are a promising type of material to form membrane selective layers. These layers have an open pore structure with a three-dimensional channel connectivity on both stainless steel and ceramic supports. The selective layer was successfully bound to the stainless steel supports. If the pore size of this membrane were to be reduced, it would meet the requirements for use at the site of an oil spill to treat contaminated waters as it does not need the heavier supports found in traditional ceramic membranes.

Résumé

La pollution et les déversements d'hydrocarbures causent de graves dommages aux écosystèmes marins et aux environnements côtiers. À l'heure actuelle, les eaux huileuses récupérées d'un déversement doivent être expédiées à terre pour leur décontamination. Ceci limite le volume d'eau contaminé qui peut être traité. Il est nécessaire de développer des technologies permettant de traiter les eaux huileuses en dessous de 15 ppm (parties par million) sur le site du déversement. Les technologies membranaires sont largement utilisées dans le traitement et la purification de l'eau.

La possibilité de se servir d'une membrane dans cette application est déterminée par les matériaux utilisés dans sa fabrication. Comparées aux membranes polymères, les membranes inorganiques sont inertes vis-à-vis de la dégradation microbiologique, offrent une résistance chimique et thermique élevée et peuvent facilement être rincées et nettoyées une fois encrassées. Cependant, les membranes inorganiques constituées d'oxydes métalliques sont plus lourdes et plus coûteuses que les membranes polymères, en raison de leurs couches de support en céramique volumineuses et cassantes. Cela limite leur application lorsque le poids total d'une unité de traitement est préoccupant.

Un matériau 2D/3D récemment développé, appelé TAN (Twinned Alumina Nanosheets), a récemment été utilisé dans la formation de membranes dynamiques. Les nano-plaquettes formant les TAN ont une longueur de 4 µm, une largeur de 1 µm et une épaisseur de 100 nm. Ils ont une très haute perméabilité, une taille de pores de 0,2 µm et une porosité allant jusqu'à 88% en raison du faible volume des nanofeuilles. Ces caractéristiques uniques font du TAN un matériau très prometteur pour la formation de couches sélectives de membranes. Cependant, ils doivent être déposes sur une couche très ouverte afin de tirer parti de leur grande porosité. Au cours de ce travail, une membrane composite a été réalisée avec une couche sélective de nanoplaques

d’alumine 2D / 3D (TAN) déposées sur deux types de supports; des mailles en acier inoxydable et des supports en céramique. La structure du TAN dans la couche sélective a été renforcée avec des liants. L'objectif principal de ce travail était de vérifier l'adhérence des TAN sur le support.

La cristallisation des TAN a été optimisée pour obtenir une structure 2D/3D ouverte. Cette structure a ensuite été déposée sur un treillis en acier inoxydable. Les mailles ont été prétraitées pour obtenir une surface réentrante. Le maillage a été immergé dans une solution de gravure et placé parallèlement à une plaque de graphite conductrice sous un potentiel électrique constant de 5 V pendant 4 min.

Des solutions aqueuses de sol de silice et d’argent colloïdal ont été testées en tant que liants. Ils ont été déposés sur la maille et frittés pendant 4 heures. Des expériences ont été effectuées sur des mailles en acier inoxydable avec différentes tailles d’ouverture et températures de calcination. La meilleure température de frittage était de 800 ° C pour un treillis ayant une taille d'ouverture de 35 µm.

La membrane synthétisée a été mise à l’essai avec une suspension de 10 ppm d'argile bentonite à une pression constante de 100 mbar. La structure intégrale de la membrane couche de TAN produite avec un liant à 2,5wt% de silice a été maintenue après les tests de perméabilité. La structure 3D poreuse a tendance à se remplir de silice à des concentrations de silice supérieures à 2,5wt%. La taille effective des pores de la membrane produite avec 2,5wt% de liant de silice a été estimée à 0,53 µm. Le flux de la membrane n'a pas augmenté après le rinçage, indiquant que la couche sélective de la membrane était liée de manière sûre au maillage en acier inoxydable. La membrane présentait un déclin de flux entre les rinçages indiquant que des particules étaient

retenues à sa surface. Les images au microscope à balayage prises après la filtration ont montré que cette membrane libère complètement les particules de bentonite de ses pores.

Des essais ont également été réalisés avec une membrane comportant deux revêtements TAN sur le treillis métallique. Cela réduit le flux mais n'améliore pas la rétention des particules fines. L'argent colloïdal s'est avéré être un agent de liaison médiocre car des particules sont libérées de sa couche sélective. La silice était un liant très efficace, contrairement à l'argent colloïdal. Le TAN a également été déposé avec succès sur des supports en céramique. Il est également resté sur la membrane après le rinçage à contre-courant.

Les résultats de ce travail démontrent que les TAN renforcés avec un liant de silice sont un type de matériau prometteur pour former des couches sélectives, avec des structures à pores ouverts possédant une connectivité de canal tridimensionnelle, sur des supports en acier inoxydable et en céramique. La couche sélective a été liée avec succès au support en acier inoxydable. Si la taille des pores de cette membrane devait être réduite, elle pourrait être utilisée sur le site d'un déversement d'hydrocarbures pour traiter les eaux contaminées car elle ne nécessite pas les supports plus lourds que l'on trouve dans les membranes de céramique traditionnelles.

Acknowledgements

I would like to express my great gratitude to Dr. Andre Y. Tremblay for his continuous guidance, advice and support throughout my research.

I would also like to thank Franco Ziroldo, Gerald Nina and James Macdermid for technical assistance during the experiments.

I am grateful to Mohamad Elian, Xinlong Chen, Xuewei Meng, and all my colleagues in the faculty for their support.

Nomenclature

Abbreviations

ACS	Acidic Colloidal Silica
BCS	Basic Colloidal Silica
BSCF	$Ba_{0.5}Sr_{0.5}Co_{0.8}Fe_{0.2}O_{3-\delta}$
CFV	Cross Flow Velocity
CGO	$Ce_{0.9}Gd_{0.1}O_{1.95-\delta}$
CTAB	Cetyl Trimethyl Ammonium Bromide
DE	Diatomaceous Earth
DM	Dynamic Membranes
FR	Fouling Resistance
GS	Gas Separation
HPC	Hydroxypropyl Cellulose
Lmh	Liter/m^2/h
LSCF	$La_{0.6}Sr_{0.4}Co_{0.2}Fe_{0.8}O_{3-\delta}$
MF	Microfiltration
NCS	Neutral Colloidal Silica
NF	Nanofiltration
PDMS	Poly(dimethylsiloxane)
PEEK	Polyether Ether Ketone
PEG	Polyethylene Glycol
ppm	Parts per million

PVA	Polyvinyl Alcohol
PVB	Polyvinyl Butyral
RMSE	Root Mean-Squared Error
RO	Reverse Osmosis
SEM	Scanning Electron Microscope
SS	Stainless-steel
TAN	Twinned Alumina Nanoplates
TMP	Transmembrane Pressure
UF	Ultrafiltration
UHPC	Ultra-high-performance Concrete

Symbols

Ft	Feed turbidity
h	Half-width of the slit pore
J_V	Filtrate Flux Through the Clean Membrane
J_0	Initial Filtrate Flux Through the Clean Membrane
K_{block}	Constant in complete blocking model
K_{cake}	Constant in cake filtration model
$K_{constriction}$	Constant in pore constriction model
K_{inter}	Constant in intermediate blocking model
L_p	Hydraulic permeability
Pt	Permeate turbidity

R	Radii of cylindrical pore
wt	Weight

Greek Letters

δ_m	Thickness of the membrane
μ	Viscosity of solution
ε	Membrane porosity

Table of Contents

List of Figures

List of Tables

1 Introduction and literature review

1.1 Introduction and objectives

Oil pollution and spills can cause serious damage to wildlife, marine ecosystems and coastal environments. This form of pollution originates from routine shipping, oil field wastewaters from production operations, or oil spills [1]. Oil spills can have severe environmental, ecological and economic consequences. Cleanup and recovery from an oil spill is difficult and depends upon many factors, such as the temperature of the water and the type and the location of the spill. The accident may take weeks, months or years to clean up. However, current large-scale technologies can only treat spilled oil down to the separation obtained from the physical oil/water interface concentration of 15 ppm. The discharge concentration for oil in Canadian waters ranges from 5 to 15 ppm [2]. Currently, oily waters recuperated from a spill must be shipped onshore for treatment. There is a need to develop technologies to treat oil spills on-site. The ability of current technologies to treat large volumes of contaminated water below 15 ppm on-site is very limited.

Synthetic membrane technologies offer a solution to the problems of on-site contaminated water treatment in oil production and spills. In such wastewater, oil is often found in the form of oil droplets, with sizes ranging from 1-40 microns. Membranes are widely used for liquid separation purposes. They can be defined as a semi-permeable barrier, which selectively allows for the passage of one or more components in a liquid mixture. The degree of selectivity of a membrane depends on membrane pore size. Typically, pressure-driven membranes are classified according to their application or characteristic pore size, including microfiltration (MF), ultrafiltration (UF), nanofiltration (NF) and reverse osmosis (RO) membranes [3]. MF and UF are low pressure-driven processes in which the physical separation of the different-sized feed components is achieved via

a sieving mechanism across the membrane with a specific pore size. Various membrane materials are available for MF/UF processes, and the choice of the membrane material affects the reliability and sustainability of the filtration process.

Ceramic membranes are membranes made from inorganic materials (such as alumina, titania, zirconia oxides, silicon carbide or some glassy materials) and are used in potable water production, food and dairy industry, chemical industry and water purification applications [4]. Ceramic membranes generally consist of three layers. The top layer or selective layer has the smallest pore size and performs the separation. The bottom layer is the microporous support layer which forms the major part and provides a high mechanical strength for the membrane. The intermediate layer has a pore size in between those of top layer and support layer. Commercial ceramic membranes for MF/UF processes consist mainly of α-Al_2O_3 as the substrate and α-Al_2O_3, TiO_2 or ZrO_2 as the selective separation layer [5]. Compared to polymeric membranes, inorganic membranes are inert to microbiological degradation, offer high chemical and thermal resistance, can easily be back flushed and cleaned once fouled. However, inorganic membranes consisting of metal oxides are heavier, more fragile and expensive than polymeric membranes, due to their bulky and brittle ceramic support layers. This limits their use when the overall weight of a process unit is of concern. They must be handled with care and the choice of housing, sealing and shipping should be carefully considered. Moreover, for membrane cleaning purpose, backflushing is usually applied in which the flow of permeate is reversed under pressure by applying twice the flux that is used during filtration [4]. Backflushing is preferred over forward and chemical flushing due to its capability in removing adsorbed particles in the membrane pores without leaving chemical pollutants behind. The extent of backflushing is limited to the binding of the successive layers forming the membrane [6]. Therefore, it is important to find alternative membrane materials which serve similar purposes

as the ceramic membranes but are able to maintain high mechanical stability, withstand high backflushing rates, and are inexpensive to fabricate.

The microstructure across the membrane cross-section is a key property that dictates the performance and usability of a membrane for certain applications. A ceramic membrane can be categorized into symmetric and asymmetric structures [4]. A symmetric membrane has a uniform pore size and porosity throughout its cross-section whereas an asymmetric membrane does not. Ceramic membranes usually have an asymmetric structure [7]. For MF and UF processes, asymmetric membranes consisting of a thin skin layer on top of a porous sub-layer are desired. The porous sub-layer acts to provide adequate mechanical strength. This type of structure combines the high selectivity of the skin layer with good permeation fluxes. An asymmetric membrane can be integral or made of several layers known as a composite. The top and porous layers of an integral asymmetric membrane are normally made of the same material, and for composite membranes the top skin layer and the porous sub-layer can be made of different materials.

A membrane support provides mechanical strength to the top selective layer to withstand the stress induced by the pressure difference applied across the membrane during filtrate flow, and it should sustain high flow capacity at the same time. Different types of materials have been used in the fabrication of membrane supports including MgO, Al_2O_3, ZrO_2, CGO ($Ce_{0.9}Gd_{0.1}O_{1.95-\delta}$), BSCF ($Ba_{0.5}Sr_{0.5}Co_{0.8}Fe_{0.2}O_{3-\delta}$), LSCF ($La_{0.6}Sr_{0.4}Co_{0.2}Fe_{0.8}O_{3-\delta}$), metal and so on. The configuration of the support layer can be tubular, flat sheet, monolithic or hollow fiber [8]. The selective layer of the membrane typically faces the feed channel. Flat sheet membranes are most often used in spiral-wound and plate and frame modules and cannot be backflushed. Tubular membrane elements have

several flow channels or lumens with the selective layer on the inside and typically can be backflushed [9].

Stainless steel, which is inexpensive and mechanically stable, has been used in literature studies as the support for membranes [10]–[13]. Interest has increased in the modification of stainless-steel mesh for the purpose of oil and water separation, such as the coating of stainless-steel mesh with ceramics.

Membrane performance is strongly determined by the substances used in its production, its resistance to harsh condition and porosity, in which pore size and the shape of pores are key factors. In this work, we focus on bonding nanoplatelets of controlled morphology onto stainless-steel meshes.

Twinned alumina nanosheets (TAN) are a newly developed 2D/3D material, which have been successfully used to make dynamic membranes [14]. The special 3D structure of the twinned nanoplatelets, gives them a slit-pore like morphology instead of a circular shape. A membrane with slit-shaped pores that are small enough to completely exclude a given protein will have a permeability that is 2.67 (8/3) times greater than a membrane with cylindrical pores [15].

A single nanoplatelet forming the TAN has a length of 4 µm, a width of 1 µm and a thickness of 100 nm [16]. They have a very high porosity of 88% and must be supported on a very open layer in order to take advantage of this high porosity. However, this high porosity and this structure makes TAN assemblies easy to compact. The compaction of TAN nanoparticles was studied by X. Meng [17]. She found that TAN alone could not be used in a packed bed as it was subjected to compaction. Two binding materials SiO_2 and $AlH_6O_{12}P_3$ were studied to reinforce the TAN materials. SiO_2 was found to offer a better resistance to compaction than $AlH_6O_{12}P_3$. The results

of the work demonstrated that reinforced TANs offer a column packing with an open pore structure and improved channel connectivity.

The requirement for support materials in packed beds is to resist compaction. In the case of a membrane, the selective layer must resist compaction and bind to the support layer. This prevents the selective layer form being washed away in cross-flow filtration and offers the possibility of backflushing the membrane by reversion the flow of fluid passing through the membrane.

The objective of this work is to develop a synthetic membrane with a selective layer of 2D/3D TANs on a support to achieve high permeability and maintain mechanical strength at the same time. The structure of the TAN in the selective layer is to be reinforced with binders. In particular, we aim to:

- Bind TAN onto stainless steel meshes and ceramic supports.
- Verify the adhesion of TAN to the supports by observing the microstructure of the synthesized membrane using SEM, and performing permeation experiments.

1.2 Oil spill treatment techniques

An oil spill is the accidental or intentional discharge of petroleum hydrocarbons to the environment. A spill on water can be spread by current and wind, and form a surface slick. It can disperse in water, or accumulate in sediments [18]. Thus, an oil spill on water can damage marine ecosystems and contaminate water for drinking and other purposes. The Exxon Valdex oil spill in 1987 (11million gallons) [19] and the oil spill from the oil drilling rig Deep Horizon in 2010 (4.9million barrels) [20] were marked as the greatest disasters for the marine environment. It is necessary to employ various methods for oil spill response. A number of cleanup methodologies can be adopted

to control oil spills and keep them from spreading to the coastal areas. These methods include the use of boom, skimmers, in situ burning, dispersants, bioremediation, etc [21].

The most important characteristic of booms is containing spilled oil. They work as physical floating barriers to prevent an oil slick attempting to expand and concentrate oil for recovery. A boom has several parts containing the cylindrical inflatable buoy on the top, and a skirt made of metal or plastic, which is able to extend a few inches to a few feet below the surface [22].

Once the oil has been confined by using booms, skimmers can be applied to pump oil from the water surface. They are designed to physically separate the oil from water so that it can be collected and transferred on shore for further processing. Using booms and skimmers are often seen as the ideal solutions as these aims to remove oil from the marine environment without changing the chemical or physical properties of oil. Beyond these two major steps, there are plenty of other measures depending on the situation. In situ burning of an oil slick may be applied before it reaches the coast. This is an effective measure; however, it might release nitrogen and Sulphur, leading to additional pollution.

Sorbents are materials that soak up liquids through the mechanisms of absorption, adsorption, or both. Sorbents are most often used to absorb or adsorb final trace amounts of oil that could not be skimmed off, and then the sorbents must be removed from the water by nets and rakes and properly disposed of on land or recovered for re-use.

One of the controversial treatment methods includes the use of dispersants. The dispersants are sprayed on the oil spill to break it into small droplets, so that oil transfers into the water column. In this method, the amount of oil in the environment remains the same, while chemicals will be

introduced to the environment. As a consequence, decisions should be made regarding the possible impact to the ecosystem in using this technique [23].

Bioremediation methods involves the addition of microbes or nutrients to stimulate bacterial proliferation, and enhance the biodegradation of the spilled oil. The bacteria can break the petroleum hydrocarbon into simpler and less toxic molecules. Although there is anaerobic biodegradation of hydrocarbon in marine environments, the actual metabolism rate is particularly low. In most cases, nutrients are the rate limiting factors in oil biodegradation [24].

The effectiveness of the oil spill cleanup method depends on the amount and type of oil spilled and its dispersion by ocean currents and tides. The primary responses aim to ship the oil to onshore for further treatment, such as oil and water separation. Therefore, there is a growing demand for treatment on the site of the spill that produces water which can be discharged directly to the environment.

1.3 Materials for selective layers of membranes:

According to the Canadian Oil Pollution Prevention Regulations, the oil content of the undiluted discharged effluent should not exceed 15 ppm [2]. Synthetic membranes can be used to reach this discharge level. Peng and Tremblay (2008) have reached levels of 1 ppm in treating oily wastewaters.

In the past few years, advanced materials such as inorganic membranes have been used extensively for the separation of oil-water mixtures. Inorganic membrane technologies are widely used in water treatment and purification. Compared to polymeric membranes, inorganic membranes are inert to microbiological degradation. Furthermore, they are highly chemical, thermal resistant and

sterilizable. They can be challenged with high pressure backflushing and cleaned easily once fouled.

On the other hand, the traditional inorganic membranes consisting of metal oxides are heavier and brittle, depending on the application they can be more expensive than polymeric membranes.

The main types of inorganic membranes are; ceramic membranes, carbon-based membranes, silica membranes, zeolite membranes and dynamic membranes, etc. It should be mentioned that dynamic membranes are a kind of secondary membrane that can be dynamically formed. It can trap the foulant material in a deposited layer on top of the membrane. Once it has become severely fouled, it could be removed by brushing or acid cleaning and form a fresh layer to continue filtration operations. In this study, we do not consider dynamic membranes. Different fabrication methods have been used to synthesize inorganic membranes, including slip casting, tape casting, pressing, extrusion and sol gel methods. The most commonly used inorganic membranes in water treatment are titania, zirconia, alumina, and carbon based membranes [7].

1.3.1 Ceramic membranes

Ceramic membranes are a type of artificial membrane that are made from metallic oxides (alumina, zirconia oxides, titania), silicon carbide or some glassy materials such as silica. Other materials can also be used to make ceramic membranes, including non-oxides (nitrides, carbides, silicides, and borides). An asymmetric ceramic membrane consists of two or three layers, a support layer with coarse pore size, an intermediate layer and a selective layer with the required pore size to provide selectivity and separation.

Based on the characteristic pore size of the top layer, ceramic membrane can be classified into three categories, namely micro-porous, meso-porous and macro-porous membranes. See Table 1-1.

Table 1-1. Types of ceramic membranes

Pore type (size range, nm)	Pore size (nm)	Applications
Micro-porous	<2	NF (nanofiltration), GS (gas separation)
Meso-porous	2-50	NF + UF (ultrafiltration), GS
Macro-porous	>50	UF/MF (microfiltration)

1.3.2 Preparation of ceramic membranes

Ceramic membranes are usually available in three configurations, including flat, tubular, and multichannel. The preparation of ceramic membranes commonly involves the following three steps [7].

- Paste or suspension preparation by mixing the ceramic powders with the binding liquid.
- Shaping the prepared paste or suspension into some desired geometry.
- Heat treatment to bind the ceramic particles through the calcination or sintering processes.

The last step is critical in determining the mechanical and structural properties of the membrane. Further control on the pore size or multilayer membrane fabrication can be achieved by subsequent coating or heating steps. We here briefly overview several fabrication methods that are commonly used for ceramic membranes.

1) **Slip casting**. It is the most commonly used method for membrane preparation, involving the use of a porous mold to cast the ceramic membrane into the required shape [25], [26]. After a powder suspension is well mixed, it is then transferred into a porous mold. Capillary forces promote the extraction of solvents from the pores during slip casting leaving the ceramic particles to form the pores. Slip casting is usually used to form hollow fiber ceramic membranes, which are known for their high permeability attributed to the presence of larger pore size over a thinner region, thereby leading to high fluid permeation [27].

2) **Tape casting**. It is a technique used to fabricate flat-sheet ceramic membranes [28], [29]. In this method, a ceramic paste with good suspension and pseudo-plastic behavior is first prepared. The paste is then sent to a reservoir and controlled by a blade with an adjustable height to cast the membrane. The produced casted layer is then passed through a drying zone at which the solvent evaporation from the membrane surface takes place [30]. The ceramic membranes prepared by this technique are usually a few millimeters thick.

3) **Pressing**. Disc inorganic membranes are usually prepared using this method. During the fabrication process, a pressure greater than 100 MPa is applied to the membrane surface using a press to yield a sintered dense layer. The disc has a thickness of about 0.5 mm and diameter in the range of few centimeters [5]. The main drawback of this method is the difficulty to fine-tune the pore microstructure and control the membrane thickness to diameter ratio. Moreover, the process is considered a batch process and is mainly used for membranes destined for use in laboratories [31].

4) **Extrusion**. Extrusion is another method to produce tubular and hollow fiber ceramic membranes. In this method, a homogeneous stiff paste is forced through a nozzle to be compacted or shaped to form the final membrane. To keep the membrane in its desired final shape, any remaining binder, solvent, and plasticizer should be evaporated. The shape, porosity, and pore size distribution of the final product is determined by the die [32].

5) **Sol-gel method**. Sol-gel is a method to form homogeneous layers/structures of fine particulates on the membrane [5], [31]. The raw material may be a metal organic compound (alkoxide) or a metal salt. Suitable precursors are reacted by polymerization or colloidal pathways. An acidic or basic catalyst can be used in the reaction route, and finer particles can be produced by an acidic catalyst, which will eventually produce a finer microporous structure at the end of the membrane preparation process [33]. The sol-gel method is a very useful method for preparation of tailor-made membrane layers. Not only can the particle size in the sol be controlled, but the surface properties of the membrane can also be adjusted by tuning the chemical composition.

1.3.3 Zeolite membranes

Zeolite membranes are used in highly-selective gas separation applications due to their uniform pore size. Zeolites are also a catalytic substance, which makes them advantageous in catalytic membrane reactor applications. Concerns about zeolite membranes include thicker layer requirements in case of cracking and relatively low gas flux.

1.4 Pore geometry effects & biomimetic considerations

Microfiltration and ultrafiltration are pressure driven sieving processes, where particles that are larger than the membrane pore size are removed. Ideally, a membrane with high permeability and high separation is desirable. However, in practice membranes with high permeability have low selectivity and vice versa. In order to improve both permeability and selectivity, research in producing membranes having other shapes than the usual circular shape is growing.

1.4.1 Biomimetic technology

The human kidney filters blood using slit diaphragm membranes. These membranes are made from various proteins that are synthesized by podocytes. The proteins extend across filtration slits. Proteins from adjacent foot supports interact to form a mesh-like barrier which excludes proteins based on their size [34]. This barrier has size and charge selective properties. Rodewald and Karnovsky suggest that the slit diaphragm is a zipper-like structure that functions as a sieve, with a pore size smaller than albumin. Since the slit diaphragm appears as the final seal to prevent loss of circulating proteins into urine, this unique intercellular junction has been the focus of increased research interest [35].

1.4.2 Effects of pore size distribution and pore geometry

Siddiqui et al (2016) [36] used a modeling approach to investigate the effect of the distribution of pore sizes and pore shapes on the permeability-selectivity tradeoff for MF and UF membranes. The results show that increasing pore aspect ratio provides improvement in membrane

performance while an increase in the width of the pore size distribution deteriorates the permeability and selectivity tradeoff.

Kanani et al (2010) [37] carried out experiments to study the effect of pore geometry on the permeability-selectivity tradeoff for membranes with pore size below 100nm. By using the novel silicon membranes with well-defined arrays of uniform slit-shaped pores, they demonstrated that slit-shaped pores can have significantly enhanced performance, compared to ultrafiltration membranes with cylindrical pores. The model calculations indicated that pore size distribution has a greater influence on the performance of membranes with slit-shaped pores due to the larger value of the protein sieving coefficient in a slit pore having the same critical dimension as a cylindrical pore. Therefore, the advantage of applying membranes with slit-shaped pores can only be achieved if these membranes also provide a relatively narrow pore size distribution.

Zydney et al (2011) [15] pointed out that the pore size distribution in existing UF membranes has a relatively smaller effect on the permeability-selectivity tradeoff. Most efforts have focused on attempting to reduce the pore size distribution to enhance the performance of UF membranes, by fabrication of composite membrane structures, or varying the casting conditions. However, reducing the size distribution achieved relatively little improvement. In their results, using membranes with slit-shaped pore, or electrically charged membranes might significantly improve the performance of UF membranes. It compared the hydraulic permeability of membrane with uniform cylindrical pores using Hagen-Poiseuille equation with a membrane having uniform slit-shaped pores by the corresponding equation. Based on Hagen-Poiseuille equation and the representation of the membrane as a parallel bundle of tubes, the hydraulic permeability (L_p) for a membrane with uniform cylindrical pores can be calculated using the equation below,

$$L_{p1} = \frac{\varepsilon R^2}{8\mu\delta_m}$$

where ε is the membrane porosity, R is the radii of cylindrical pore, μ is the viscosity of the solution, and δ_m is the thickness of the membrane. The corresponding hydraulic permeability of a membrane with uniform slit pores is,

$$L_{p2} = \frac{\varepsilon h^2}{3\mu\delta_m}$$

where h is the half-width of the slit pore. Therefore, if the two membranes have the same porosity, thickness, and characteristic pore size, we have $\frac{L_{p2}}{L_{p1}} = \frac{8}{3}$, which indicates that a membrane with slit-shaped pores that are small enough to completely exclude a given protein will have a permeability that is 8/3 times greater than a membrane with cylindrical pores.

1.5 Twinned Alumina Nanosheets (TAN)

The self-assembly of twinned boehmite nanosheets into porous 3D structures, was developed by Roebuck and Tremblay in 2016 [16]. By varying the concentration of the surfactant monomer and ethanol in the synthesis, the thickness, shape and twinning of the nanosheets could be influenced. They reported that with a critical micelle concentration of cationic surfactant cetyltrimethylammonium bromide (CTAB), in 50 vol% ethanol-water mixtures, the particles of CTAB-templated boehmite nanosheets exhibited an elongated shape, had the smallest thickness with a narrow thickness distribution, and the 3D structure they formed had a very high porosity and hydraulic permeability.

Roebuck et al (2016) [38] explored the performance of the dynamic membranes (DM) produced by aggregates of nanosheets. The unique morphology of the alumina nanosheet aggregates resulted in high porosity with three-dimensional connectivity. Alumina aggregates were synthesized in 0, 25, and 50 vol% ethanol-water solutions by the calcination of boehmite. The Al-50 DM had the highest operating flux during bentonite filtration, highest packing density and porosity among the three DMs. The high packing density provided an evenly distributed flow throughout the aggregate pores.

Roebuck et al (2017) [14] analyzed two types of precoat filters that were formed by the deposition of TAN particles and diatomaceous earth (DE) on a support. The TAN precoat showed better flow properties and reduced the turbidity of the filtrate more rapidly than the DE. They demonstrated that TAN particles maintained their structural integrity during filtration and resisted compaction due to the unique twinning of the alumina nanoplatelets. Moreover, the structure of the deposited TAN layer was isotropic, leading to permeability in all directions.

The synthesized particles had a length of 4 μm, a width of 1 μm, and a thickness of 100 nm. Their hydraulic permeability was 714 mD for a 0.2 μm-pore size dynamic membrane. Their porosity could reach up to 88% with a macroscopic surface area of 5.7 m^2/g, due to their low nanosheet volume. These unique characteristics make the nanosheet a very promising material in membrane applications [38].

The pores on a traditional ceramic membrane are circular in shape. When particles are filtered, they can block part of the openings. If particles are filtered having a larger diameter than the pore size, these may obstruct three adjoining pores at the same time. However, the twinned alumina

nanosheets offer a surface that has pores with sharp edges that can prevent the particles from entering the pores and help in their release when the membrane is backflushed.

Last but not least, the matrix confined between the circular pores in traditional membrane layers can accumulate fine particles. While for TAN, the combination of a thin platelet and the low nanosheet volume gives no space for particle accumulation.

Due to its high permeability and slit-pore 2D/3D configuration, TAN is a promising coating material to act as a selective layer instead of the traditional circular-pore ceramic membrane. To date, no integral membrane has been made from TAN. Only dynamic membranes have been made from TANs. A dynamic membrane cannot be used in a cross-flow application as the selective layer of the membrane will be washed off by the feed fluid. Dynamic membranes cannot be backflushed. It is the objective of this work to bind the TAN material to a suitable support in order that it can be backflushed by reversing the flow of the feed solution in order to release the filter cake accumulating at the surface of the membrane.

1.6 Backing materials

1.6.1 Selection of a membrane support

A membrane support provides mechanical strength to the selective layer which is usually very thin in order to promote flow through it. The selection of a proper membrane support is as important as choosing a suitable selective layer. Although it is often preferred to use identical materials for membrane and porous support to reduce thermal expansion mismatch, different materials might be considered based on their cost and mechanical properties. Different types of materials have

been used in the fabrication of membrane support including MgO, Al_2O_3, ZrO_2, CGO ($Ce_{0.9}Gd_{0.1}O_{1.95-\delta}$), BSCF ($Ba_{0.5}Sr_{0.5}Co_{0.8}Fe_{0.2}O_{3-\delta}$), LSCF ($La_{0.6}Sr_{0.4}Co_{0.2}Fe_{0.8}O_{3-\delta}$), and metals.

Lipinska-Chwałek et al. [39] conducted a detailed study of the mechanical properties of porous MgO supports. The effect of sintering conditions on porosity and mechanical properties, i.e. elastic modulus and fracture stress as function of temperature were summarized for planar and tubular support geometries. It was found that sintering temperature and time offer optimization potential for porosity. Moreover, compared with CGO, BSCF or LSCF substrates, the price of MgO is much less.

Alumina substrates are also widely used industrially. Abadi et al. [6] employed a tubular ceramic MF (α-Al_2O_3) system for the treatment of a typical oily wastewater. Effects of operating parameters such as transmembrane pressure (TMP), cross flow velocity (CFV) and temperature on permeate flux, TOC removal efficiency and fouling resistance (FR) were investigated. They also found that backflushing could prevent permeate flux decline significantly.

Biesheuvel and Verweij [8] used a combined experimental and theoretical approach to optimize the design of a ceramic membrane support. The tensile strength and permeability of ceramic membrane supports made by colloidal processing and dry-pressing were measured. Using colloidal techniques and a suspension of dispersed particles, they obtained a material with a higher tensile strength and a lower permeability than in the case of dry-pressing.

Zhang and J. Malzbender [40] investigated nano- and micro-porous materials as supports for NF membranes. The micro-porous support had a higher strength than the nano-porous material due to a larger contact area between grains. However, initial permeation tests indicated that the nano-porous substrates lead to an approximately one order of magnitude lower flux than the micro-

porous substrate material. This will result in much higher flow resistance and blockage of flow pathway in the substrate, therefore undermining the filtration performance of the membrane. They stressed the importance of an optimized balance between the mechanical strength of the substrate and the permeate rate.

In the present study, we choose to use a stainless-steel substrate. High temperature endurance, strong mechanical strength, and high porosity provide a combination of material strength and high flow rate, which is ideal for membrane separation purposes. Due to its ease of fabrication, good weldability, ductility and low cost, stainless steel supported filters have been widely used in oil-water separation, waste water treatment, soil contaminant remediation, and so on [10]–[12], [41], [42]. With appropriate modification techniques, the surface of stainless-steel meshes can be changed to a superhydrophobic (or superhydrophilic) surface so that oil (or water) can easily pass through the mesh while water (or oil) is repelled.

1.7 Etching

Stainless steels, mainly consisting of chromium (minimum of 10.5 wt%), iron and nickel, are most known for their corrosion resistance. As opposed to ceramics, they have a much lower cost, higher mechanical stability under backflushing condition and are resistant to cracking, which make them potential support materials for membranes where both corrosion resistance and mechanical stability are required.

The surface morphology of the support material plays an important role in bonding with the selective layer. As stainless steel is known for its smooth surface. Etching is an effective way to

form a micro/nanostructure on its wire surface, which creates more surface area before coating with nanoplatelets.

1.7.1 Chemical etching

Varshney et al. [43] implemented a chemical etching method using a mixture of hydrochloric acid and nitric acid (in a 1:3 ratio), followed by immersion in a lauric acid solution to roughen the surface of stainless steel to improve oil/water separation. After the treatment, they observed rough microstructures on the coated steel mesh surface, which exhibited both superhydrophobicity and superoleophilicity, so that water runs off the mesh while oil permeates through it. Petroleum ether–water and benzene–water mixtures were successfully separated via a simple filtering method using the coated mesh with a separation of more than 99%.

Nanda et al. [44] synthesized superhydrophobic and superoleophilic coatings on stainless steel mesh via chemical etching using a mixture of $FeCl_3$ and HCl followed by treatment with hexadecyltrimethoxysilane. They observed flower-like microstructures on the surface after treatment. The coating shows excellent thermal, chemical and mechanical stability. Kerosene-water and hexane-water mixtures were successfully separated via a simple filtering process using coated steel mesh with a separation of more than 98%.

Frank et al. [45] fabricated a superhydrophobic stainless steel surface by sand-blasting and then chemically etching the surface with myristic acid. The effect of chemical etching with HCl and HF on surface morphology was studied. They also studied the influence of soaking time in the myristic acid solution and the effect of the concentration of myristic acid in the soaking solution

on the finally achieved wettability. With the optimized surface modification parameters (roughness, myristic acid coating time), they were able to achieve a maximum contact angle of 167°.

Yu et al. [41] prepared a hydrophobic steel mesh by etching commercial stainless steel mesh with $FeCl_3$ alcohol solution and successively coating it with n-octadecanethiol. The treated mesh showed high oil/water selectivity for a broad variety of oils and organic solvents. Using the modified mesh, they developed a multilayer 3D structure as the separation material for the in-situ separation of spilled oil. They then conducted oil/water separation experiments and found that oils with different viscosities can be separated continuously from oil/water mixtures.

1.7.2 Electrochemical etching

Choi et al. [46] performed electrochemical etching of 316 stainless steel immersed in nitric acid (HNO_3, 70 %) to control the wettability of the surface. They observed that variation of the applied anodic potential changed the etch selectivity between grains and grain boundaries and thus the resulting surface structure. Based upon the observed relationship, they designed a process to achieve nano/microscale hierarchical intrinsic grain structures on the stainless steel surface that is water-repellent.

Stover et al. [47] studied two methods of electrochemical surface microstructuring as a basis for the drug-coating of coronary stents. They found that electrochemical etching with hydrochloric acid at 2.28 mA/mm^2 produced an evenly rough, terraced surface. which deteriorated the adhesion properties. On the other hand, they showed that electrochemical grain-boundary etching rendered a furrowed, microstructured surface offering volume for the coating drug, which resulted in a higher amount of drug on the stent after dilatation.

Kim et al. [42] used electrochemical etching followed by a hydrophobic coating process to adjust the wettability of stainless steel meshes. The mesh wire pieces were etched electrochemically to form re-entrant structures by immersing them in aqueous solution of 3.6 wt% (1 N) HCl and 1.2 wt% HNO_3 mixed in a 1:1 volume ratio, with the piece of mesh subjected to positive polarity and a carbon electrode that was set parallel to it to negative polarity. They found that the degree of repellency of the treated mesh could be controlled by simply adjusting the voltage and duration of electrochemical etching.

1.8 Binders for ceramic membranes and stainless steel

The performance and durability of a membrane greatly depends on its morphology and mechanical strength, which is dominantly controlled by binder content, preparation pressure, sintering temperature, etc. [48] Therefore, it is essential to optimize these parameters to tune the membrane performance. The proper selection of binders and the concentration of binders to mix with membrane materials is of critical importance to ensure the mechanical strength of the membrane, and to optimize the pore size distribution for selectivity purposes. Based on the composition of binders, they can be classified into two main types, namely organic and inorganic binders.

1.8.1 Organic binders

Organic binders are used in the molding process and are lost in calcination. They are important in minimizing defects during calcination. The commonly used organic binders include polyvinyl alcohol (PVA), polyvinyl butyral (PVB), methyl cellulose, and hydroxypropyl cellulose (HPC). Ahmad et al. [49] used PVA and HPC as organic additives to synthesize TiO_2 membranes. The

addition of PVA and HPC resulted in a relaxation of stress and a strengthening of the gel network. Significant alteration upon the TiO_2 microstructure was observed, increasing average pore width, pore volume, and surface area, and as a result affecting the morphology. Crack formation was also avoided. Abdallah et al. [50] fabricated ceramic membrane samples shaped in disk form using PVA as a polymeric additive, and tested the membrane performance. They found that membranes produced using PVA displayed reasonable mechanical strength allowing them to withstand incoming water pressure. Arzani et al. [51] prepared ceramic monolith MF membranes for treating a synthetic solid-liquid wastewater comprising SiO_2 powder in water. The effect of PVA concentration on mechanical strength and pore size of the membrane was studied. Lian et al. [52] prepared PVB based polymer membranes for lithium-ion batteries. The dense PVB based membranes showed high mechanical strength of 16.33 MPa and high liquid uptake of 288%. Sarkar [53] prepared multichannel tubes with alumina and clay using methocel as the binder, which resulted in a crack-free straight and mechanically strong porous clay-alumina ceramics with average pore size of 1 μm and porosity of 39%. Zhou and He [54] used poly(dimethylsiloxane) (PDMS) as a molecular binder to fabricate glass fiber membranes for robust oil/water separation. The SiO_2 nanoparticles were found to be firmly anchored onto the glass fiber surfaces to produce superhydrophobic/superoleophilic membranes with “oil selectivity”.

1.8.2 Inorganic binders

Organic binders suffer from several deficiencies which limit their applications, such as poor mechanical strength, appearance of micro cracks and pores, uncontrolled binder burnout resulting in dimensional inaccuracy [55]. In addition, organic binders create problems such as

agglomeration and retention of organic species in the non-sintered product as impurities, which finally reduce the efficiency of the membrane [56]. Such binders also create difficulties in ceramic paste processing such as extrusion, due to its inadequate or excessive addition with the ceramic powder.

As an alternative, inorganic binders are widely used to mitigate such problems. For example, Fernando and Chung [57] compared the mechanical properties and pressure drop characteristics of alumina fiber based filter membranes made using three types of binding materials, including colloidal silica, colloidal alumina, and phosphate. They found that the filter membranes containing between 5% and 10% by weight of acid phosphate binder exhibited the highest flexural strength, compressive strength, work of fracture and elastic modulus. Ray et al. [58] used boehmite sol as an inorganic binder to prepare porous alumina membranes, which not only reduced the pore size of the membranes but also provided acceptable mechanical strength to the membrane prepared at 1350 °C. They also found that the membrane prepared without organic binder resulted in smaller pore size and better treatment efficiency with low fouling characteristics compared with conventional ceramic membranes prepared with organic binders. Liu et al. [59] studied HZSM-5 coating using three colloidal silica binders, including acidic colloidal silica (ACS), neutral colloidal silica (NCS) and basic colloidal silica (BCS), and found that zeolite coating using BCS shows the smoothest surface with higher homogeneity and adherence strength. Boix et al. [60] used silica binders to washcoat PtCo/Ferrierite on a ceramic monolith to improve adherence and to obtain a selective catalyst. In the study by Yu et al. [61], nano-silica was applied as a binding agent on ultra-high-performance concrete (UHPC) and its effect on the hydration and microstructure was investigated. It was reported that the highest mechanical properties were obtained with only 3.74% by the mass of the binder. Dong et al. [62] fabricated fibrous porous

zirconia ceramics through a gel casting process by adding K_2SO_4 as binder. Sun et al. [63] fabricated fibrous zirconia ceramics with ultra-high porosity (72–89%) through a process of mixing the slurry of zirconia fibers and a silica binder. The results showed that the zirconia fibers were bonded successfully mainly at the fiber junctions, and 10 wt% binder and 1600 °C were the optimal processing parameters for better properties.

1.8.3 Binder selection

Few studies have been reported on binding ceramic selective layers and a stainless-steel mesh to form a membrane. To ensure mechanical strength and high flux permeability, we chose to use inorganic binders, in particular colloidal silica and colloidal silver. Silica is a widely used binder in the refractory and ceramic industry. It is often used in the form of an aqueous dispersion containing 20 to 50 wt% of silica colloids. The average colloidal size of the silica can range from under 10 nm to over 80 nm. The silica binder has many advantages, including its ease of use and good temperature endurance.

Silver was also evaluated as a binding agent. Nanoparticles of Ag_2O, were included in the binding solution and heated to above 300 °C to reduce the silver to Ag_0. This binding agent has not been reported in the literature.

1.9 Objectives

As previously mentioned, the objective of this work is to produce a composite membrane with a selective layer of 2D/3D alumina nanoplatelets (TAN) on a support. The 3D structure of the TAN

selective layer is to be reinforced with binders. The selective layer is to be bound to the support by the binder. The main objective of this work is to verify the adhesion of the TAN selective layer onto the support. This will be done by challenging the membranes with a suspension of 10 ppm bentonite and backflushing the membranes with pure water. The presence of a consistent membrane flux, after successive backflushing cycles, will verify that the selective layer has successfully adhered to the support.

2 Experimental

2.1 Materials

Aluminium chloride hexahydrate (99%, nitrogen flushed) was purchased from Acros Organics. Sodium hydroxide (Pellets/Certified ACS) were purchased from Fisher Scientific. Cetyl trimethylammonium bromide (CTAB), colloidal silica (40% w/w solution), colloidal silver (65-75%, Ag basis) and bentonite were purchased from Sigma-Aldrich Canada. Hydrochloric acid (37%) (Acros Organics) and Nitric acid (10%) (LabChem) were both purchased from Fisher Scientific. Anhydrous ethanol (Greenfields alcohol), isopropanol, Polyethylene glycol (PEG 6000) (Fisher Scientific) were also used.

The autoclave used for particle synthesis was a Teflon-lined stainless-steel autoclave with a thin internal PEEK sleeve (Parr Instrument Company, Illinois). The oven used for calcination was a Thermo FB1315 Benchtop Muffle Furnace (Thermo Scientific, Massachusetts). Vent tubes were assembled to permit the evacuation of the reactor contents in case of overpressure. A scanning electron microscope (Phenom Pro Desktop SEM (Nanoscience Instruments, Virginia) at 5kV and 10kV) was used to characterize the synthesized particles and membrane. Particles were mounted on aluminum stubs (Ted Pella, Redding, California) for observation in the SEM. The turbidity meter used in the permeation experiments was a Micro 100 Turbidimeter (HF Scientific Inc., Fort Myers, Florida).

Stainless-steel meshes (316 Stainless Steel, small-particle-filtering stainless steel wire cloth), the conductive graphite sheet used as polarity material for electrochemical etching, and the urethane structural adhesive were purchased from McMaster-Carr. All materials were used as purchased.

2.2 Methods

2.2.1 2D/3D nanosheets (TAN) synthesis

Twinned Alumina Nanosheets were synthesized according to a procedure developed in our laboratory [16]. TAN synthesis, included 3 steps; seed mixing, autoclaving and calcination. The raw materials used in preparing the seed mixture for crystallization into boehmite particles were: aluminum chloride hexahydrate, sodium hydroxide pellets that were dissolved in ethanol and deionized water. With the purpose of affecting the self-assembly of nanomaterials into desirable 3D superstructures, Cetyl trimethylammonium bromide (CTAB) was added to the seed mixture. After 24 hours of agitation, the mixture was autoclaved to form twinned boehmite nanoplatelets. Calcination at 600 °C for 4 hours produced alumina nanoplatelets [16].

Details of the fabrication procedure are as follows; aluminum chloride hexahydrate (1.45g) was dissolved in 30 g of distilled, deionized water under vigorous stirring. Ground sodium hydroxide pellets were added to the aluminum chloride hexahydrate solution to reach a pH of 14. CTAB (0.84g) was dissolved in 45g of anhydrous ethanol. Both solutions were combined to form a seed solution that was continuously stirred at 430 rpm for 24 hours at room temperature. After stirring, the seed solution was poured into three Teflon-lined stainless-steel autoclaves line with a PEEK sleeve (Parr Instrument Company, Illinois), sealed and heated to 165°C for 12h under autogenous pressure. Boehmite nanoplate crystals accumulated at the bottom of the autoclave in the shape of a disk. The disk of particles was taken out, lightly covered and placed in the fume hood overnight. The dried precipitates were then calcined at 600°C for 4 hours. After calcination, the particles were stored for analysis and deposited onto supports.

2.2.2 Temperature during seed mixing

Experiments on TAN synthesis were carried out under different seed mixing temperatures, in order to study the optimum temperature to produce the desired TAN structures. A temperature controlled air bath was assembled and the seed solution was stirred for 24 hours at a set temperature. The temperature in the bath was controlled to +/- 0.1 C. The TAN were prepared as described above. The yield of each batch of TAN was determined. The quality of the TAN network produced was qualitatively assessed using SEM.

2.2.3 Pretreatment and selection of stainless-steel mesh

The TAN particles were deposited onto stainless steel meshes by filtration. Several stainless steel meshes of various pore openings were evaluated. A small particle-filtering stainless steel wire cloth, also known as a Dutch weave, was selected as a membrane support. It has a tight weave that traps tiny particles and provides strength for use in high-flow and high-pressure applications. Mesh with different opening sizes (10, 26, 35, 80 micron) having same weave were tested to determine the optimal opening size for TAN deposition. The mesh type with different sizes can be found in Table 2-1.

Electrochemical etching of the stainless-steel was used to form a re-entrant surface on the mesh piece. The mesh was cleaned with a water based, degreasing cleaner (Spray nine) and then rinsed with distilled-deionized water. An electrolyte was prepared with 3.6wt% of HCl in water and 1.2wt% of HNO_3 in water mixed in a 1:1 volume ratio. The mesh was immersed in the electrolyte solution and placed parallel to a conductive graphite plate under a constant electric potential of 5V.

Table 2-1: The stainless- steel meshes with different sizes used as the support layer

Meshes	Tyler Mesh size	Smallest Opening dimension (μm)
1	200 × 1400	10
2	165 × 800	25
3	200 × 600	26
4	80 × 700	35
5	24 × 110	80

Meshes were etched for 4 min and 12 min and characterized by SEM. The mesh was connected to the positive post, and the carbon was connected to negative post of the power supply. After electrochemical etching, the mesh piece was rinsed with distilled-deionized, water to avoid further chemical etching, which would weaken the stainless-steel mesh. The mesh piece was then soaked in isopropanol and left to dry before binding with TAN.

2.2.4 Binding of TAN

According to previous work performed by X. Meng [17], a mixture of silica diluted with water and ethanol was found to be an excellent binding agent for the use of alumina nanosheets in packed beds [17]. In this work, we also aim to apply silica to join the alumina nanosheets to resist compaction during filtration process. In order to obtain an open pore structure on drying prior to sintering, it is important to lower the surface tension of the binding solution. Lower alcohols, such as methanol, ethanol, isopropanol or butanol, can be selected to add to the binder solution. Among these alcohols, methanol is toxic and has a relatively weak hydrophobicity[64]. The solubility of

salts in isopropanol and butanol is less than that in ethanol. Therefore, ethanol was selected as a surface tension reducing agent in all formulations.

Silver was also evaluated as a binding agent. Nanoparticles of Ag_2O, were included in the binding solution and heated to above 300 °C to reduce Ag_2O to Ag_0.

The concentration of silica in the liquid mixture is an important parameter that affects the structure of the TAN layer. High concentrations of silica can block the porous structure, while a low concentrations of silica may not give good binding performance. The optimum concentration of silica will leave just the correct amount of silica at the nanoplatelet intersections for binding and offer an open porous structure.

Twenty grams of ethanol were mixed with 180g of distilled-deionized water. TAN (0.1g) was mildly ground and added to the solution. A cylinder pump system was used to rapidly pump the feed solution onto the stainless-steel mesh under a pressure of 60 psi. The filtrate was then passed through the filter 20 times. The filtrate became clear after it was passed a few times through the wire mesh. This indicated that a cake had formed on the wire mesh. The feed solution was replaced by the binder solution. The binder solution was then passed a few times through the filter. The mesh was left to dry naturally in the fume hood, and calcined for 4 hours. Several binder compositions were studied. Binder solutions containing 2.5, 5, 7, 10 and 15 wt% silica were processed as described above.

2.2.5 Optimum sintering temperature

To find the optimal sintering temperature without damaging the surface texture of the stainless-steel mesh wires, TAN and silica binder were deposited on a stainless-steel mesh as previously described. The coated mesh was cut into several pieces and sintered at 700, 800, 900 and 1000°C, and analyzed by SEM.

2.2.6 Permeability test of the stainless-steel mesh supported membranes coated with TAN

In order to study the permeate flux, separation (retention) and other membrane properties of the synthesized membrane, the synthetic membrane was challenged with 10 ppm of bentonite suspended solution using a filtration system shown in Figure 2-1.

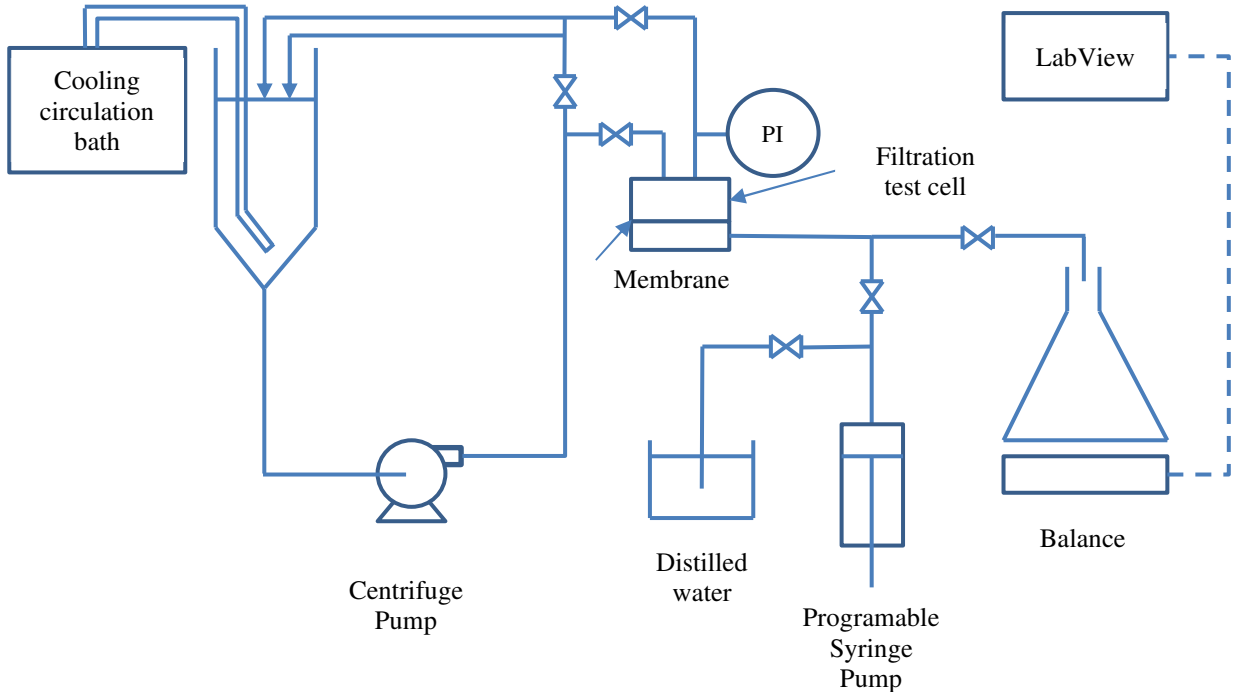

Figure 2-1: Filtration set-up with backflushing

A typical filtration experiment was as follows: the synthesized membrane sealed at the edges with polyurethane, was placed in a filtration test cell. Distilled water was first passed through the filter for about 4 minutes at an applied pressure of 100 mbar to determine its pure water permeate flux. Bentonite (0.0518g) in 80g of distilled water was ultrasonicated using a Fisher Scientific Sonic Dismembranator 550 for 60s at a power of 50%, and then added to the tank containing 5.1 L of distilled water. Backflushing of the membrane was carried out by a 50ml syringe pump shown in Figure 2-1.

The programmable syringe pump was set to withdraw 5ml of distilled deionized water from a beaker every 15 minutes. Pneumatic valves controlled by the syringe pump were used to infuse 5 mL of water through the membrane in the reverse direction to bentonite filtration. This proceeded over the course of 75 seconds to give a backflushing flux of approximately 400 Lmh ($L/m^2/h$). Each run was continued for 4 hours.

The turbidity of the feed and permeate were measured manually at time intervals of approximately 15 min. The mass of permeate flow from the test cell was continuously measured by a balance, and the data was collected using LabVIEW (National Instruments, Québec).

2.2.7 Permeability test of ceramic membrane supports coated with TAN

The surface layer of several 1.4 µm x 47 mm diameter ceramic disk membranes (Strerlitech 47M140) was removed by sanding and coated with TAN particles by filtration as described above. These ceramic membranes and the coating formulations used are shown in Table 2-2.

Table 2-2: Ceramic membrane supports with different selective layers.

Ceramic membranes	Pore size of the ceramic support (μm)	Original selective layer removed by sanding	Materials deposited on membrane
1	1.4	Yes	0.05g TAN+10wt% Ethanol+10wt% Silica+3wt% PEG+5g H_2O
2	1.4	Yes	0.013g TAN+5wt% Ethanol+10wt% Silica + 1.5 wt% PEG+2.5g H_2O
3	1.4	No	none

These membranes were all challenged with a 10 ppm bentonite solution in the set-up described in section 2.2.6 above.

3 Results and discussion – Optimal seed mixing temperature

3.1 Effect of seed mixing temperature on the yield of TAN

Experiments were carried out to determine the optimal seed mixing temperature in order to obtain a maximum yield of TAN while maintaining the best nanoplatelet structure. Experiments were carried out at a specific seed temperature, followed by autoclaving and calcination as described in section 2.2.2 above. The final products were collected as a solid disk in the bottoms of the three autoclaves, dried overnight and weighed. Figure 3-1 shows the yield of TAN with respect to the temperature of seed mixing.

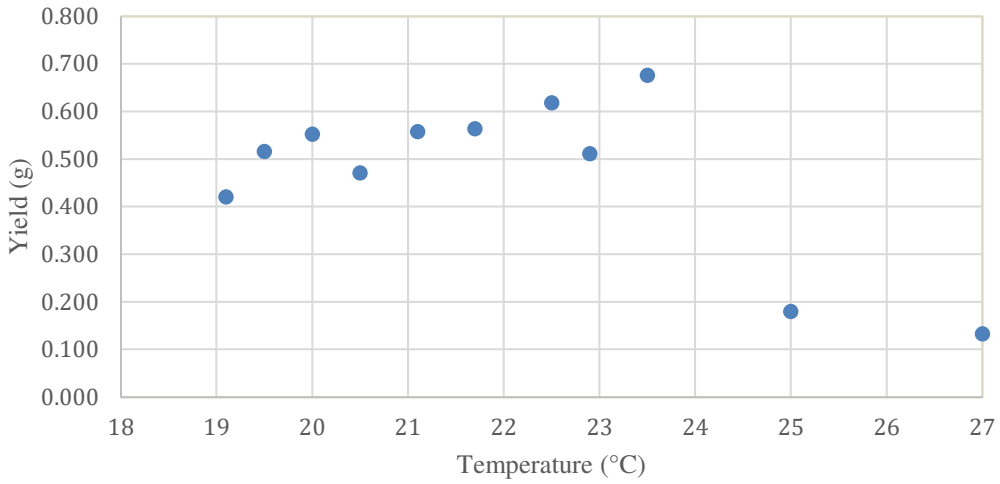

Figure 3-1: The yield of TAN at different temperatures during raw material mixture stirring.

It can be seen that the yield of TAN varies slightly at temperatures between 19°C and 23.5°C. At 19°C, boehmite formed a solid rigid disk at the bottom of the autoclave liner, with 0.42g of production once calcined. At 22.5°C, the production of TAN goes up to 0.68g. While the yield drops rapidly when it reaches 25°C.

3.2 Effect of seed mixing temperature on structure of TAN

SEM images were taken for the synthesized TAN prepared by the method demonstrated in section 2.2.2 at various temperatures. As seen in Figure 3-2, when the seed mixing temperature is between 19°C and 21.7°C, most of the particles tend to form hexagons and are twinned to produce a 2D/3D structure. However, as seen in Figure 3-3, above 21.7°C, particle size decreases with increasing seed mixing temperature. They also form nonporous aggregates. Particles at these higher temperatures will have low porosity and are likely to be unevenly distributed on the surface of the supports.

It can be concluded that TAN synthesized with a seed mixing temperature from 19°C to 22°C have a more desirable structure. Based on the results observed above, 20 °C was determined as the optimal seed mixing temperature, where most the particles are twinned hexagons that are not aggregated in large clusters and can be produced at a high yield.

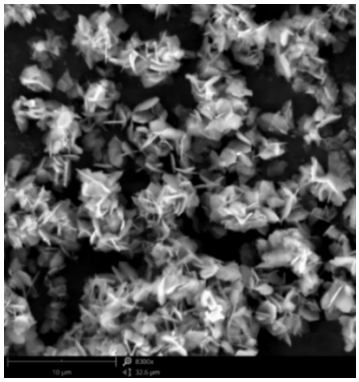

(19.1°C)

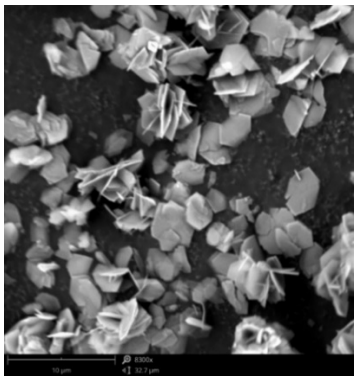

(19.5°C)

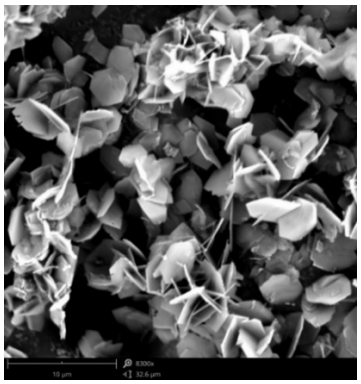

(20°C)

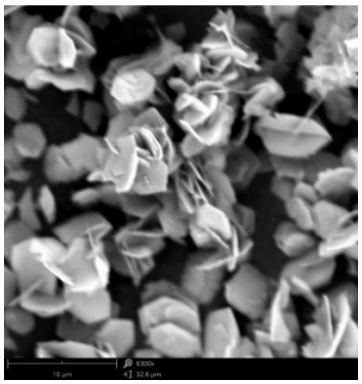

(20.5°C)

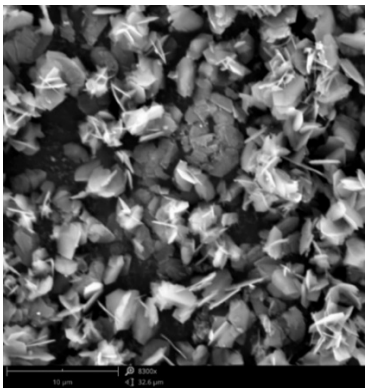

(21.1°C)

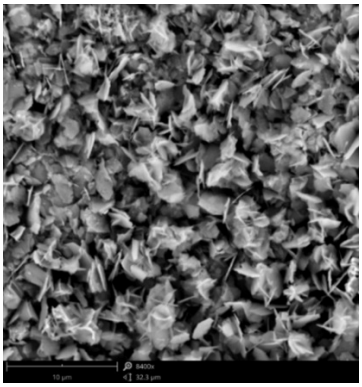

(21.7°C)

Figure 3-2: SEM images showing particle structure of TAN at temperature 19.1-21.7°C during seed mixing, recorded at 8300x.

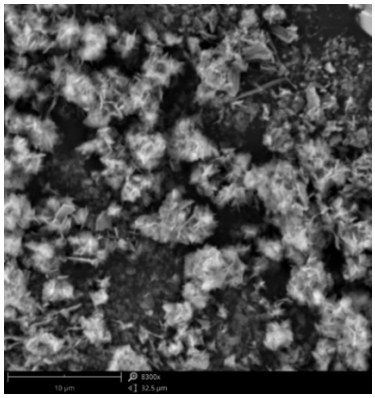

(22.5°C)

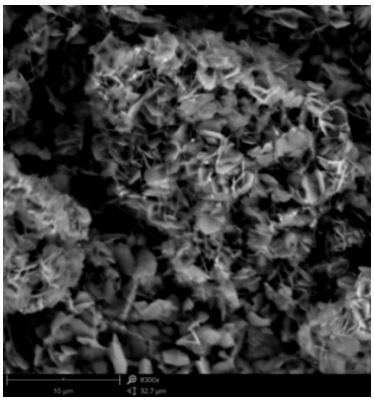

(22.9°C)

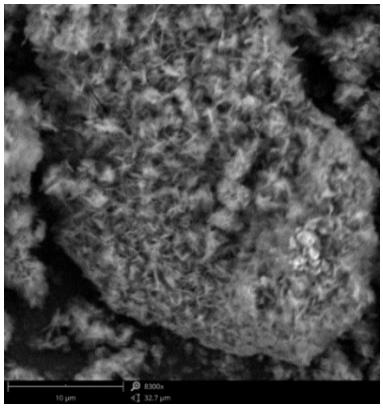

(23.5°C)

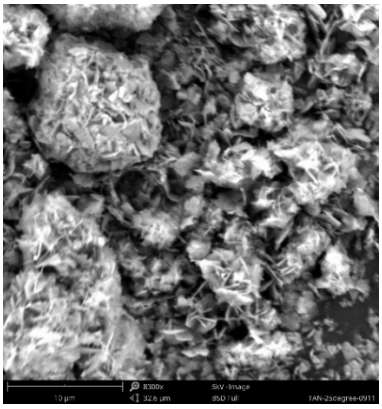

(25°C)

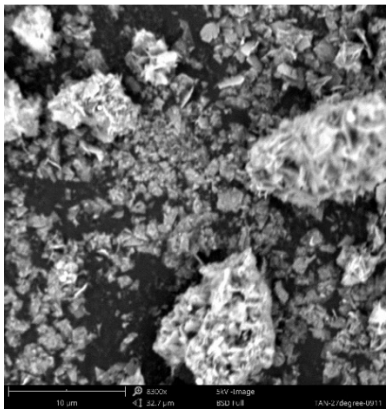

(27°C)

Figure 3-3: SEM images showing particle structure of TAN at temperature 22.5-27°C during seed mixing, recorded at 8300x.

4 Results and discussion – Membrane fabrication

4.1 Selecting the opening size of the stainless-steel mesh

The small-particle-filtering stainless steel wire cloth, has a tight weave that traps particles and provides strength for use in high-pressure and high-flow applications. As the selective layer of the membrane will be fabricated using filtration principles, the opening size of stainless-steel (SS) mesh is an important factor in determining if the nanoparticles can be deposited and stay on the surface of the mesh. Figure 4-1 shows the surface conditions of sintered SS meshes with opening size 26, 35, and 80 µm after TAN and silica binder deposition by gravity filtration. The properties of the meshes are listed in Table 2-1. As shown in Figure 4-1, it is clearly seen that there is almost no TAN retained on the filter at an opening size of 80 µm. When the opening size is as small as 26 µm, a thick filtration cake was formed that did not adhere to the mesh.

These differences can be explained by the filtration principles shown in Figure 4-2 showing the cross-section of meshes with different size openings. An individual TAN particle measures 4 x 1 µm and is 100 nm thick. The pores of the 80 µm-mesh are too large to hold up the nanoparticles, thus the TAN particles are not retained during the deposition process. When the opening size of the mesh is 26 µm, cake formation occurs on the mesh surface. The internal bridging of TAN particles forms a cake on the mesh.

Figure 4-2 is an illustration of TAN after deposition on stainless steel meshes for three different opening sizes (80, 35, 26 µm respectively from left to right). TAN is simplified as ‘T’ shaped particles, and the two disks represent the cross section of a pore in the mesh. The red curves represent the contact regions between TAN and the mesh.

As shown in Figure 4-2, at the mesh size of 80 µm, the TAN particles pass through the filter openings whereas they are retained for the other mesh sizes. By examining the area of binding between the TAN and the SS mesh for the 35 and 26 µm opening sizes, we can see that, for the 26 µm mesh, the contact area for surface adhesion is much smaller than the 35 µm mesh, thus the interaction force with the mesh is much smaller. For the 35 µm mesh, TAN has a greater chance of remaining on the surface after backflushing due to the increased contact surface for binding to the SS mesh.

Figure 4-3 shows SEM images of TAN particles supported on the SS mesh with silica after calcination at 800°C. The two SEM images show the TAN deposit condition SS mesh with an opening size of 10 µm and 35 µm. It can be seen that few TAN particles remained on the 10 µm mesh, while the pores in 35 µm mesh are fully packed with TAN particles.

The distribution and structure of the TAN layer on the SS mesh was also studied as a function of mesh size. Opening size describes the minimum particle size that the membrane will be able to reject, while the mesh size of a stainless-steel wire cloth indicates a specific dimension of the openings. Figure 4-4 shows the dimensions of 3 different meshes, 25, 26 and 35 µm listed in Table 2-1. The 25 µm size is commercially available but not tested in this work. The 35 µm mesh has the longest slit opening and offered a higher porosity than the 26 µm mesh. It is for these reason that the 35 µm mesh was selected for most of the membranes studied in this work.

(80 µm sintered)

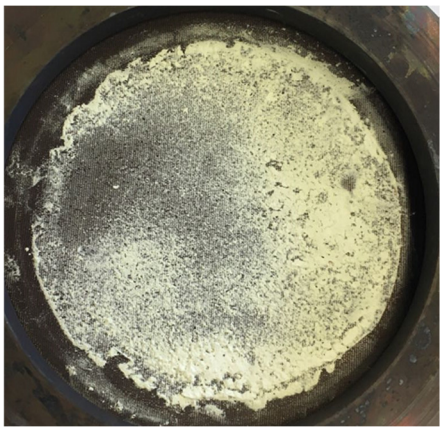

(35 µm sintered)

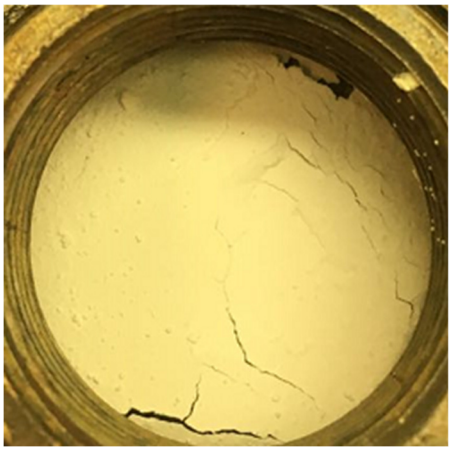

(26 µm)

(26 µm)

Figure 4-1: Surface conditions of sintered SS meshes with opening size 80, 35, and 26 µm after TAN and silica binder deposition by filtration.

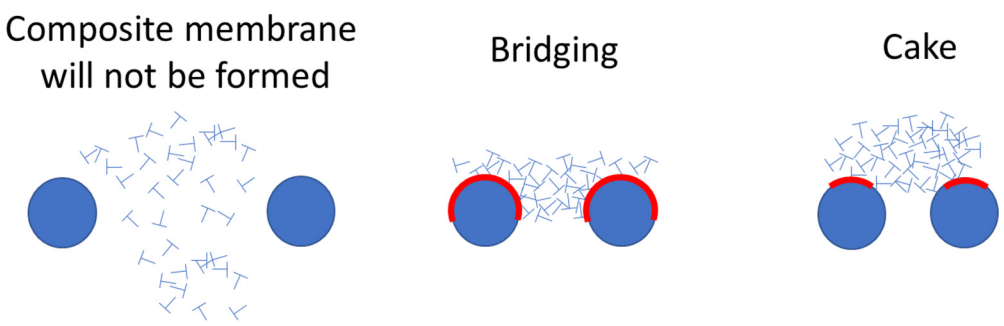

Figure 4-2: Membrane fabrication by filtration principles for three different opening sizes (80, 35, 26 µm respectively from left to right). The red line shows the surface area for binding.

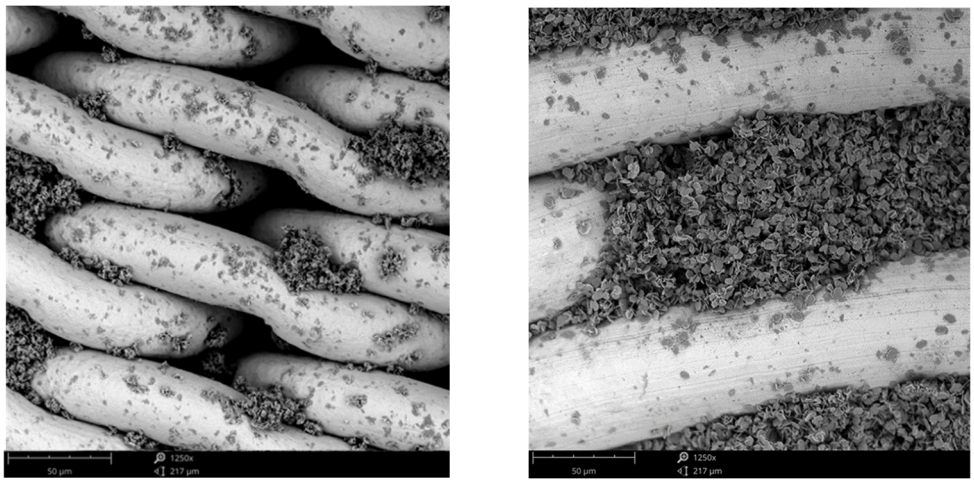

(10 µm) (35 µm)

Figure 4-3: SEM images of TAN particles supported on SS mesh with opening size 10 and 35 µm after TAN and silica binder deposition by filtration (recorded at 1250x), followed by sintering.

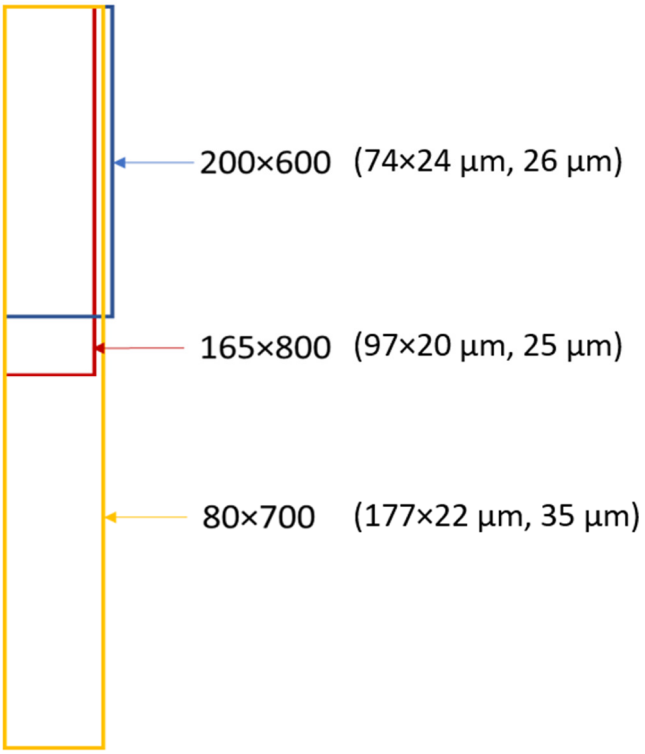

Figure 4-4: Schematics of the dimesion of three different meshes.

4.2 Pretreatment of SS support – Electrochemical etching

The surface morphology of the support material plays an important role in bonding with the TAN selective layer. As stainless steel is known for its smooth surface, etching is an effective way to form a micro/nanostructure on its wire surface. This creates more surface area and facilitates TAN deposition.

An electrolyte was prepared with 3.6wt% of HCl and 1.2wt% of HNO_3 mixed in a 1:1 volume ratio. A piece of mesh was immersed in the electrolyte and placed parallel to a conductive graphite

plate under a constant electric potential of 5V. In this work, the time it takes for etching a SS wire cloth was studied to get a re-entrant surface without causing too much damage to the SS wires.

Supports were etched for two different times, 4 min and 12 min, and characterized by SEM. Figure 4-5 shows the SEM images of SS wires that have been etched for 4 min and 12 min compared to the non-etched wire. It can be seen that the mesh that was etched for 12 minutes should be the best for TAN deposition, as it has the roughest surface. However, the mechanical strength of the mesh was dramatically weakened as evidenced by the ease with which it could be bent. As a compromise, 4 min was selected as the best etching time.

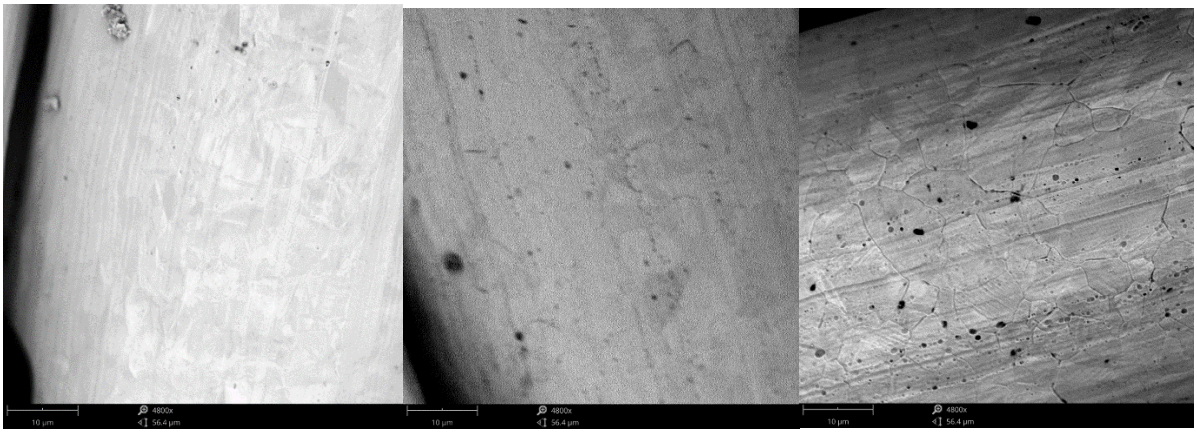

(non etched mesh) (etched for 4 min) (etched for 12 min)

Figure 4-5: SEM images showing meshes without etching and for 4 min and 12 min.

4.3 Sintering temperature

In this section, we determined the best sintering temperature for the synthetic membrane to facilitate the binding between stainless steel and deposited TAN using a silica binder. In sintering

various materials, such as metals, ceramics and plastics are fused together to create one solid piece by heating at a temperature lower than melting point of at least one of the components.

The melting points of alumina, silica and stainless steel are listed in Table 4-1.

Table 4-1 Melting points of materials used for sintering

Materials	Melting point (°C)
Alumina	2072
SiO_2	1710
316 Stainless steel	1371-1399

Figure 4-6 are SEM images showing the surface conditions of the stainless steel mesh after heating at 700, 800, 900 and 1000°C. These sample pieces were initially cut from the same membrane and sintered at different temperatures in the muffle furnace. The original membrane was prepared and deposited with the materials listed in Table 4-2.

To test the influence of sintering temperature on the mesh wires, the TAN suspension described in Table 4-2 was slowly and carefully poured over the mesh manually, to form a filter cake. The binder solution was then passed through the cake and SS support. After drying in a fume hood, it was cut into four pieces and sintered separately at four different temperatures for 4 hours. From Figure 4-6, at temperatures 900°C and 1000°C the wire surfaces were significantly oxidized and were no longer smooth compared to 700 °C. A sintering temperature of 800 °C was selected to minimize the damage to the SS supports and offer a reasonably high temperature to properly sinter silica between the TAN particles and onto the SS support.

Table 4-2: The contents of TAN suspended solution and binder solution

TAN suspended solution		Binder solution	
TAN	0.14 g	Binder SiO_2 sol	50g
DI water	15ml	DI water	130
Ethanol	15ml	Binder content	10wt%
		Ethanol	20g
		Ethanol content	10wt%

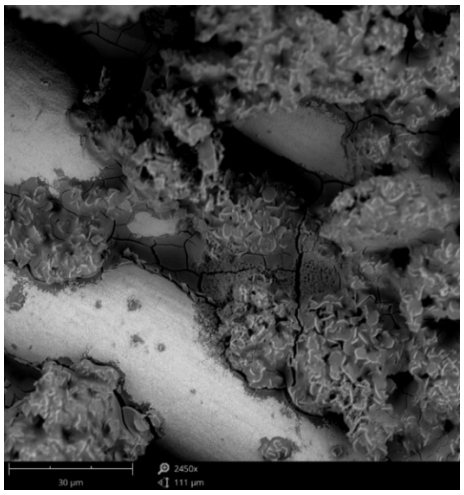

(700°C)

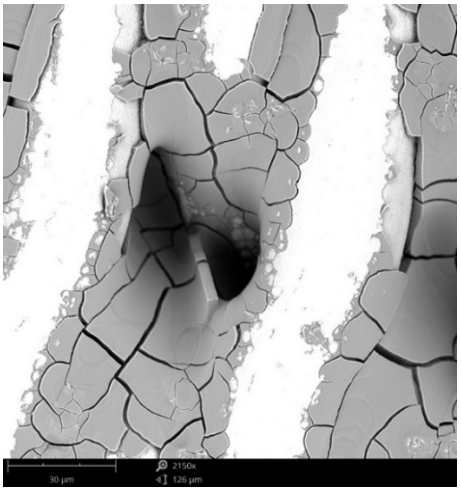

(800°C)

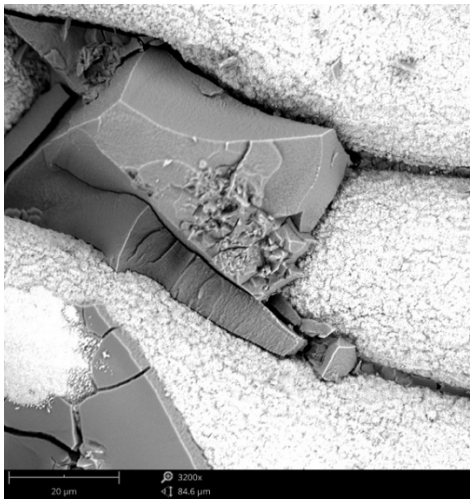

(900°C)

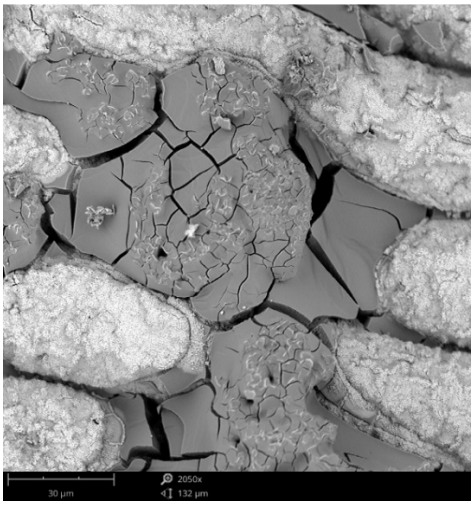

(1000°C)

Figure 4-6: SEM images showing synthetic membrane surface conditions at sintering temperature 700, 800, 900 and 1000°C.

5 Results and discussion- Permeability experiments

5.1 Permeability experiments for membranes with TAN supported on stainless-steel meshes using silica as binding agent

The synthesized filters were challenged with a suspension of distilled and deionized water containing 10 ppm of bentonite under a constant transmembrane pressure of 100 mbar. The filters were produced by depositing 0.1g TAN at different silica binder concentrations (2.5wt%, 5wt%, 7.5wt%). The filter was backflushed after 15 min of permeation. As shown in Figure 5-1, for TAN on 35µm stainless-steel mesh support using 2.5wt% of silica as the binding agent. Figure 5-2 represents the retention of bentonite by the membrane. The maximum permeate flux generally occurs at the beginning of each backflushing cycle. Since backflushing washes away most of the retained bentonite, the pores are cleaner and open at that moment. The initial flux after backflushing declines with each subsequent backflush over the 4-hour run. This indicates that the TAN was successfully retained on the SS support. The permeate flux drops rapidly between backflushings as the filtration proceeds. The rapid flux decline is due to the accumulation of bentonite on the surface of the membrane [65].

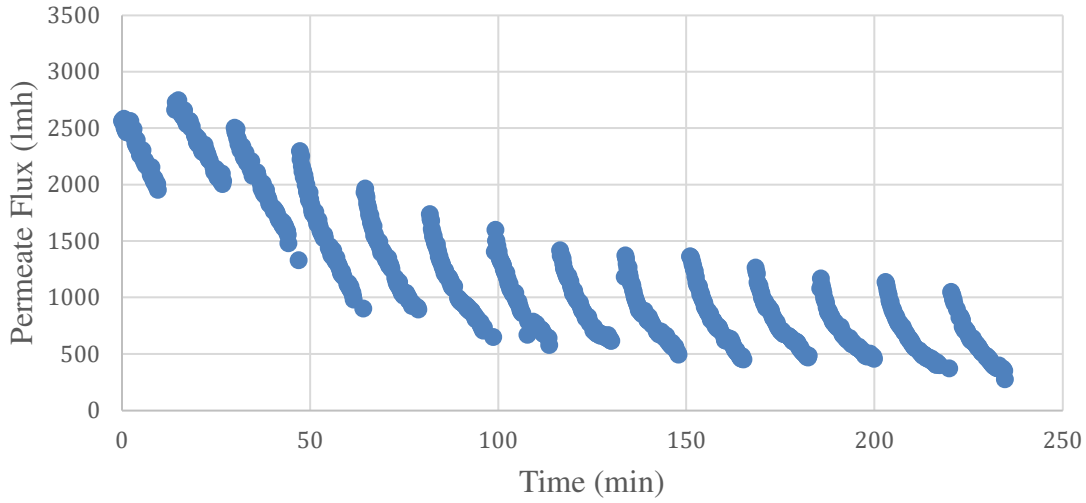

Figure 5-1: Flux curve for TAN on 35µm stainless-steel mesh support using 2.5wt% of silica as the binding agent.

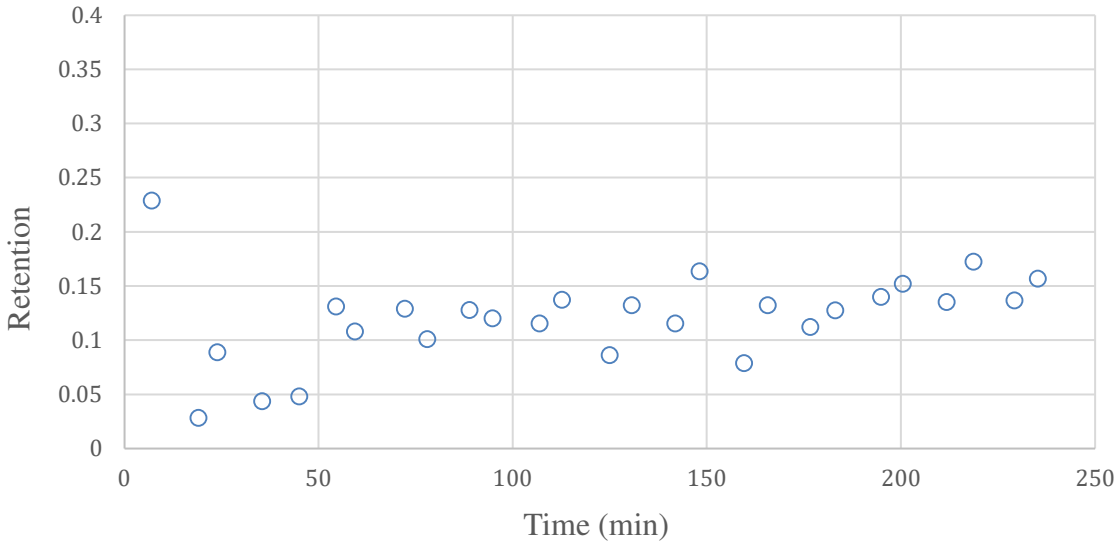

Figure 5-2: Retention for TAN on 35 µm stainless-steel mesh support using 2.5wt% of silica as the binding agent

A better understanding of the filtration process can be obtained by modeling the flux decline data with classic filtration models. There are four basic filtration models for constant pressure filtration: the complete blocking model, intermediate blocking model, pore constriction model, and cake filtration model. Illustrations and equations for these fouling mechanisms, given by Peng and Tremblay, are shown in Table 5-1 [65].

Table 5-1: Classic filtration models

Filtration model	Equation	Schematic
Complete blocking	$\frac{J_v}{J_0} = \exp(-K_{block}t)$	
Intermediate blocking	$\frac{J_v}{J_0} = (1 + K_{inter}t)^{-1}$	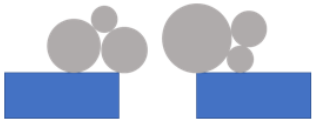
Pore constriction	$\frac{J_v}{J_0} = (1 + K_{cons}t)^{-2}$	
Cake filtration	$\frac{J_v}{J_0} = (1 + K_{cake}t)^{-1/2}$	

The model offering the best fit to the data can be determined from the root mean-squared error (RMSE), defined as the square root of the mean square error divided by the number of data points modeled. Table 5-2 shows three flux decline intervals at the beginning, middle, and end of the 4 hour run. Figure 5-3, Figure 5-4, Figure 5-5 present the results of applying different models to the

filter of TAN on stainless-steel mesh support using 2.5wt% of silica as the binding agent at the three fitted backflushing cycles. Therefore, the filtration mechanisms for the membrane at different stages can be estimated from the modeling results. The best fit for the initial cycle was the pore constriction model, while intermediate blocking occurred at middle and final stages. The results indicate that the bentonite particles were deposited on pore walls at the beginning of the run but gradually more particles settled onto the other ones and blocked the membrane pores. Generally, cake formation occurs in the late stages of filtration. Since cake filtration was not observed in both middle and final stages, this further demonstrates that the backflushing provided a very deep form of cleaning where pores were totally open and intermediate pore blocking could occur.

Table 5-2: Modeling results for TAN on stainless-steel mesh support using 2.5wt% of silica as the binding agent.

Fitting interval	Root mean squared error (RMSE) (L/m^2h)			
	Complete blocking	Intermediate blocking	Pore constriction	Cake filtration
Initial stage (14.98-26.73 min)	0.01311	0.01337	<u>0.01308</u>	0.01468
Middle stage (99.23-113.53 min)	0.03967	<u>0.01461</u>	0.02503	0.02046
Final stage (203.31-217.28 min)	0.04179	<u>0.01250</u>	0.02429	0.02440

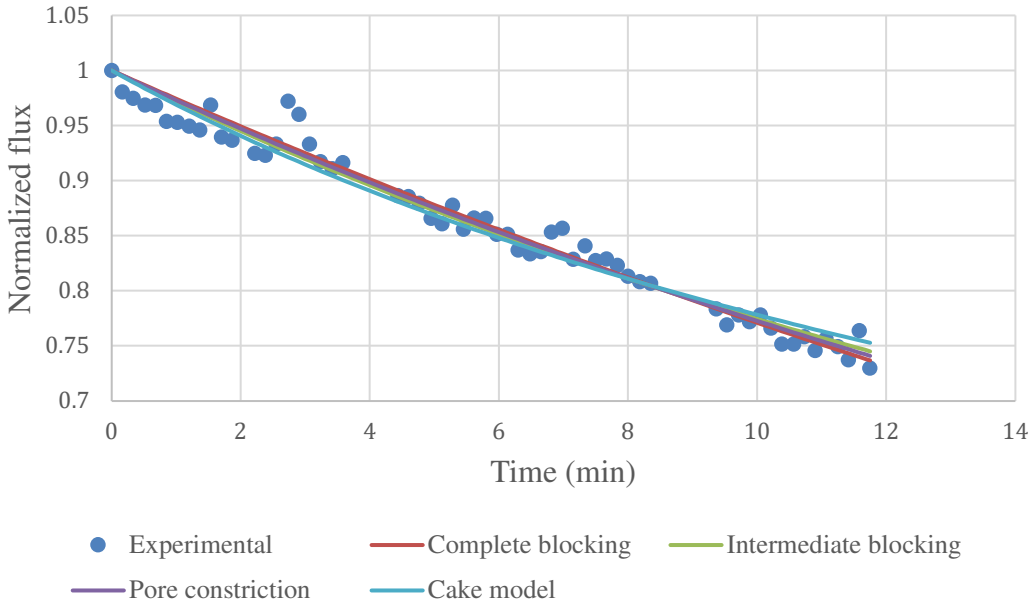

Figure 5-3: Experimental flux data at initial stage (14.98 min-26.73 min) and models fitted to the data for membrane with 2.5wt% silica.

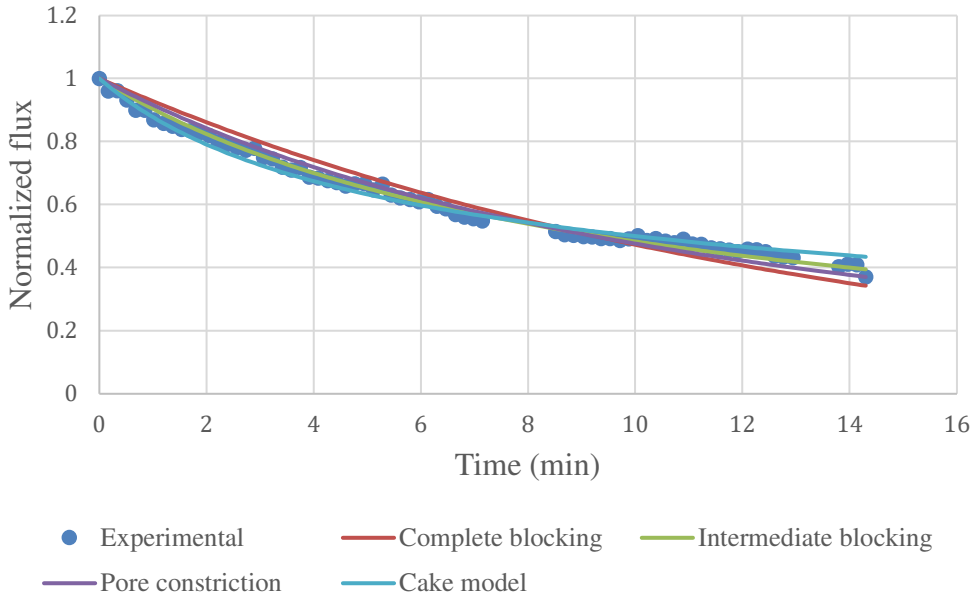

Figure 5-4: Experimental flux data at middle stage (99.23 min -113.53 min) and models fitted to the data for membrane with 2.5wt% silica.

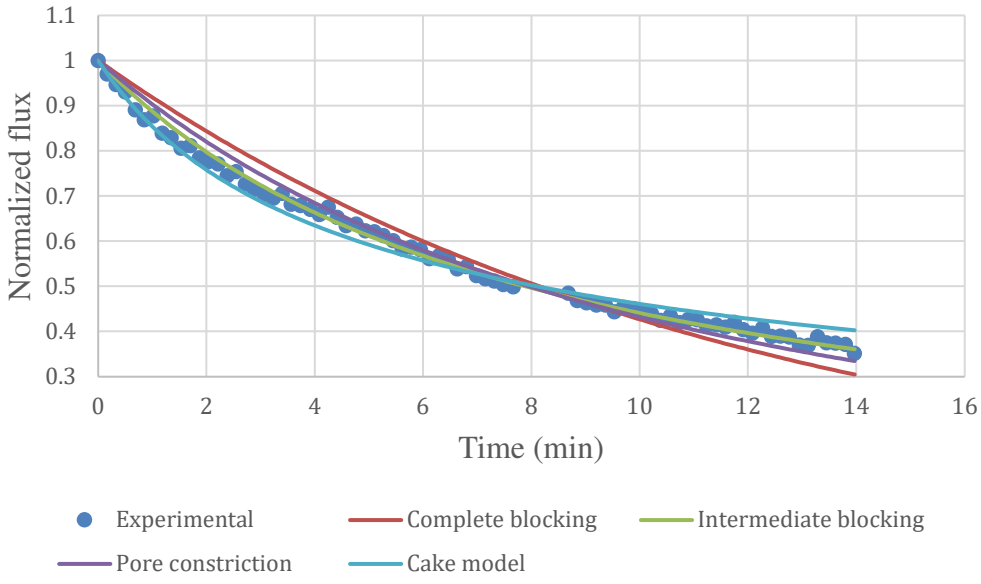

Figure 5-5: Experimental flux data at final stage (203.31 min-217.28 min) and models fitted to the data for membrane with 2.5wt% silica.

Figure 5-7 and Figure 5-9 shows the permeate flux curves for the membranes of TAN on stainless-steel mesh support using 5wt% and 7.5wt% of silica as the binding agent. As in the case of the 2.5wt% silica membrane, the initial flux after backflushing declines with each subsequent backflush over the 4-hour run. This indicates that the TAN was successfully retained on the SS support. Compared to 2.5wt% silica and 5wt% silica membranes, the initial permeate flux of 7.5wt% silica membrane was about half of the other two as a high concentration of silica as the binding agent would cover a large portion of the mesh support and reduce membrane permeability. The retention of the three membranes are shown in Figure 5-2, Figure 5-8 and Figure 5-10.

The turbidity of dilute (< 30 ppm) bentonite solutions was found to correlate linearly with concentration with an intercept of zero. The turbidity of the feed and permeate were measured to calculate the retention by the following equation.

$$\%\text{Retention} = \frac{F_t - P_t}{F_t}$$

Where, Ft = Feed turbidity (NTU), Pt = Permeate turbidity (NTU).

The retention of bentonite was used to estimate the value of the effective pore size of the membrane. Figure 5-6 is the particle size distribution of bentonite prior to filtration. The area under the particle size distribution curve (Figure 5-6) was used to determine the effective pore size of the membrane. The percentage of particles in the distribution passing through the membrane was taken as ((1-Retention) ×100 %). It can be represented as the cumulative area of each measured particle size passing through the membrane to the sum of the whole area under the curve (Figure 5-6). In this way, the effective pore size of the synthesized membrane can be estimated for a given retention. Since the bentonite particle size ranges from 0.06 µm to 0.7 µm, the effective pore size of the 2.5wt%, 5wt% and 7.5wt% silica membranes were determined as 0.53 µm (retention of 12%), >0.7 µm, 0.62 µm (retention of 2%), respectively.

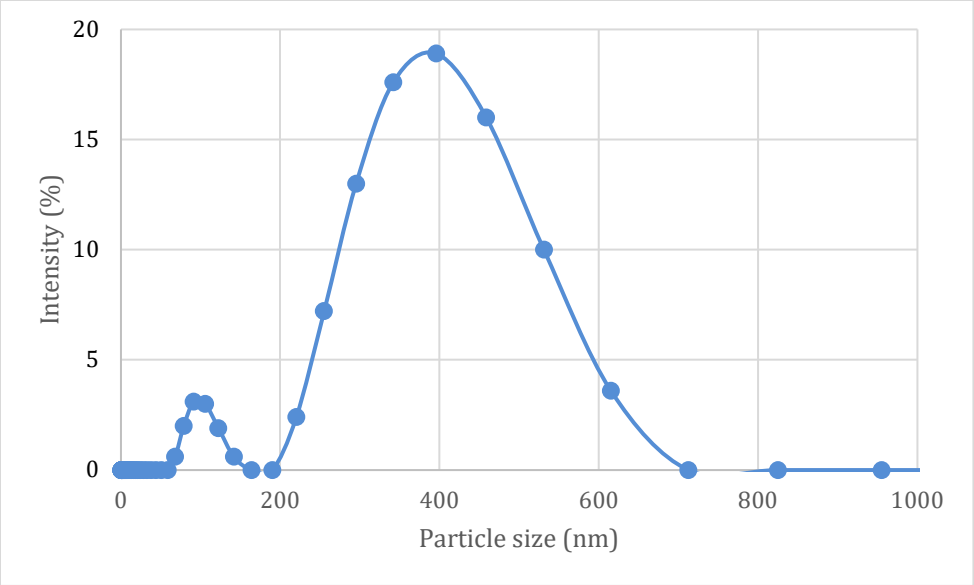

Figure 5-6: Particle size distribution of the 10 ppm bentonite feed solution determined by dynamic light scattering.

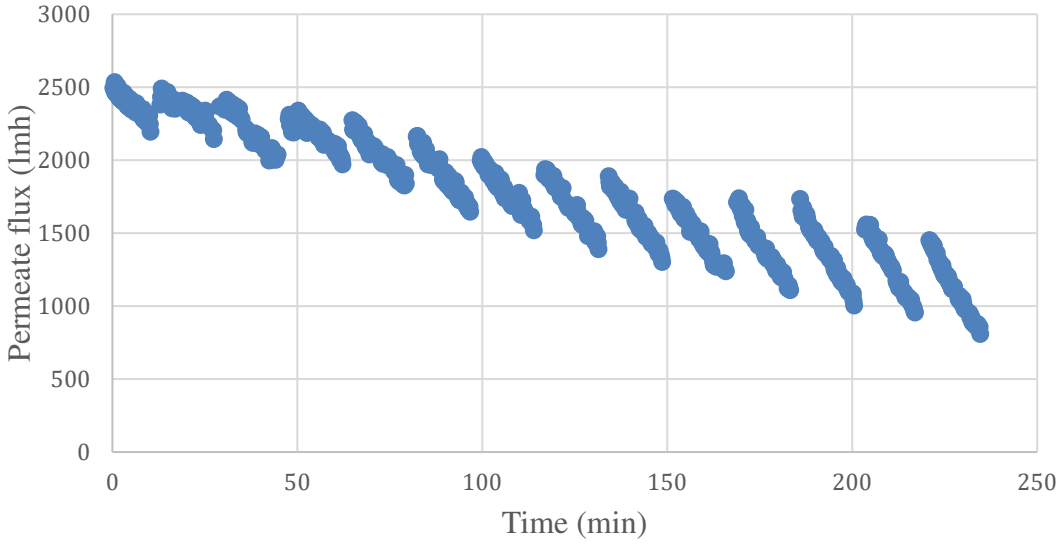

Figure 5-7: Flux curve for TAN on 35µm stainless-steel mesh support using 5wt% of silica as the binding agent.

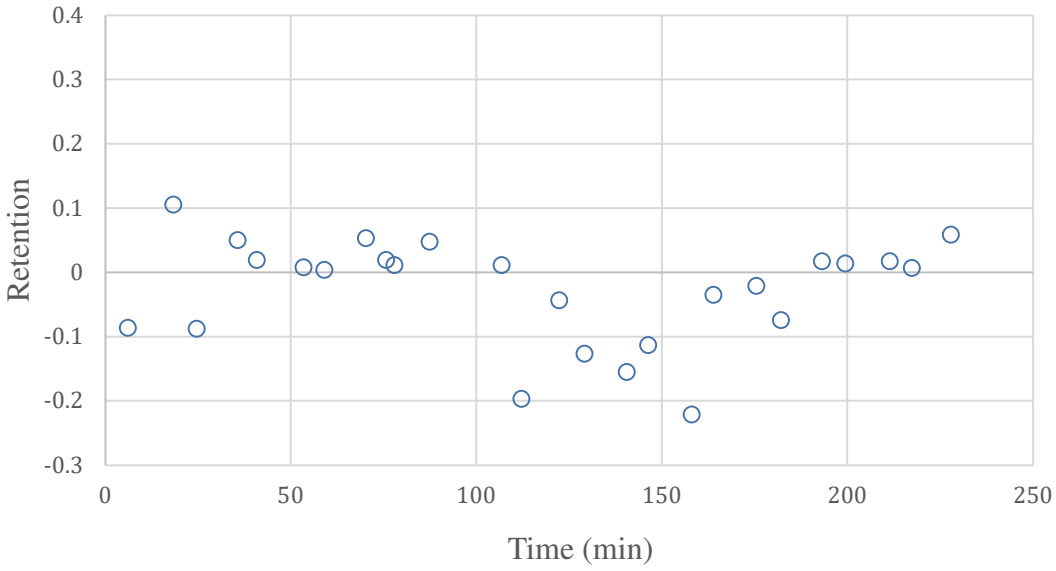

Figure 5-8: Retention for TAN on 35µm stainless-steel mesh support using 5wt% of silica as the binding agent.

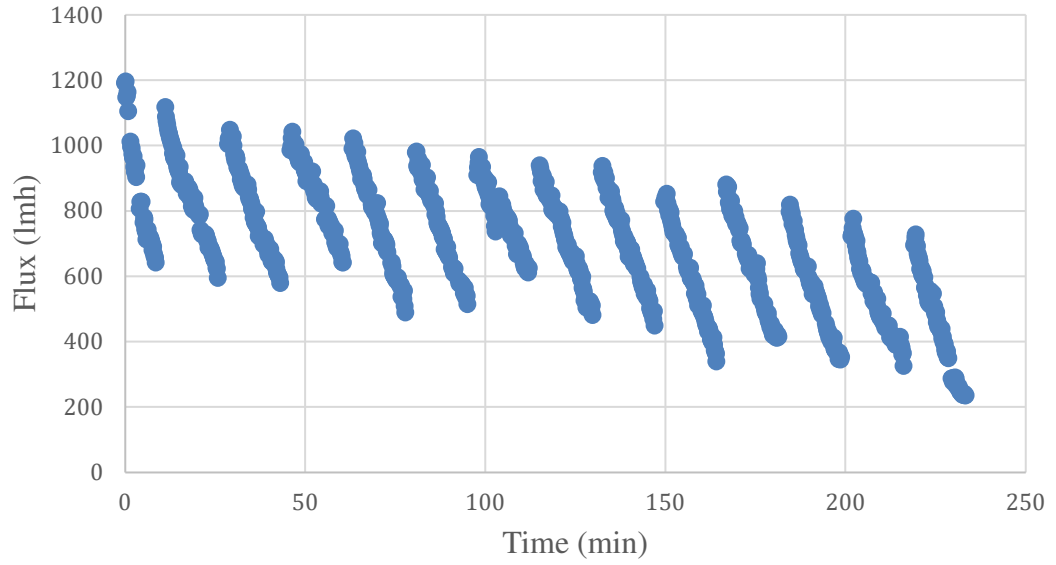

Figure 5-9: Flux curve for TAN on 35µm stainless-steel mesh support using 7.5wt% of silica as the binding agent.

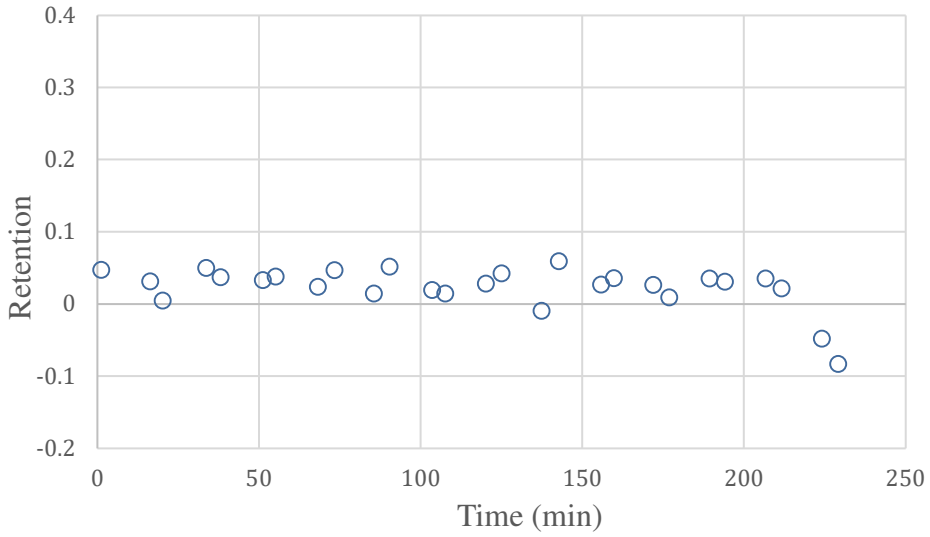

Figure 5-10: Retention for TAN on 35µm stainless-steel mesh support using 7.5wt% of silica as the binding agent.

The plots of experimental data with 4 model predictions for all of the membranes can be found in Appendix A. The modeling results and best fit of 5wt% silica membrane and 7.5wt% silica membrane at different time stages are listed in Table 5-3 and Table 5-4. Cake filtration occurred during the tests for both membranes, as more bentonite particles are retained on the surface of the membrane with higher concentrations of silica binder. This indicates that less particles enter the membrane pores at these increased concentrations of silica binder.

Table 5-3: Modeling results for TAN on stainless-steel mesh support using 5wt% of silica as the binding agent.

Fitting interval	Root mean squared error (RMSE) (L/m^{2}h)			
	Complete blocking	Intermediate blocking	Pore constriction	Cake filtration
Initial stage (13.27-27.4 min)	0.01660	0.01638	0.01649	<u>0.01617</u>
Middle stage (99.72-113.85 min)	0.01625	0.01519	0.01565	<u>0.01468</u>
Final stage (203.73-216.85 min)	<u>0.01422</u>	0.02103	0.01757	0.02774

Table 5-4: Modeling results for TAN on stainless-steel mesh support using 7.5wt% of silica as the binding agent.

Fitting interval	Root mean squared error (RMSE) (L/m^{2}h)			
	Complete blocking	Intermediate blocking	Pore constriction	Cake filtration
Initial stage (11.23-25.72 min)	0.02378	<u>0.01887</u>	0.02047	0.02051
Middle stage (98.28-111.92 min)	0.02989	<u>0.02853</u>	0.02901	0.02856
Final stage (202.18-216.13 min)	0.04403	0.02850	0.03522	<u>0.02304</u>

In an attempt to reduce the effective pore size of the membrane, a coating of TAN was applied to a previously coated and sintered membrane. Figure 5-11 is the permeate flux curve for the double coated membrane. It was coated with 0.078g TAN and 10wt% silica, followed by a second coating with 0.0029g TAN and 5wt% silica. From Figure 5-12, the retention increases compared to the

single coated membranes shown above. The retention is 15%, which corresponds to an effective pore size of 0.52 µm.

The modeling results and best fits for the double coated membrane is shown in Table 5-5. Bentonite particles were deposited on pore walls at the beginning of the filtration, followed by intermediate blocking at the middle stage and final stage, which implies that pores were cleaned and open once backflushed.

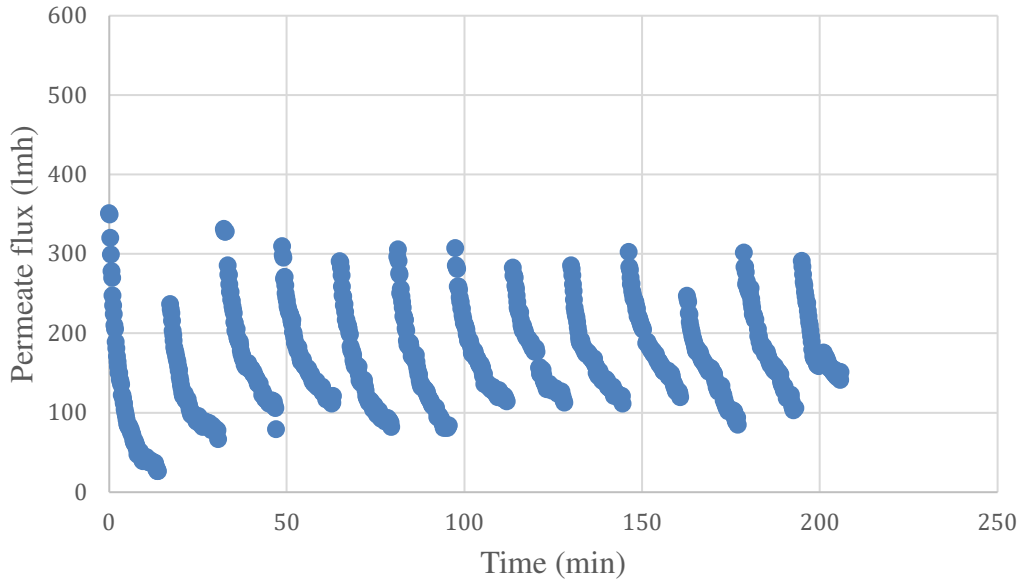

Figure 5-11: Flux curve for the double coated membrane (first layer of 0.078g TAN, 10wt% silica and second layer of 0.0029g TAN and 5wt% silica) on 26µm stainless-steel mesh support.

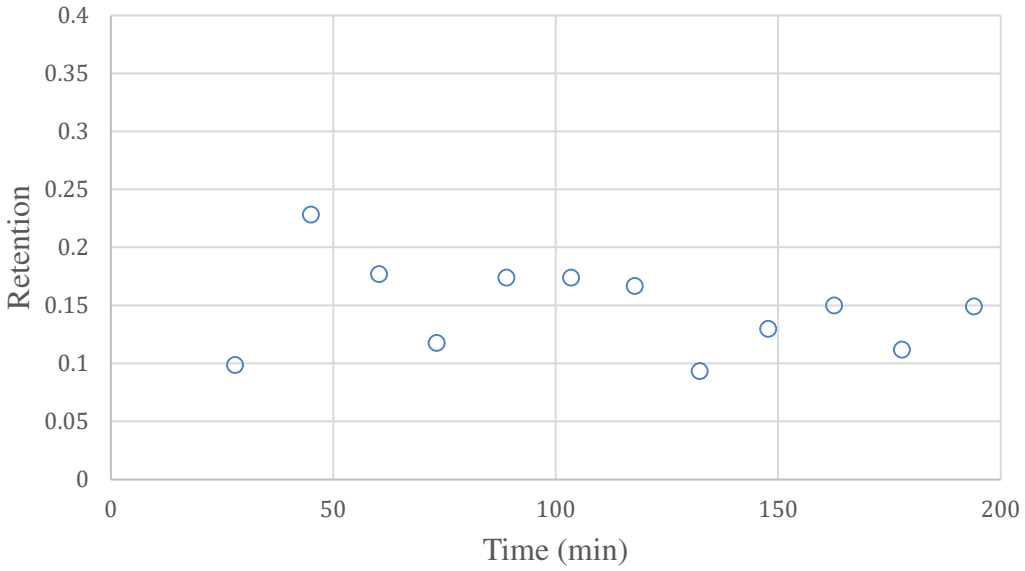

Figure 5-12: Retention for the double coated membrane (first layer of 0.078g TAN, 10wt% silica and second layer of 0.0029g TAN and 5wt% silica) on 26µm stainless-steel mesh support.

Table 5-5: Modeling results for the double coated membrane (first layer of 0.078g TAN, 10wt% silica and second layer of 0.0029g TAN and 5wt% silica) on 26µm stainless-steel mesh support.

Fitting interval	Root mean squared error (RMSE) (L/m^{2}h)			
	Complete blocking	Intermediate blocking	Pore constriction	Cake filtration
Initial stage (0-13.78 min)	0.04479	0.03664	<u>0.01222</u>	0.08520
Middle stage (81.28-95.58 min)	0.05722	<u>0.02122</u>	0.03434	0.03424
Final stage (178.63-193.11 min)	0.04126	<u>0.02048</u>	0.02785	0.02816

5.2 Permeability experiments for membranes with TAN supported on stainless-steel mesh using silver as a binding agent

The synthesized filters were challenged with 10 ppm of bentonite under 100 mbar. The filters were coated with 0.05g TAN and different amounts of colloidal silver (0.025g and 0.05g), each followed by 4 hours of calcination at 500°C. Figure 5-13 and Figure 5-15 are the permeate flux curves for the membranes. The observed fluxes for these membranes are extremely high. It can also be seen that there are no particles retained on the membranes as flux curves do not decline after subsequent backflushing cycles. The measured retention presented in Figure 5-14 and Figure 5-16 are quite low and sometimes negative. The negative observations represent particles being released form the membrane. It can be concluded that colloidal silver is not a good binding agent for TAN and stainless steel.

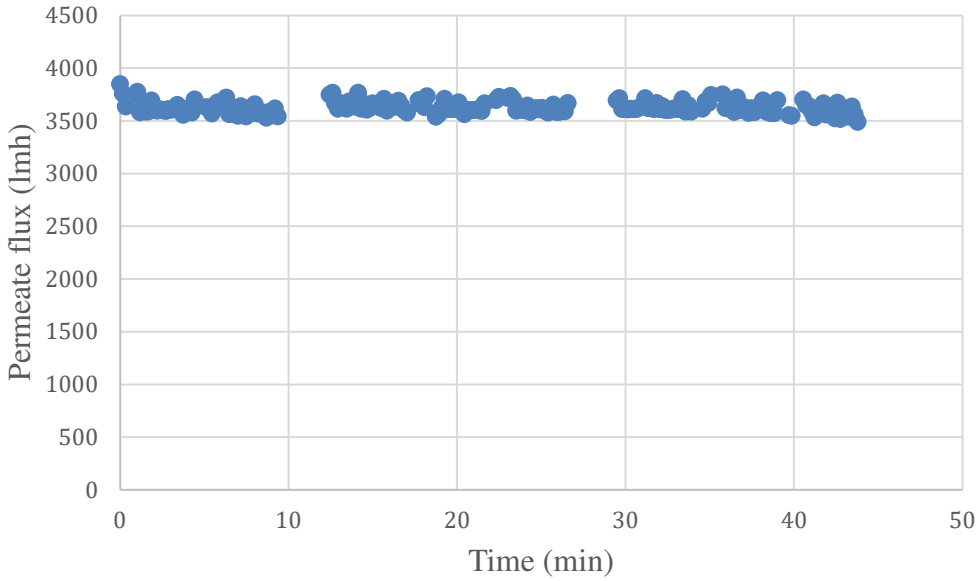

Figure 5-13: Flux curve for TAN on 35µm stainless-steel mesh using 0.025g silver as binding agent.

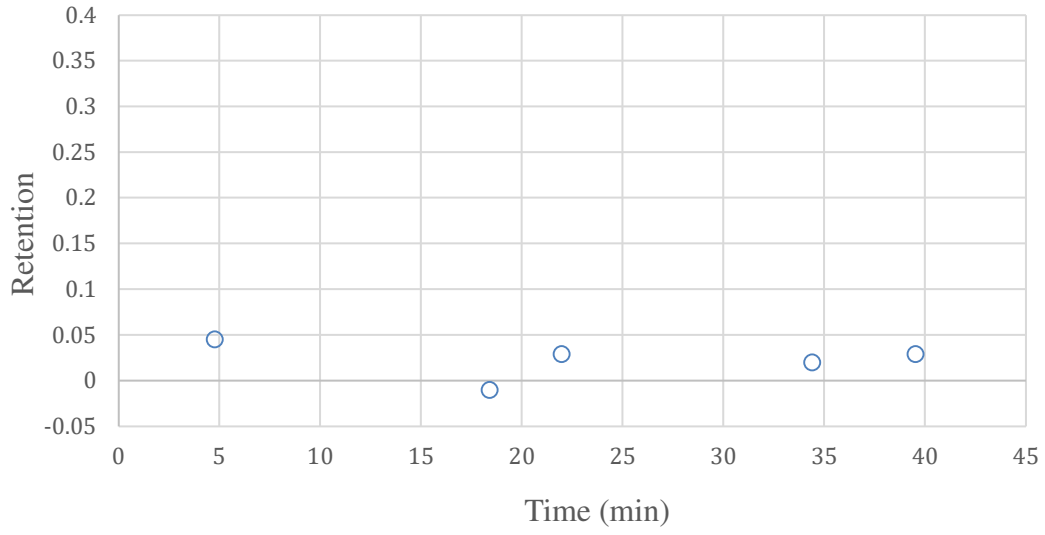

Figure 5-14: Retention for TAN on 35µm stainless-steel mesh using 0.025g silver as binding agent.

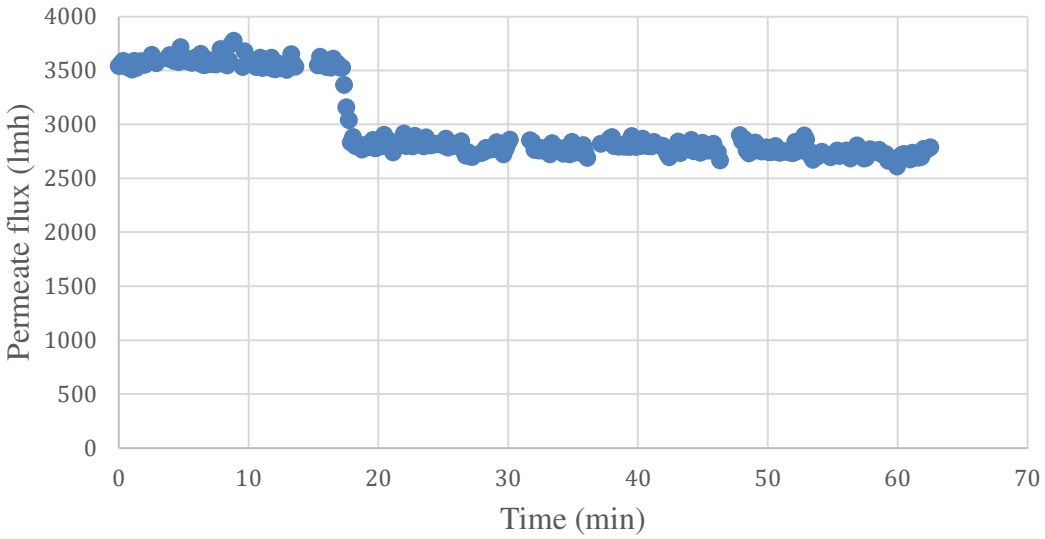

Figure 5-15: Flux curve for TAN on 35µm stainless-steel mesh using 0.05g silver as binding agent.

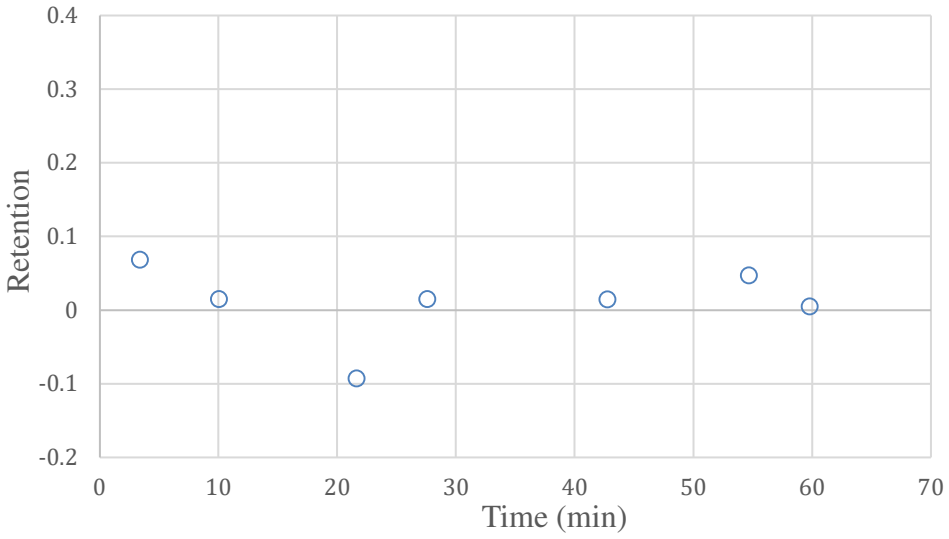

Figure 5-16: Retention for TAN on 35µm stainless-steel mesh using 0.05g silver as binding agent.

In an attempt to decrease the effective pore size of the membrane, a second coating of silver was applied to an already sintered membrane. Figure 5-17 shows the permeate flux curve of the membrane with two silver coatings (first layer was with 0.1g TAN and 0.0267g Ag_2O; Second layer was with 0.1g Ag_2O only). As in the case of the silica membranes, the initial flux after backflushing declines with each subsequent backflush over the 4 hour run. This indicates that the TAN was successfully bound to the stainless steel support and bentonite particles were retained by the membrane. However, the retention presented in Figure 5-18 is below zero as a result of materials being released from the membrane. This further demonstrated that silver was a weak binder to join TAN with stainless steel. Cake filtration is the primary filtration mode (Table 5-6) for the membrane of TAN with double Ag_2O coatings. The materials that were released from the membrane were mixed with bentonite solution in the feed after backflushing, leading to a large

number of particles accumulating on the membrane surface. This will be further illustrated by the SEM analysis of the membranes.

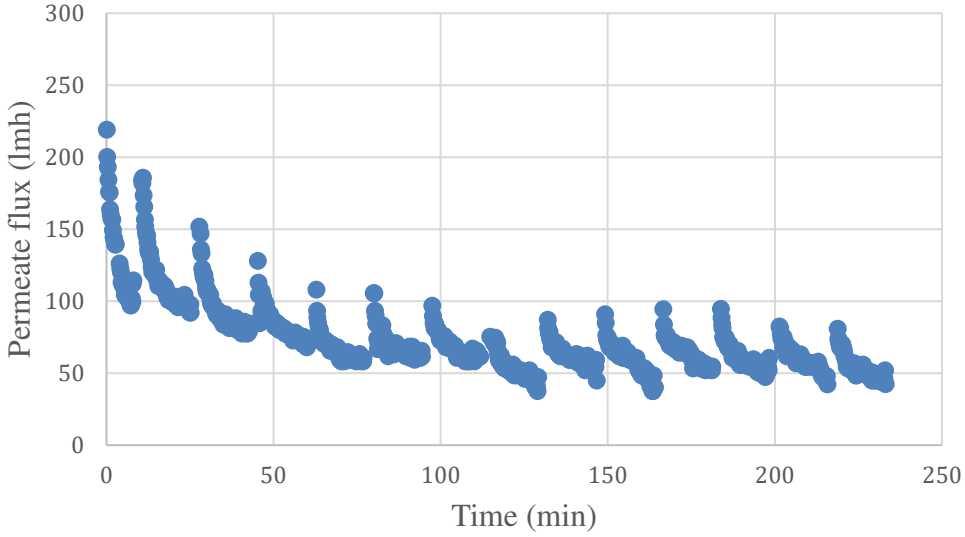

Figure 5-17: Flux curve for TAN with double Ag_2O coatings (first layer was with 0.1g TAN and 0.0267g Ag_2O ; second layer was with 0.1g Ag_2O only) on 35µm SS mesh.

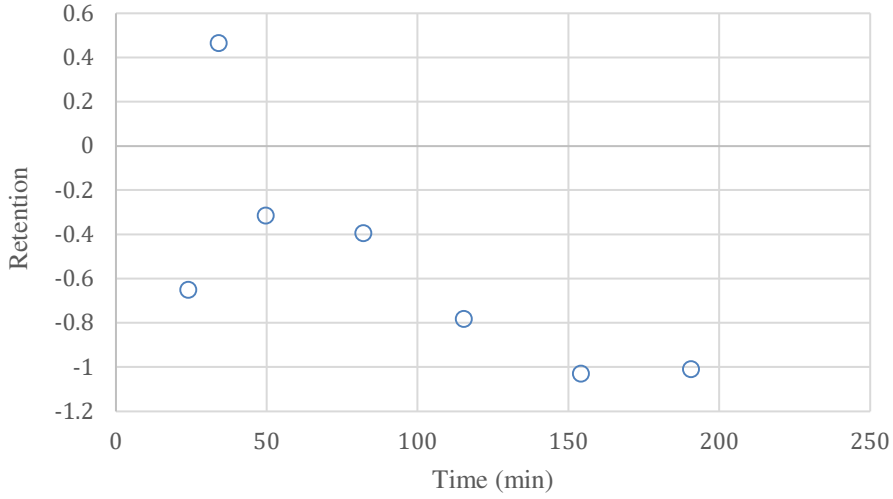

Figure 5-18: Retention for TAN with double Ag_2O coatings (first layer was with 0.1g TAN and 0.0267g Ag_2O ; second layer was with 0.1g Ag_2O only) on 35µm SS mesh.

Table 5-6: Modeling results for TAN with double Ag_2O coatings (first layer was with 0.1g TAN and 0.0267g Ag_2O ; second layer was with 0.1g Ag_2O only) on 35µm SS mesh.

Fitting interval	Root mean squared error (RMSE) (L/m^2h)			
	Complete blocking	Intermediate blocking	Pore constriction	Cake filtration
Initial stage (10.88-25.15 min)	0.10267	0.07640	0.08894	0.05462
Middle stage (97.43-111.72 min)	0.08104	0.06693	0.07374	0.05482
Final stage (201.3-215.62 min)	0.06170	0.05132	0.05625	0.04310

5.3 Permeability experiments using ceramic supports

5.3.1 Commercial ceramic membrane

A commercial ceramic membrane having a 1.4 µm pore size determined by mercury porosimetry (Sterlitech 47M140) was also tested using 10 ppm of bentonite under 100 mbar. Figure 5-19 and Figure 5-20 are the flux curve and retention of this membrane.

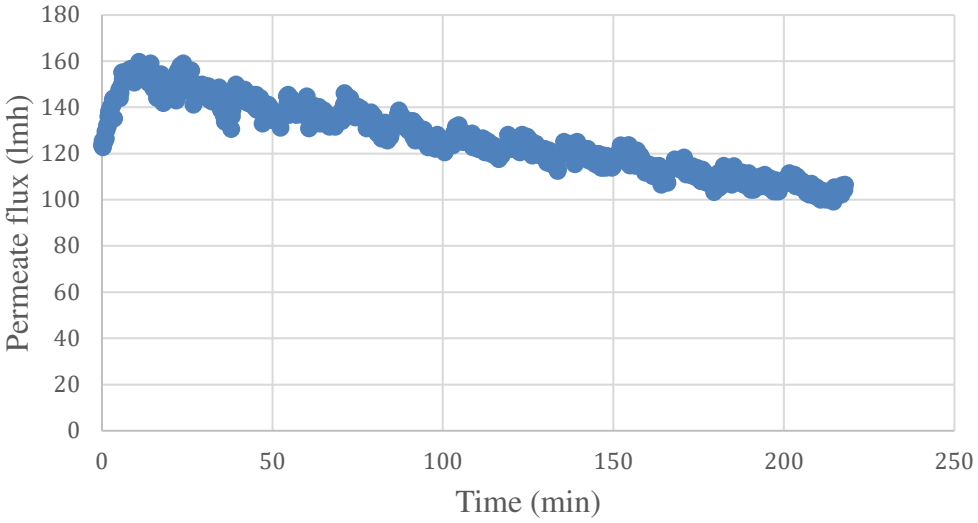

Figure 5-19: Flux curve for 1.4 µm ceramic membrane

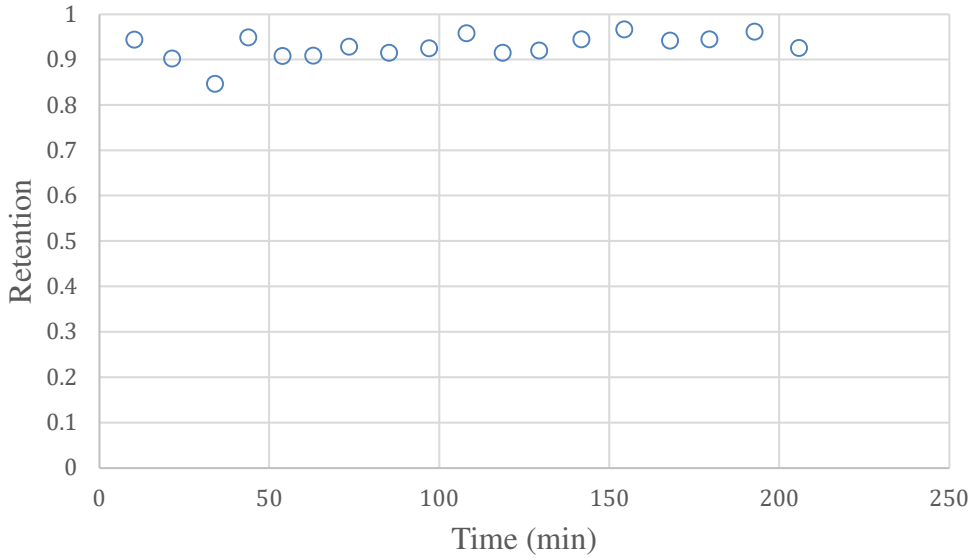

Figure 5-20: Retention for 1.4 µm ceramic membrane

The average retention from Figure 5-20 was 93%, indicating that particles of 0.26 µm and greater were retained by the membrane. The effective pore size of the membrane was reduced by the formation of a cake on the surface of the membrane and the retention of particles in the selective

layer and support of the membrane. This caused a reduction in effective pore size from 1.4 µm measured by Hg- porosimetry to 0.26 µm measured from particle size analysis.

5.3.2 Membranes made with TAN on ceramic supports

The surface of a commercial Sterlitech membrane 47M140 was sanded down to expose the support layer. TAN suspensions with amounts of 0.013g and 0.05g were mixed with a silica binder, then the mixtures were deposited on ceramic supports, followed by 4 hours of calcination at 1000°C. The filters were challenged with 10 ppm of bentonite. Figure 5-21, Figure 5-22 and Figure 5-23 are the flux curves and retention versus time of TAN on ceramic supports. The average retention of the membrane of 0.013g TAN (5wt% silica) on ceramic support was approximately 60%, indicating an effective pore size of 0.38 µm, and it was 66% for the 0.05g TAN (10wt% silica) membrane, so the effective pore size of the second membrane was estimated as 0.37 µm.

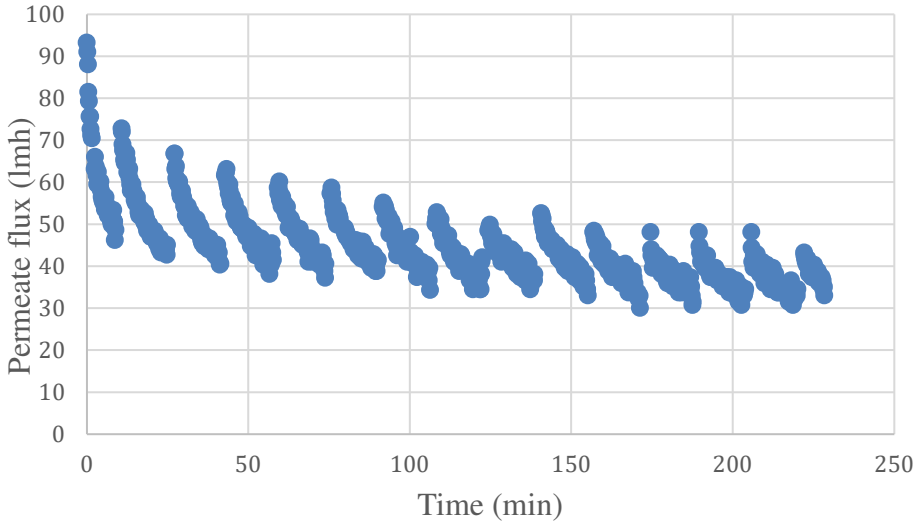

Figure 5-21: Flux curve for 0.013g TAN and 5wt% silica on a ceramic support.

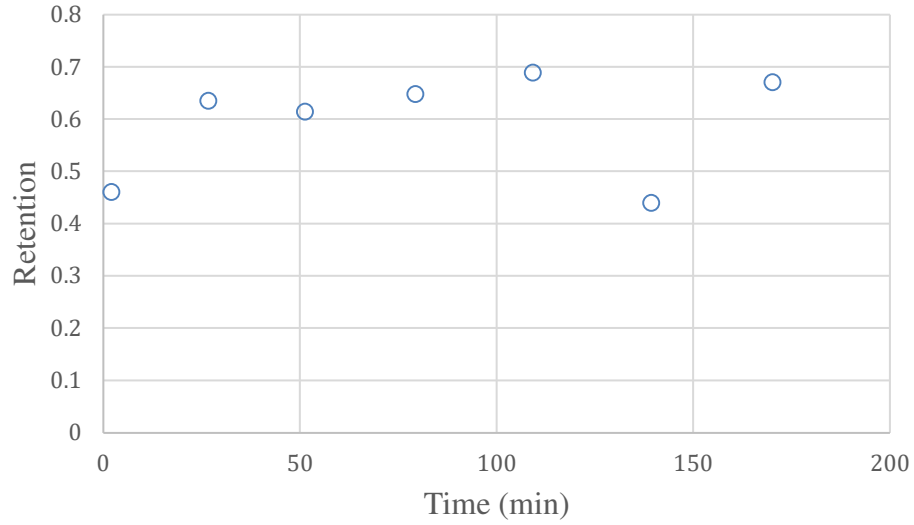

Figure 5-22: Retention for 0.013g TAN and 5wt% silica on a ceramic support.

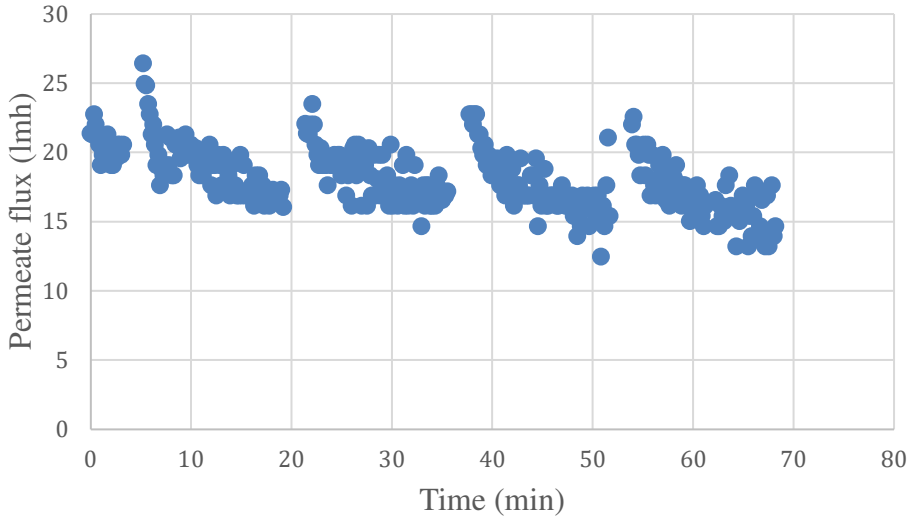

Figure 5-23: Flux curve for 0.05g TAN and 10wt% silica on the ceramic support.

The modeling results and best fits of TAN on ceramic supports are shown in Table 5-7 and Table 5-8. Cake filtration was the primary mode of filtration for the two membranes throughout the process. They had better retention than the membranes mentioned above and the particles mostly accumulated on the surface of the membrane as evidenced by the data fitting the cake filtration mechanism for both membranes, see Table 5-7 and Table 5-8.

Table 5-7: Modeling results for 0.013g TAN and 5wt% silica on ceramic support

Fitting interval	Root mean squared error (RMSE) (L/m^2h)			
	Complete blocking	Intermediate blocking	Pore constriction	Cake filtration
Initial stage (10.72-24.85 min)	0.04209	0.02912	0.03528	0.01915
Middle stage (108.33-121.95 min)	0.03513	0.02965	0.03221	0.02566
Final stage (205.75-219.9 min)	0.06658	0.05907	0.06270	0.05256

Table 5-8: Modeling results for 0.05g TAN and 10wt% silica on the ceramic support.

Fitting interval	Root mean squared error (RMSE) (L/m^2h)			
	Complete blocking	Intermediate blocking	Pore constriction	Cake filtration
Initial stage (5.22-19.17 min)	0.09206	0.08211	0.08692	0.07337
Middle stage (22.07-35.52 min)	0.08654	0.08103	0.08371	0.07614
Final stage (37.72-51.68 min)	0.07424	0.06749	0.07072	0.06191

6 Results and discussion- SEM characterization

SEM images were taken to characterize the synthesized membranes supported on stainless- steel mesh or ceramics after the filtration of a 10 ppm bentonite suspension. A complete list of magnified images can be found in Appendix B.

6.1 TAN supported on SS mesh using silica as a binder

Figure 6-1 and Figure 6-2 compare of TAN supported membranes on SS mesh, using silica as the binding agent (2.5wt%, 5wt%, 7.5wt%), measured at 4800x and 2000x. It can be seen that the porosity of the selective layer decreased with increasing silica binder concentration. This corresponds to the results in Section 5.1 as the permeability is reduced with increasing silica binder content. TAN with 2.5wt% and 5wt% silica binder retained the twinned structure of TAN and maintained the slit pore configuration after successive backflushings, while TAN reinforced by 7.5wt% silica tends to present a loss of 3D structure as the silica filled-in the pores between nanoplatelets.

Figure 6-3 shows the SEM image of double coated membrane (first layer of 0.078g TAN, 10wt% silica and second layer of 0.0029g TAN and 5wt% silica) on 26μm stainless-steel mesh support. The double coated membrane presents better retention than single coated membrane, as observed in Section 5.1. The SEM analysis further proves that silica content higher than 7.5wt% is excessive in binding TAN with stainless steel mesh.

(2.5wt% silica)

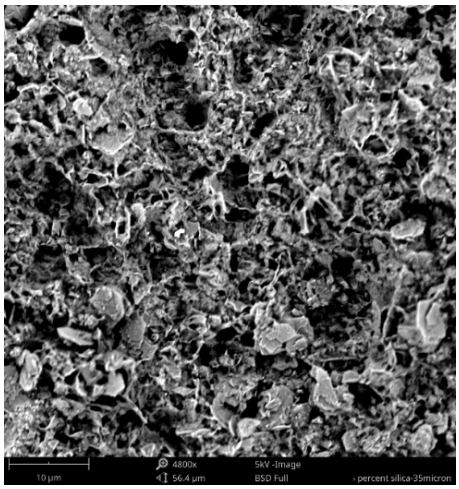

(5wt% silica)

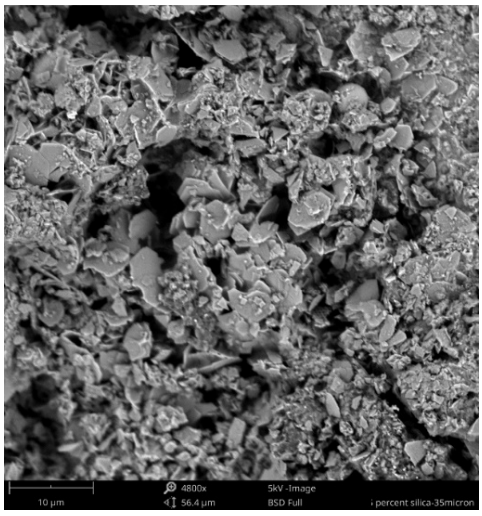

(7.5wt% silica)

Figure 6-1: TAN on 35µm stainless-steel mesh support using 2.5wt%, 5wt%, 7.5wt% of silica as the binding agent, recorded at 4800x (taken after the filtration of 10 ppm bentonite suspension).

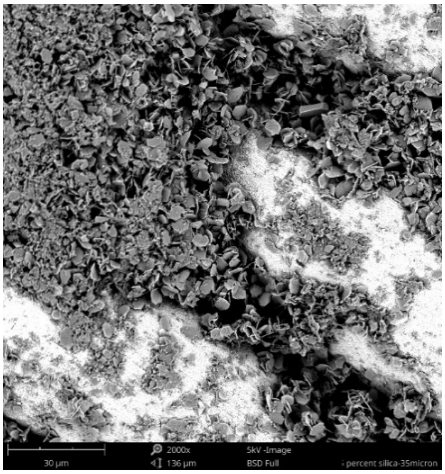

(2.5wt% silica)

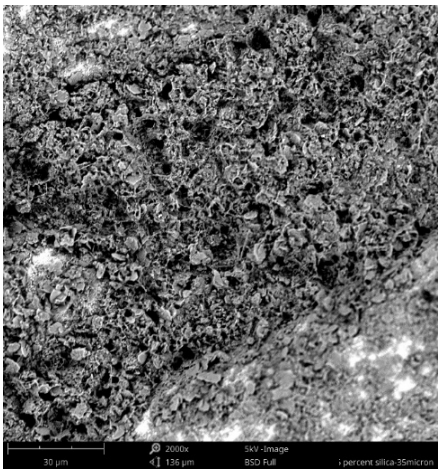

(5wt% silica)

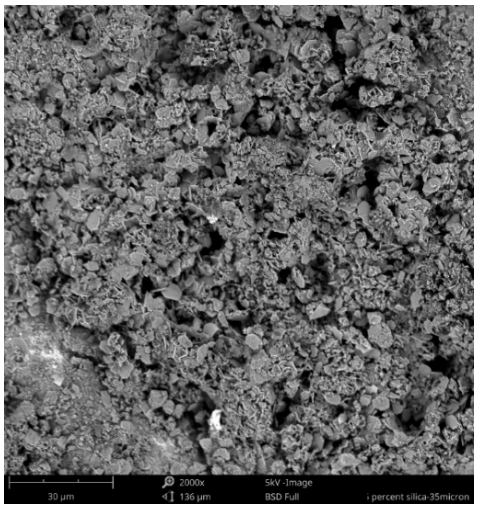

(7.5wt% silica)

Figure 6-2: TAN on 35µm stainless-steel mesh support using 2.5wt%, 5wt%, 7.5wt% of silica as the binding agent, recorded at 2000x (taken after the filtration of 10 ppm bentonite suspension).

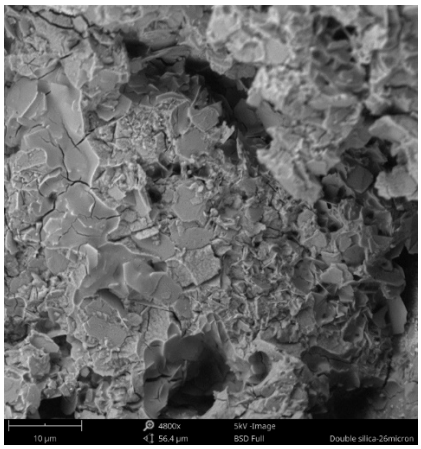

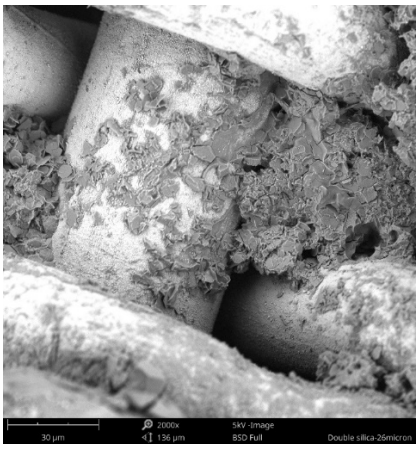

(4800x) (2000x)

Figure 6-3: Double coated membrane (first layer of 0.078g TAN, 10wt% silica and second layer of 0.0029g TAN and 5wt% silica) on 26µm stainless-steel mesh support, recorded at 4800x and 2000x (taken after the filtration of 10 ppm bentonite suspension).

6.2 TAN supported on SS mesh with use of silver as a binder

Figure 6-4 and Figure 6-5 compare TAN membranes deposited on a 35µm SS mesh support, using silver as the binding agent (0.025g and 0.05g). It can be observed that TAN particles were retained sparsely and tended to collapse onto the mesh and did not form an open porous structure. In addition, silver is more conductive than alumina or silica and will carry a greater charge in the SEM. Silver appears as very bright particles in the SEMs. In Figure 6-4 and Figure 6-5, the silver particles are not binding the TAN platelets together nor are they binding the TAN to the stainless steel mesh.

Figure 6-6 shows the membrane of TAN with double Ag_2O coatings (first layer was with 0.1g TAN and 0.0267g Ag_2O; second layer was with 0.1g Ag_2O only) on 35µm SS mesh. Obviously,

the TAN structure was reinforced, but there is still a large amount of colloidal silver appearing apart from the TAN. The SEM images demonstrate that colloidal silver is not a suitable binder in this application.

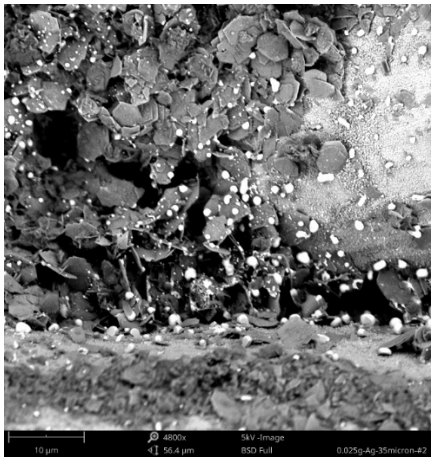

(0.025g Ag_2O)

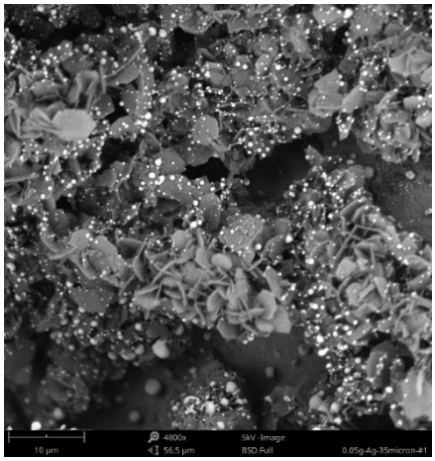

(0.05g Ag_2O)

Figure 6-4: TAN on 35µm stainless-steel mesh using silver (0.025g, 0.05g) as binding agent, recorded at 4800x (taken after the filtration of 10 ppm bentonite suspension).

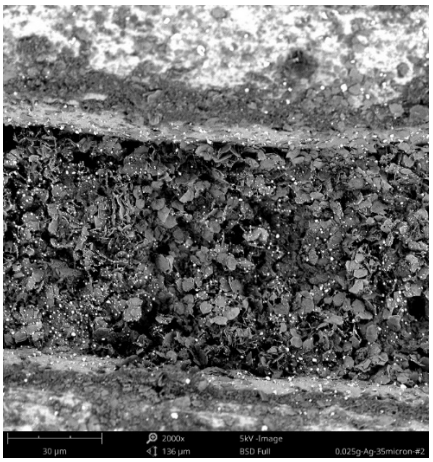

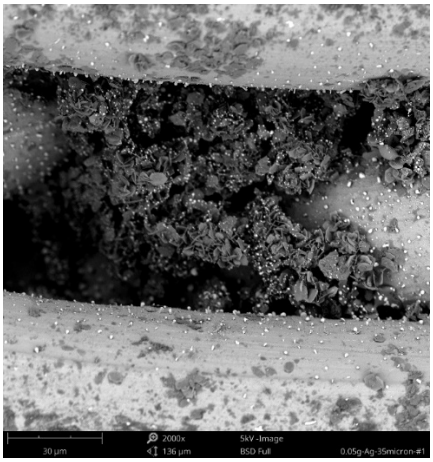

(0.025g Ag_2O) (0.05g Ag_2O)

Figure 6-5: TAN on 35µm stainless-steel mesh using silver (0.025g, 0.05g) as binding agent, recorded at 2000x (taken after the filtration of 10 ppm bentonite suspension).

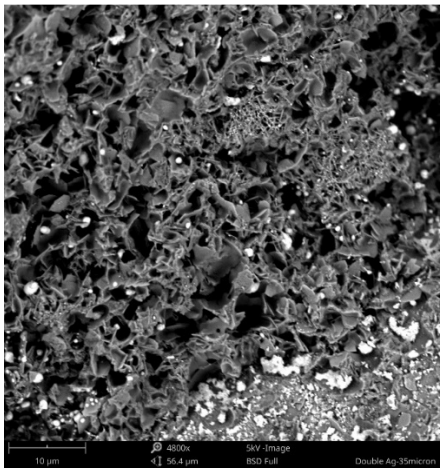

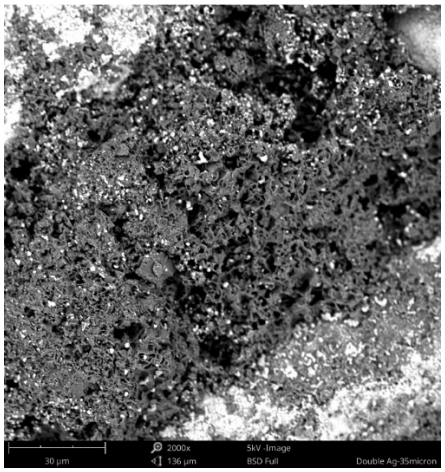

(4800x) (2000x)

Figure 6-6: Membrane of TAN with double Ag_2O coatings (first layer was with 0.1g TAN and 0.0267g Ag_2O; second layer was with 0.1g Ag_2O only) on 35µm SS mesh, recorded at 4800x and 2000x (taken after the filtration of 10 ppm bentonite suspension).

6.3 TAN on ceramic support with use of silica as a binder

Figure 6-7 compares TAN on a ceramic support using silica as the binding agent (5wt% and 10wt%). Both retained a selective layer with slit pore configuration after permeability tests. The membrane produced with 0.013g TAN and 5wt% silica binder has a more open structure than the membrane produced using 0.05g TAN and 10wt% silica binder solution, since the selective layer of the 10wt% membrane is filled with silica and the structured 2D/3D packing of the TAN is lost. This results in better flux for the 5wt% vs the 10wt% membrane as seen in Figure 5-21 (5wt%) vs Figure 5-23 (10wt%).

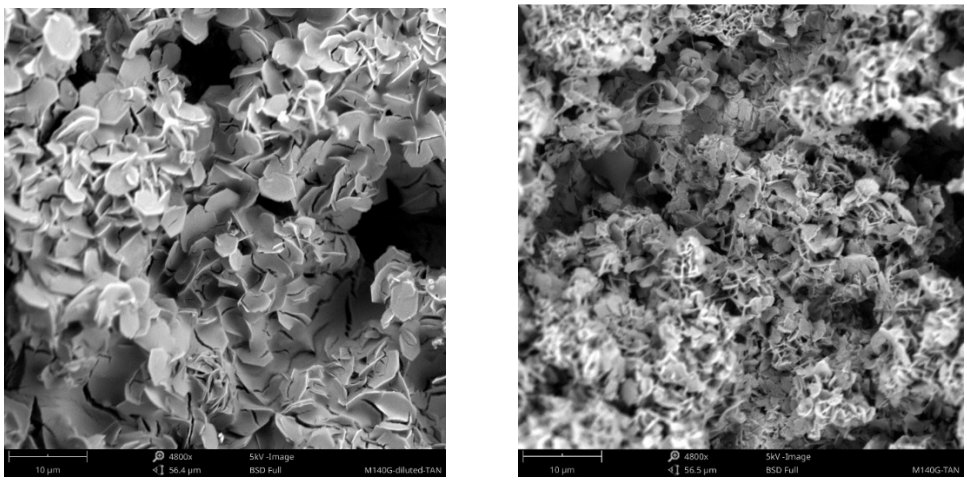

(5wt% silica) (10wt% silica)

Figure 6-7: TAN on ceramic support using silica as the binding agent (0.013g TAN and 5wt% silica, 0.05g TAN and 10wt% silica) recorded at 4800x (taken after the filtration of 10 ppm bentonite suspension).

7 Discussion Summary, Conclusions and Recommendations

7.1 Discussion Summary

The effect of seed mixing temperature on the structure and yield of twinned alumina nanosheets, was studied with the aim to obtain a maximum production of TAN. Experiments were carried out with varying seed mixing temperatures from 19.1 to 27 °C (Figure 3-1) followed by autoclaving and calcination to produce TAN. The effect of temperature on the shape and structure of boehmite nanosheets during seed mixing was assessed by SEM.

The yield of TAN varies slightly at temperatures between 19°C and 23.5°C. At 19°C, 0.42g of TAN were produced after calcination. At 22.5°C, the production of TAN goes up to 0.68g and the yield drops rapidly when it reaches 25°C.

When the seed mixing temperature is between 19°C and 21.7°C, most of the particles tend to form hexagons and are twinned to obtain a 2D/3D structure (Figure 3-1). The size of the nanosheets starts to decrease as a function of the seed mixing temperature when the temperature is above 21.7°C (Figure 3-2). Particles are also likely to aggregate and form larger clusters at higher temperatures, which is not desirable as larger clusters of TAN would lead to an uneven distribution of TAN particles on the stainless-steel mesh support during the deposition process. Thus, TAN synthesized with a seed mixing temperature from 19°C to 22°C have a better structure. Based on the results observed above, 20 °C was determined as the optimal seed mixing temperature, where most the particles are twinned hexagons and the yield is relatively high.

Membranes were fabricated by the deposition of TAN on supports via filtration, followed by sintering. The small-particle-filtering stainless steel wire cloth and a commercial membrane

ceramic support were selected as the membrane supports for TAN in this work. Based on filtration observations, the 35µm- stainless-steel mesh was found to be the optimal support in this work.

Electrochemical etching was applied to form a micro/nanostructure on the wire surface of the stainless-steel mesh, which creates more surface area and facilitates TAN adherence. An electrolyte was prepared with 3.6wt% of HCl and 1.2wt% of HNO_3 mixed in a 1:1 volume ratio. A piece of mesh was immersed in the electrolyte and placed parallel to a conductive graphite plate under a constant electric potential of 5V. We determined 4 minutes to be the best time to etch the SS wire cloth to get a re-entrant surface without decreasing the mechanical strength of wire mesh.

The effect of sintering temperature (700, 800, 900 and 1000°C) on the binding performance of stainless steel and deposited TAN using a silica binder was studied. From Figure 4-6, at temperatures 900°C and 1000°C the wire surfaces were severely oxidized and were no longer smooth compared to 700 °C. A sintering temperature of 800 °C was selected to minimize the damage to the SS supports and maintain a reasonably high temperature to properly sinter silica between the TAN particles and onto the SS support.

Permeability experiments were carried out for membranes with TAN on stainless-steel mesh supports using silica as binding agent. The filters were backflushed at 15 min intervals under an applied pressure 100 mbar. As shown in Figure 5-1, Figure 5-7 and Figure 5-9, the initial flux after backflushing declines as well as each subsequent backflush over the 4-hour run, indicating that TAN was successfully bound on the SS support. Compared to 2.5wt% silica and 5wt% silica membranes (Figure 5-2, Figure 5-7), the initial permeate flux of the 7.5wt% silica membrane (Figure 5-9) was about half of the other two as the higher concentration of silica binding agent partially fills the pores of the TAN selective layer.

The retention of the three membranes are shown in Figure 5-2, Figure 5-8, Figure 5-10. According to Figure 5-6, since the bentonite particle size ranges from 200nm to 700nm, we could estimate that the effective pore size of the 2.5wt%, 5wt% and 7.5wt% silica membranes are approximately 0.53 μm (retention of 12%) , >0.7 μm , 0.62 μm (retention of 2%), respectively. The retention could only reach up to 20% for the bentonite suspension.

The modeling results and best fit of the membranes at different time stages are listed in Table 5-2, Table 5-3 and Table 5-4. Cake filtration was not observed in both the middle and final stages for the 2.5wt% silica membrane, this further demonstrates that the backflushing provided a very deep form of cleaning where the pores were totally open and intermediate pore blocking could occur. Cake filtration occurred for the other two membranes (5wt% and 7.5wt% silica), which shows that more bentonite particles are retained on the surface of the membrane during filtration as higher concentrations of silica binder filled in the pores of TAN structure. This is also evidenced from the SEM pictures in Figure 6-1 and Figure 6-2, where bentonite particles (particles measuring less than 0.7 microns) do not appear in the SEMs at the 2.5wt% silica level but do appear on the 5 and 7.5wt% silica membranes. The slit-pore morphology of the TAN was maintained after deposition onto the stainless-steel mesh as evidenced in Figure 6-1 and Figure 6-2.

The double coated membrane was deposited with 0.078g TAN and 10wt% silica, followed by a second coating with 0.0029g TAN and 5wt% silica. The retention of the double coated membrane increased (Figure 5-12) compared to the single coated membranes, indicating that the larger pores of the membrane were blocked by the second coating. The retention is around 15%, which corresponds to an effective pore size of 0.52 μm. The modeling results and best fits of double-coating membrane of TAN and silica binder on SS support is shown in Table 5-5. Pore constriction was observed at the beginning of the run followed by intermediate blocking at middle stage and

final stage. This indicates that bentonite particles were released from the pores with backflushing. In the SEM image (Figure 6-3), a high concentration of silica binder led to the loss of the 3D structure of the TAN at the surface of the membrane.

Permeability experiments for membranes of TAN on stainless-steel mesh support using silver (Ag_2O) as a binding agent were also carried out. The filters were deposited with 0.05g TAN and silver of different amounts (0.025g and 0.05g), each followed by 4 hours of calcination at 500°C. There was no retention of bentonite on the membranes as flux curves remained at same level (Figure 5-13, Figure 5-15) and the retention for both membranes (Figure 5-14, Figure 5-16) is quite low. The concentration of particles in the permeate was greater than in the feed indicating that particles were released from the membrane. From Figures 6-4 to 6-5 it was observed that silver formed small aggregates. These are the brighter particles in the SEM, they are brighter as more scattering is produced by conductive materials and they illuminate compared to the background material that is nonconductive. These aggregates did not bind the TAN to the stainless steel.

For the membrane with double silver coatings (first layer was with 0.1g TAN and 0.0267g Ag_2O; second layer was with 0.1g Ag_2O only), flux declines occurred between backflushing cycles indicating that some of the deposited layer was retained on the surface of the membrane (Figure 5-17). However, the retention is less than zero indicating that particles were released from the TAN layer. As shown in Figure 6-6, the colloidal silver formed small aggregates. Colloidal silver did not wet the TAN nanosheets and provide binding between sheets or binding to the support.

Permeability experiments for membranes of TAN on ceramic supports using silica as a binding agent were performed for comparison with a stainless-steel mesh support. TAN suspensions with

amounts of 0.013g and 0.05g were mixed with silica binder, then the mixtures were deposited on ceramic supports, followed by 4 hours of calcination at 1000°C.

The average retention of the membrane of 0.013g TAN (5wt% silica) on a ceramic support was approximately 60%, indicating an effective pore size of 0.38 μm, and it was 66% for the 0.05g TAN (10wt% silica) membrane, so the effective pore size of the second membrane was estimated as 0.37 μm. Cake filtration became the primary mode of filtration for the two membranes throughout the tests (Table 5-7, Table 5-8) indicating that most bentonite particles were retained on the surface of the membrane.

7.2 Conclusions

Twinned alumina nanosheets were successfully synthesized and their unique 2D/3D nanoplatelet structure was observed. The slit pore morphology of the alumina nanosheet aggregates was maintained after the deposition of TAN on the stainless steel and ceramic supports. Inorganic binders, including silica sol (SiO_2) and colloidal silver (Ag_2O) were studied as binding agents. A 35µm small-particle-filtering stainless steel mesh and a ceramic membrane support were tested as backing materials for TAN.

The yield of TAN varied slightly with respect to seed mixing temperatures between 19°C and 23.5°C. An optimal seed mixing temperature of 20 °C was determined, where most of the particles were produced as twinned hexagons at a relatively high yield.

Membranes were fabricated by the deposition of TAN on supports via filtration principles, followed by sintering. Electrochemical etching was applied to form a micro/nanostructure on a wire surface of stainless-steel mesh, which creates more surface area and facilitates TAN deposition. The best etching time was determined as 4 minutes, with the aim to achieve a re-entrant surface without cracking of the wires of stainless-steel mesh and avoid reducing its mechanical strength. A sintering temperature of 800 °C was selected to minimize the damage to the SS wire during sintering.

The filtration properties of the TAN membranes were evaluated through a constant-pressure (100 mbar) filtration of 10 ppm bentonite clay solution. For membranes with TAN on SS support with silica as the binding agent, TAN is bonded to the support and the retained bentonite was removed away after backflushing. The 2.5wt% silica membrane displayed a high flux even though the particle filtration was modelled by pore constriction and intermediate blocking, indicating that

backflushing provided the deep cleaning of the pores. According to the SEM images, the 2.5wt% silica membrane preserved the integral structure of TAN after permeability tests, while the pores tended to be filled with silica at higher silica concentrations. Although the effective pore size of 2.5wt% silica was estimated to be the smallest, which is approximately 0.53 μm, the overall retention was small. The 7.5wt% silica membrane has an initial permeate flux that is half of the other two, this is because the high concentration of binder filled the pores of the TAN selective layer. The SiO_2 binder had a positive effect in reinforcing the TAN particles. In addition, the application of two TAN/silica coatings was found to substantially increase retention.

Permeability experiments for membranes of TAN on stainless-steel mesh supports using silver as binding agent were also carried out. The filters were deposited with 0.05g TAN and silver of different amounts (0.025g and 0.05g), each followed by 4 hours of calcination at 500°C. There were no bentonite particles retained on the membranes as flux curves remain unchanged. For the membrane with double silver coatings, flux declines occurred, while SEM imaging illustrated that silver was not wetting the materials and could not join with TAN and stainless steel. Colloidal silver was not found to be a suitable binding material for TAN on stainless steel.

Permeability tests for membranes of TAN on a ceramic support using silica as a binding agent were performed for comparison with stainless-steel mesh supports. The retention could reach up to 70%, showing an effective pore size of 0.37 μm and 0.38 μm for the synthetic membranes.

We concluded that 2D/3D alumina nanoplatelets (TAN) can be bound onto stainless steel supports to produce a new composite membrane, which remains its structural integrity after backflushing. This confirms our expectations in the very beginning. 20 °C was determined as the optimal seed mixing temperature to produce TAN, where most the particles are twinned hexagons and the yield

is relatively high. Silica with concentrations lower than 7.5% was found to be a suitable agent to bind the TAN onto the stainless steel mesh while keeping an open porous structure. A sintering temperature of 800 °C was selected to minimize the damage to the SS wire during sintering. Bentonite was found to be easily released form the TAN selective layer.

The results of this work show that TAN is a very promising material to produce lightweight, selective inorganic membranes that resist fine particulate fouling. The produced membrane is lightweight and could be used in applications where an inorganic membrane is needed but weight constraints exist such as the onsite treatment of oil spills. In this thesis we explored the fabrication workflow for this novel membrane, and the experimental study of oil/water separation or water purification using this membrane will be conducted in future work.

7.3 Recommendations

Based on these results, the following recommendations are proposed for future work.

1. The synthesis of TAN should be further investigated to improve productivity. Alternatives to the surfactant (CTAB) and other raw materials can be considered.

2. Further explore double coating, in particular different amounts of TAN during membrane fabrication to block larger pores and improve the integrity and retention of the membrane.

3. Two inorganic binders (SiO_2 colloidal and Ag_2O nanoparticles) were selected to synthesize composite membranes of TAN on supports. Other binders can be studied to reinforce the structure of TAN and bond them to backflushable supports.

4. A method to integrate the new synthetic membrane in a filtration unit to decontaminate oily waters from an oil spill should be further explored.

8 References

[1] "Spill Containment Methods | response.restoration.noaa.gov." [Online]. Available: https://response.restoration.noaa.gov/oil-and-chemical-spills/oil-spills/spill-containment-methods.html. [Accessed: 03-Aug-2019].

[2] M. S. Government of Canada; Transport Canada; Safety and Security, "2. Marine acts and regulations," 07-Jan-2010. [Online]. Available: https://www.tc.gc.ca/eng/marinesafety/tp-tp14609-2-marine-acts-regulations-617.htm. [Accessed: 04-Aug-2019].

[3] "Membrane," *Wikipedia*. 09-Sep-2018.

[4] M. Lee, Z. Wu, and K. Li, "2 - Advances in ceramic membranes for water treatment," in *Advances in Membrane Technologies for Water Treatment*, A. Basile, A. Cassano, and N. K. Rastogi, Eds. Oxford: Woodhead Publishing, 2015, pp. 43–82.

[5] K. Li, *Ceramic Membranes for Separation and Reaction*. John Wiley & Sons, 2007.

[6] S. R. H. Abadi, M. R. Sebzari, M. Hemati, F. Rekabdar, and T. Mohammadi, "Ceramic membrane performance in microfiltration of oily wastewater," *Desalination*, vol. 265, no. 1, pp. 222–228, Jan. 2011.

[7] A. Kayvani Fard *et al.*, "Inorganic Membranes: Preparation and Application for Water Treatment and Desalination," *Materials (Basel)*, vol. 11, no. 1, Jan. 2018.

[8] P. Maarten Biesheuvel and H. Verweij, "Design of ceramic membrane supports: permeability, tensile strength and stress," *Journal of Membrane Science*, vol. 156, no. 1, pp. 141–152, Apr. 1999.

[9] P. Monash, G. Pugazhenthi, and P. Saravanan, "Various fabrication methods of porous ceramic supports for membrane applications," *Reviews in Chemical Engineering*, vol. 29, no. 5, pp. 357–383, 2013.

[10] Z. Chen *et al.*, "ZrO2-coated stainless steel mesh with underwater superoleophobicity by electrophoretic deposition for durable oil/water separation," *J Sol-Gel Sci Technol*, vol. 85, no. 1, pp. 23–30, Jan. 2018.

[11] K. Hou *et al.*, "Durable underwater superoleophobic PDDA/halloysite nanotubes decorated stainless steel mesh for efficient oil–water separation," *Applied Surface Science*, vol. 416, pp. 344–352, Sep. 2017.

[12] Y. Liu, K. Zhang, W. Yao, J. Liu, Z. Han, and L. Ren, “Bioinspired structured superhydrophobic and superoleophilic stainless steel mesh for efficient oil-water separation,” *Colloids and Surfaces A: Physicochemical and Engineering Aspects*, vol. 500, pp. 54–63, Jul. 2016.

[13] Y. Yu, H. Chen, Y. Liu, V. Craig, L. H. Li, and Y. Chen, “Superhydrophobic and Superoleophilic Boron Nitride Nanotube-Coated Stainless Steel Meshes for Oil and Water Separation,” *Advanced Materials Interfaces*, vol. 1, no. 1, p. 1300002, Feb. 2014.

[14] K. Roebuck and A. Y. Tremblay, “Highly permeable twinned alumina nanoparticles for the precoat filtration of fine colloids,” *Separation and Purification Technology*, vol. 182, pp. 197–206, Jul. 2017.

[15] A. L. Zydney, “Chapter 15 - High Performance Ultrafiltration Membranes: Pore Geometry and Charge Effects,” in *Membrane Science and Technology*, vol. 14, S. T. Oyama and S. M. Stagg-Williams, Eds. Elsevier, 2011, pp. 333–352.

[16] K. Roebuck and A. Y. Tremblay, “The self-assembly of twinned boehmite nanosheets into porous 3D structures in ethanol–water mixtures,” *Colloids and Surfaces A: Physicochemical and Engineering Aspects*, vol. 495, no. Complete, pp. 238–247, 2016.

[17] X. Meng, “Flow Through, 2D/3D Nanoplatelet Supports for Packed Beds and Columns,” Thesis, Université d’Ottawa / University of Ottawa, 2018.

[18] C. M. Reddy *et al.*, “The West Falmouth Oil Spill after Thirty Years: The Persistence of Petroleum Hydrocarbons in Marsh Sediments,” *Environ. Sci. Technol.*, vol. 36, no. 22, pp. 4754–4760, Nov. 2002.

[19] R. T. Carson, R. C. Mitchell, R. J. Kopp, S. Presser, and P. A. Ruud, “Contingent Valuation and Lost Passive Use: Damages from the Exxon Valdez Oil Spill,” p. 30.

[20] T. M. Brody, P. D. Bianca, and J. Krysa, “Analysis of Inland Crude Oil Spill Threats, Vulnerabilities, and Emergency Response in the Midwest United States,” *Risk Analysis*, vol. 32, no. 10, pp. 1741–1749, 2012.

[21] O. US EPA, “EPA’s Response Techniques,” *US EPA*, 14-Mar-2013. [Online]. Available: https://www.epa.gov/emergency-response/epas-response-techniques. [Accessed: 03-Aug-2019].

[22] O. US EPA, “Booms,” *US EPA*, 30-Jul-2013. [Online]. Available: https://www.epa.gov/emergency-response/booms. [Accessed: 04-Aug-2019].

[23] C. on U. O. S. D. E. and Effects, O. S. Board, D. on E. and L. Studies, and N. R. Council, *Oil Spill Dispersants: Efficacy and Effects*. National Academies Press, 2005.

[24] B. Doshi, M. Sillanpää, and S. Kalliola, "A review of bio-based materials for oil spill treatment," *Water Research*, vol. 135, no. Complete, pp. 262–277, 2018.

[25] C. Falamaki and M. Beyhaghi, "Slip casting process for the manufacture of tubular alumina microfiltration membranes," *Materials Science Poland*, vol. Vol. 27, No. 2, 2009.

[26] P.-K. Lin and D.-S. Tsai, "Preparation and Analysis of a Silicon Carbide Composite Membrane," *Journal of the American Ceramic Society*, vol. 80, no. 2, pp. 365–372, 1997.

[27] J. M. Benito, A. Conesa, F. Rubio, and M. A. Rodríguez, "Preparation and characterization of tubular ceramic membranes for treatment of oil emulsions," *Journal of the European Ceramic Society*, vol. 25, no. 11, pp. 1895–1903, Jul. 2005.

[28] N. Das, S. Bandyopadhyay, D. Chattopadhyay, and H. S. Maiti, "Tape-cast ceramic membranes for microfiltration application," *JOURNAL OF MATERIALS SCIENCE*, vol. 31, no. 19, pp. 5221–5225, Jan. 1996.

[29] K. Lindqvist and E. Lidén, "Preparation of alumina membranes by tape casting and dip coating," *Journal of the European Ceramic Society*, vol. 17, no. 2, pp. 359–366, Jan. 1997.

[30] A. J. Burggraaf and L. Cot, *Fundamentals of Inorganic Membrane Science and Technology*. Elsevier, 1996.

[31] E. Drioli, L. Giorno, and E. Fontananova, *Comprehensive Membrane Science and Engineering*. Elsevier, 2017.

[32] J. Smid, C. G. Avci, V. Günay, R. A. Terpstra, and J. P. G. M. Van Eijk, "Preparation and characterization of microporous ceramic hollow fibre membranes," *Journal of Membrane Science*, vol. 112, no. 1, pp. 85–90, Apr. 1996.

[33] İ. Erdem, "Sol-gel applications for ceramic membrane preparation," *AIP Conference Proceedings*, vol. 1809, no. 1, p. 020011, Feb. 2017.

[34] "Filtration Membrane." [Online]. Available: https://courses.washington.edu/conj/bess/filtration/filtration.htm. [Accessed: 07-Mar-2019].

[35] H. Holthöfer, "Molecular architecture of the glomerular slit diaphragm: lessons learnt for a better understanding of disease pathogenesis," *Nephrol Dial Transplant*, vol. 22, no. 8, pp. 2124–2128, Aug. 2007.

[36] M. U. Siddiqui, A. F. M. Arif, and S. Bashmal, “Permeability-Selectivity Analysis of Microfiltration and Ultrafiltration Membranes: Effect of Pore Size and Shape Distribution and Membrane Stretching,” *Membranes (Basel)*, vol. 6, no. 3, Aug. 2016.

[37] D. M. Kanani, W. H. Fissell, S. Roy, A. Dubnisheva, A. Fleischman, and A. L. Zydney, “Permeability–selectivity analysis for ultrafiltration: Effect of pore geometry,” *Journal of Membrane Science*, vol. 349, no. 1, pp. 405–410, 2010.

[38] K. Roebuck and A. Y. Tremblay, “Optimal aggregate size distribution for the formation of highly efficient nanosheet dynamic membranes,” *Journal of Membrane Science*, vol. 514, no. Complete, pp. 143–154, 2016.

[39] M. Lipińska-Chwałek, L. Kiesel, and J. Malzbender, “Mechanical properties of porous MgO substrates for membrane applications,” *Journal of the European Ceramic Society*, vol. 34, no. 10, pp. 2519–2524, Sep. 2014.

[40] J. Zhang and J. Malzbender, “Mechanical characterization of micro- and nano-porous alumina,” *Ceramics International*, vol. 41, no. 9, Part A, pp. 10725–10729, Nov. 2015.

[41] Z. Yu, J. Ni, L. Fang, D. Wu, and H. Zhu, “Multilayer Three-Dimensional Structure Made of Modified Stainless Steel Mesh for in Situ Continuous Separation of Spilled Oil,” *Ind. Eng. Chem. Res.*, vol. 54, no. 47, pp. 11838–11843, Dec. 2015.

[42] A. Kim, C. Lee, and J. Kim, “Durable, scalable, and tunable omniphobicity on stainless steel mesh for separation of low surface tension liquid mixtures,” *Surface and Coatings Technology*, vol. 344, pp. 394–401, Jun. 2018.

[43] P. Varshney, D. Nanda, M. Satapathy, S. S. Mohapatra, and A. Kumar, “A facile modification of steel mesh for oil–water separation,” *New J. Chem.*, vol. 41, no. 15, pp. 7463–7471, Jul. 2017.

[44] D. Nanda, A. Sahoo, A. Kumar, and B. Bhushan, “Facile approach to develop durable and reusable superhydrophobic/superoleophilic coatings for steel mesh surfaces,” *Journal of Colloid and Interface Science*, vol. 535, pp. 50–57, Feb. 2019.

[45] M. Alonso Frank, A. R. Boccaccini, and S. Virtanen, “A facile and scalable method to produce superhydrophic stainless steel surface,” *Applied Surface Science*, vol. 311, pp. 753–757, Aug. 2014.

[46] W. T. Choi, K. Oh, P. M. Singh, V. Breedveld, and D. W. Hess, “Wettability control of stainless steel surfaces via evolution of intrinsic grain structures,” *J Mater Sci*, vol. 51, no. 11, pp. 5196–5206, Jun. 2016.

[47] M. Stöver *et al.*, “Microstructuring of stainless steel implants by electrochemical etching,” *J Mater Sci*, vol. 41, no. 17, pp. 5569–5575, Sep. 2006.

[48] S. Bose and C. Das, “Role of Binder and Preparation Pressure in Tubular Ceramic Membrane Processing: Design and Optimization Study Using Response Surface Methodology (RSM),” *Ind. Eng. Chem. Res.*, vol. 53, no. 31, pp. 12319–12329, Aug. 2014.

[49] A. L. Ahmad, M. A. T. Jaya, and D. C. J. Chieh, “The Effects of Organic Binders on Palladium Impregnated in TiO2 Membrane Synthesis: X-Ray Diffraction Analysis,” *Journal of the American Ceramic Society*, vol. 93, no. 11, pp. 3595–3599, 2010.

[50] H. Abdallah, Sh. K. Amin, H. H. Abo–Almaged, and M. F. Abadir, “Fabrication of ceramic membranes from nano–rosette structure high alumina roller kiln waste powder for desalination application,” *Ceramics International*, vol. 44, no. 7, pp. 8612–8622, May 2018.

[51] M. Arzani, H. R. Mahdavi, M. Sheikhi, T. Mohammadi, and O. Bakhtiari, “Ceramic monolith as microfiltration membrane: Preparation, characterization and performance evaluation,” *Applied Clay Science*, vol. 161, pp. 456–463, Sep. 2018.

[52] F. Lian, Y. Wen, Y. Ren, and H. Guan, “A novel PVB based polymer membrane and its application in gel polymer electrolytes for lithium-ion batteries,” *Journal of Membrane Science*, vol. 456, pp. 42–48, Apr. 2014.

[53] S. Sarkar, “Process for Preparation of Low Cost Clay-Alumina Multichannel Ceramic Membrane for Liquid Filtration Application,” *Transactions of the Indian Ceramic Society*, vol. 73, no. 3, pp. 239–244, Jul. 2014.

[54] X. Zhou and C. He, “Tailoring the surface chemistry and morphology of glass fiber membranes for robust oil/water separation using poly(dimethylsiloxanes) as hydrophobic molecular binders,” *J. Mater. Chem. A*, vol. 6, no. 2, pp. 607–615, Jan. 2018.

[55] M. A. Janney, “Plastic forming of ceramics: extrusion and injection moulding,” in *Ceramic Processing*, R. A. Terpstra, P. P. A. C. Pex, and A. H. de Vries, Eds. Dordrecht: Springer Netherlands, 1995, pp. 174–211.

[56] S. Kwon and G. L. Messing, “Constrained densification in boehmite–alumina mixtures for the fabrication of porous alumina ceramics,” *Journal of Materials Science*, vol. 33, no. 4, pp. 913–921, Feb. 1998.

[57] J. A. Fernando and D. D. L. Chung, “Improving an alumina fiber filter membrane for hot gas filtration using an acid phosphate binder,” *Journal of Materials Science*, vol. 36, no. 21, pp. 5079–5085, Nov. 2001.

[58] M. Ray, P. Bhattacharya, R. Das, K. Sondhi, S. Ghosh, and S. Sarkar, “Preparation and characterization of macroporous pure alumina capillary membrane using boehmite as binder for filtration application,” *J Porous Mater*, vol. 22, no. 4, pp. 1043–1052, Aug. 2015.

[59] G. Liu, J. Guo, F. Meng, X. Zhang, and L. Wang, “Effects of Colloidal Silica Binder on Catalytic Activity and Adhesion of HZSM-5 Coatings for Structured Reactors,” *Chinese Journal of Chemical Engineering*, vol. 22, no. 8, pp. 875–881, Aug. 2014.

[60] A. V. Boix, J. M. Zamaro, E. A. Lombardo, and E. E. Miró, “The beneficial effect of silica on the activity and thermal stability of PtCoFerrierite-washcoated cordierite monoliths for the SCR of NOx with CH4,” *Applied Catalysis B: Environmental*, vol. 46, no. 1, pp. 121–132, Oct. 2003.

[61] R. Yu, P. Spiesz, and H. J. H. Brouwers, “Effect of nano-silica on the hydration and microstructure development of Ultra-High Performance Concrete (UHPC) with a low binder amount,” *Construction and Building Materials*, vol. 65, pp. 140–150, Aug. 2014.

[62] Y. Dong, C.-A. Wang, J. Zhou, and Z. Hong, “A novel way to fabricate highly porous fibrous YSZ ceramics with improved thermal and mechanical properties,” *Journal of the European Ceramic Society*, vol. 32, no. 10, pp. 2213–2218, Aug. 2012.

[63] J. Sun, Z. Hu, J. Li, H. Zhang, and C. Sun, “Thermal and mechanical properties of fibrous zirconia ceramics with ultra-high porosity,” *Ceramics International*, vol. 40, no. 8, Part A, pp. 11787–11793, Sep. 2014.

[64] H. Ghahremani 1, A. Moradi2, J. Abedini-Torghabeh3, and S. M. Hassani4, “Measuring surface tension of binary mixtures of water + alcohols from the diffraction pattern of surface ripples,” *Der Chemica Sinica*, vol. 2, no. 6, 2011.

[65] H. Peng and A. Y. Tremblay, “Membrane regeneration and filtration modeling in treating oily wastewaters,” *Journal of Membrane Science*, vol. 324, no. 1–2, pp. 59–66, 2008.

Appendix A

Modeling results for the membranes produced in this work.

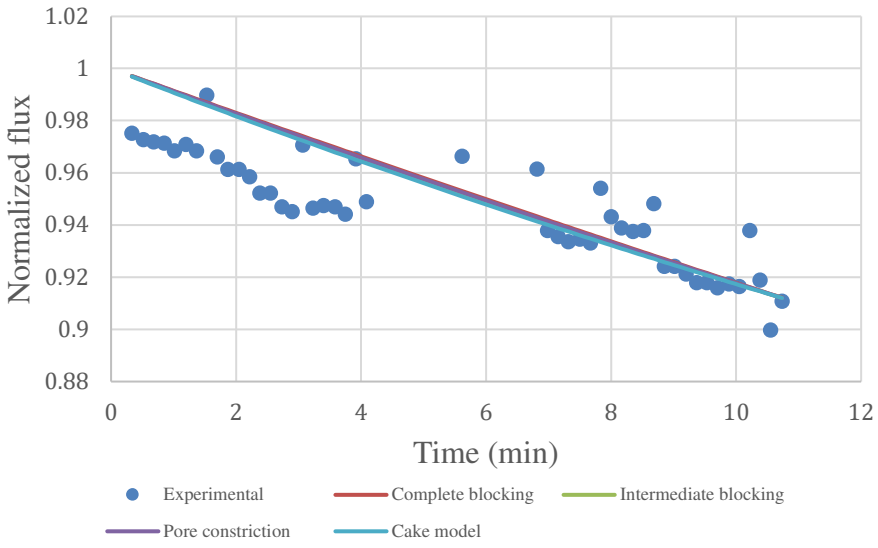

Figure A- 1: Experimental flux data at initial stage (13.27 min -27.4 min) and models fitted to the data for membrane with 5wt% silica.

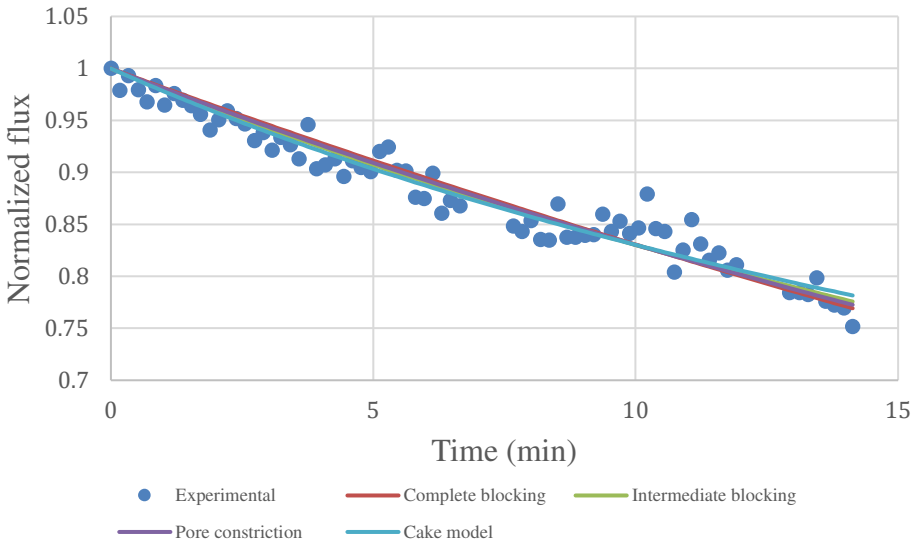

Figure A- 2: Experimental flux data at initial stage (13.27 min -27.4 min) and models fitted to the data for membrane with 5wt% silica.

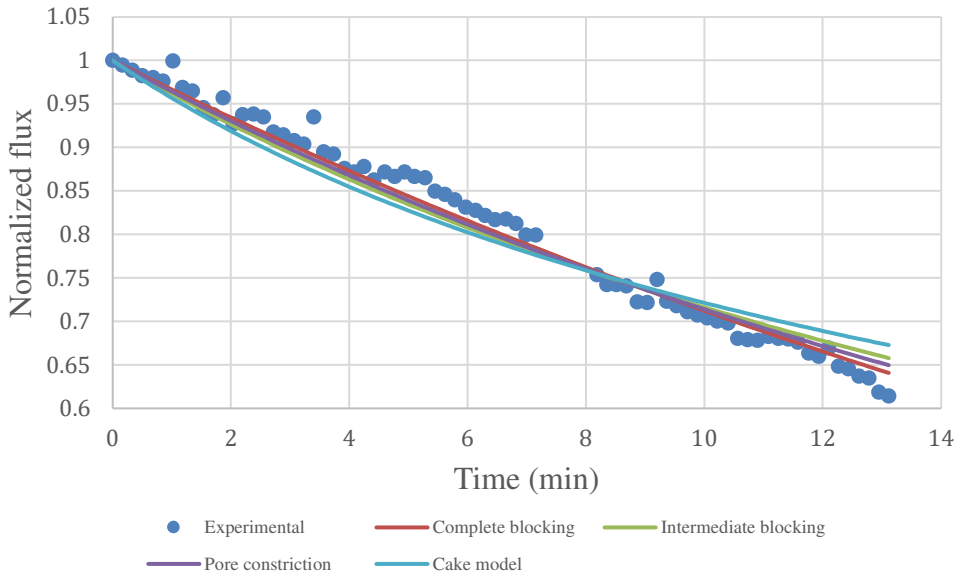

Figure A- 3: Experimental flux data at final stage (203.73 min-216.85 min) and models fitted to the data for membrane with 5wt% silica.

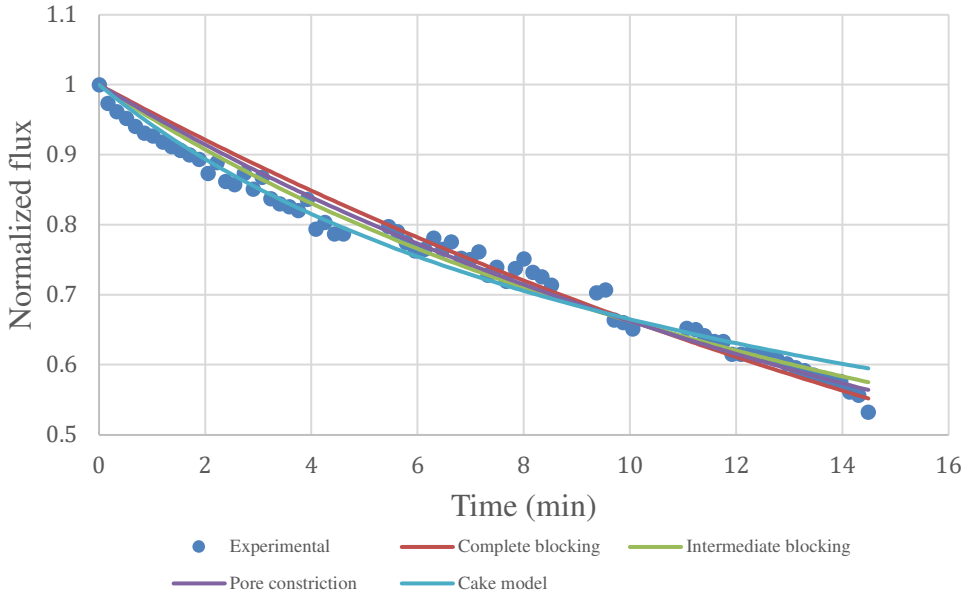

Figure A- 4: Experimental flux data at initial stage (11.23 min -25.72 min) and models fitted to the data for membrane with 7.5wt% silica.

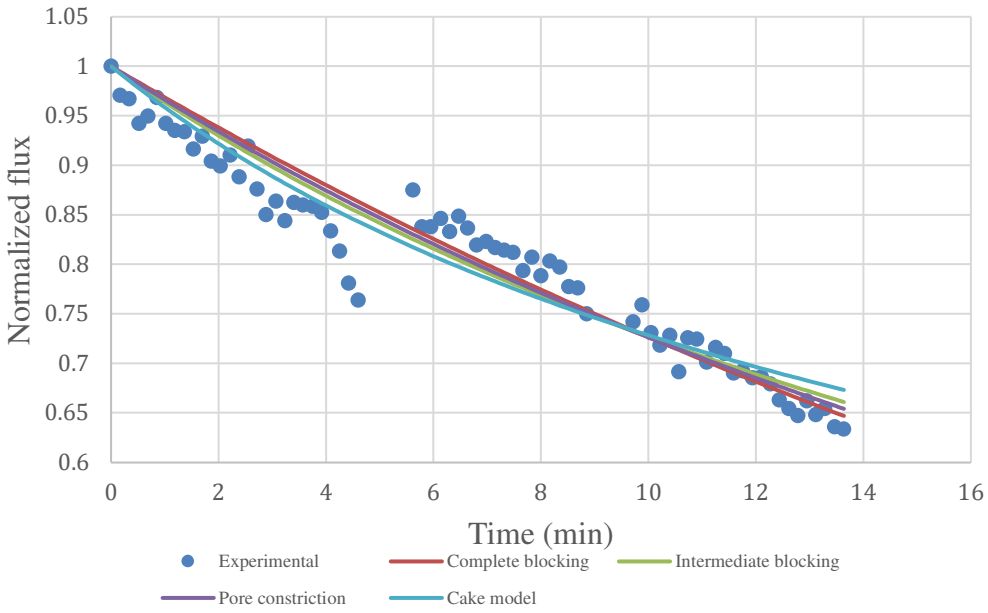

Figure A- 5: Experimental flux data at middle stage (98.28 min-111.92 min) and models fitted to the data for membrane with 7.5wt% silica.

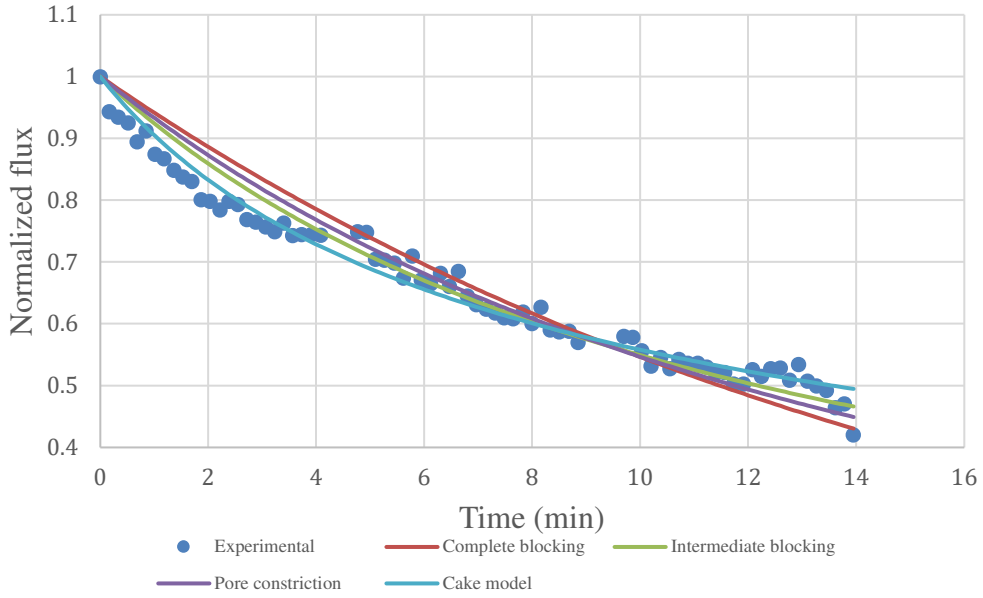

Figure A- 6: Experimental flux data at final stage (202.18 min-216.13 min) and models fitted to the data for membrane with 7.5wt% silica.

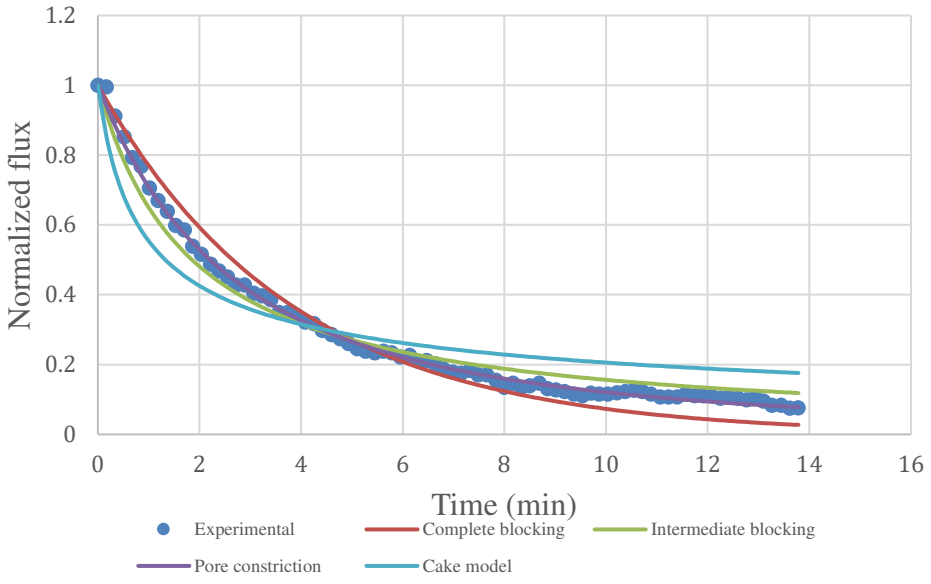

Figure A- 7: Experimental flux data at initial stage (0-13.78 min) and models fitted to the data for the double coated membrane (first layer of 0.078g TAN, 10wt% silica and second layer of 0.0029g TAN and 5wt% silica) on 26µm stainless-steel mesh support.

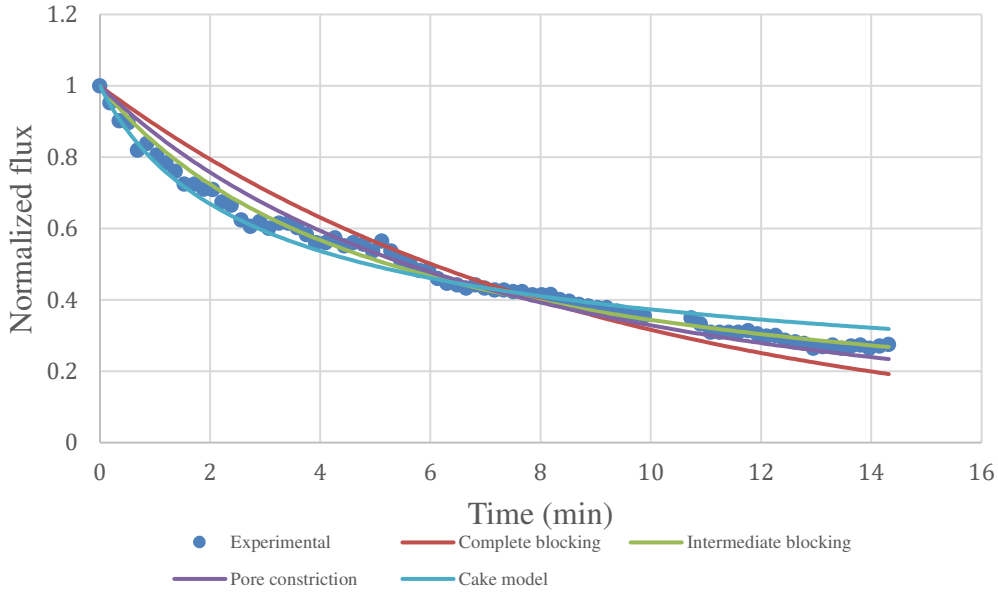

Figure A- 8: Experimental flux data at middle stage (81.28 min-95.58 min) and models fitted to the data for the double coated membrane (first layer of 0.078g TAN, 10wt% silica and second layer of 0.0029g TAN and 5wt% silica) on 26µm stainless-steel mesh support.

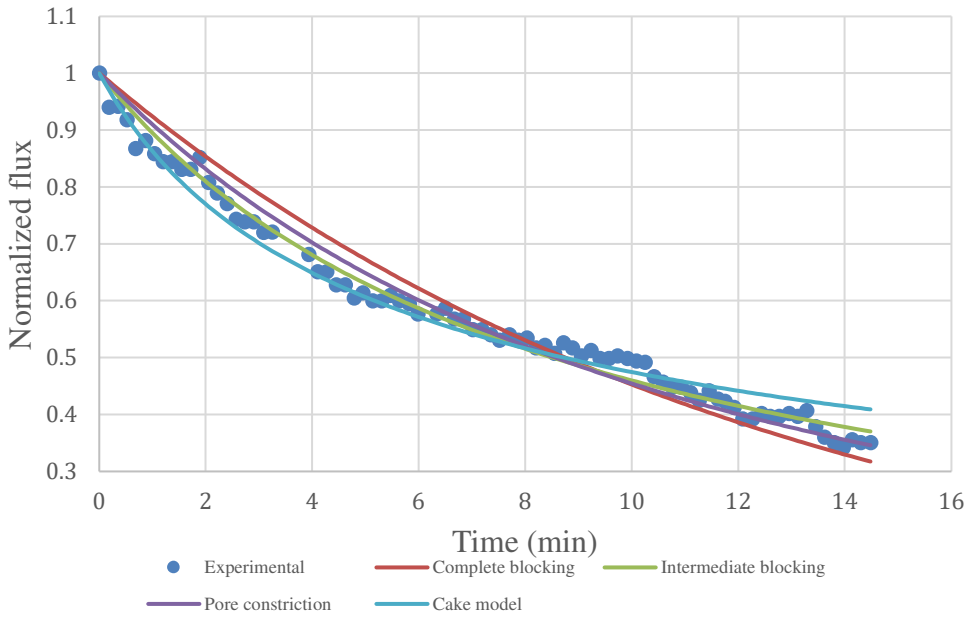

Figure A- 9: Experimental flux data at final stage (178.63 min-193.11 min) and models fitted to the data for the double coated membrane (first layer of 0.078g TAN, 10wt% silica and second layer of 0.0029g TAN and 5wt% silica) on 26µm stainless-steel mesh support.

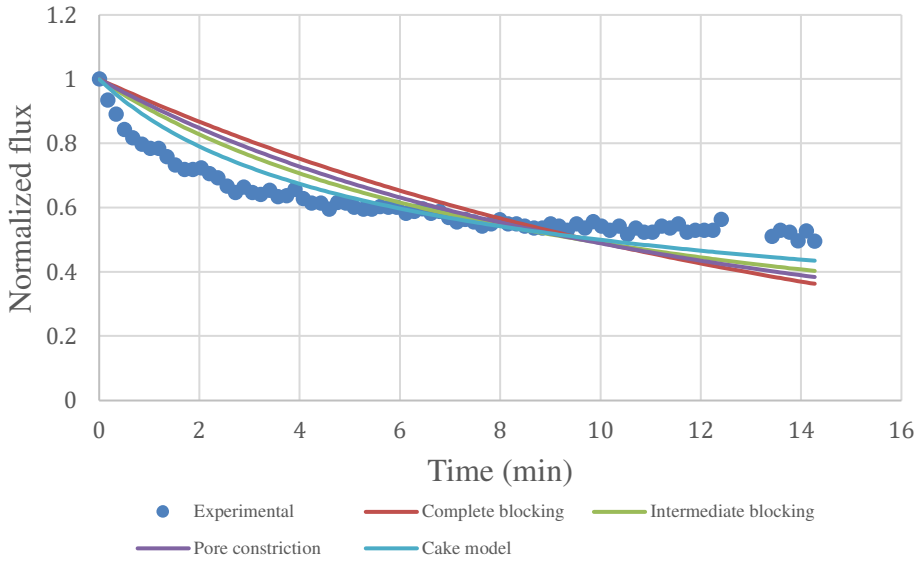

Figure A- 10: Experimental flux data at initial stage (10.88 min-25.15 min) and models fitted to the data for membrane with double silver coatings (first layer was with 0.1g TAN and 0.0267g Ag_2O; second layer was with 0.1g Ag_2O only).

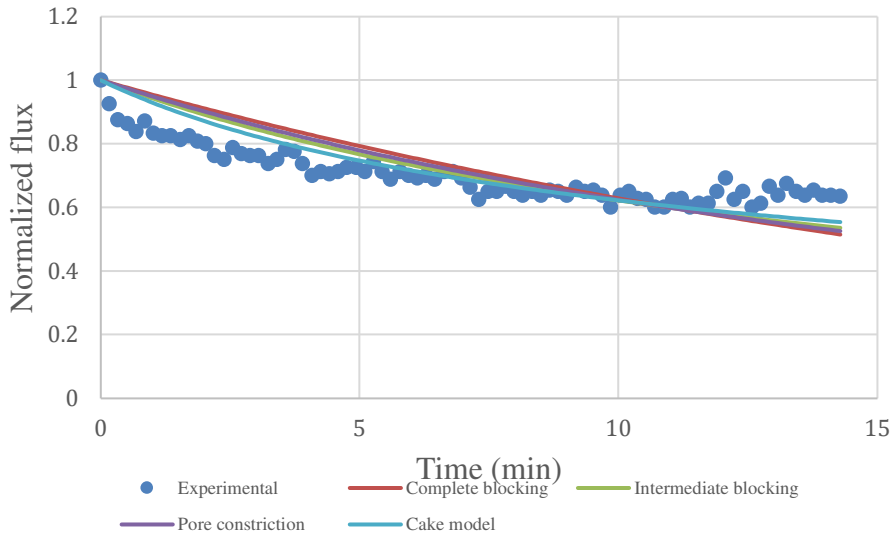

Figure A- 11: Experimental flux data at middle stage (97.43 min-111.72 min) and models fitted to the data for membrane with double silver coatings (first layer was with 0.1g TAN and 0.0267g Ag_2O; second layer was with 0.1g Ag_2O only).

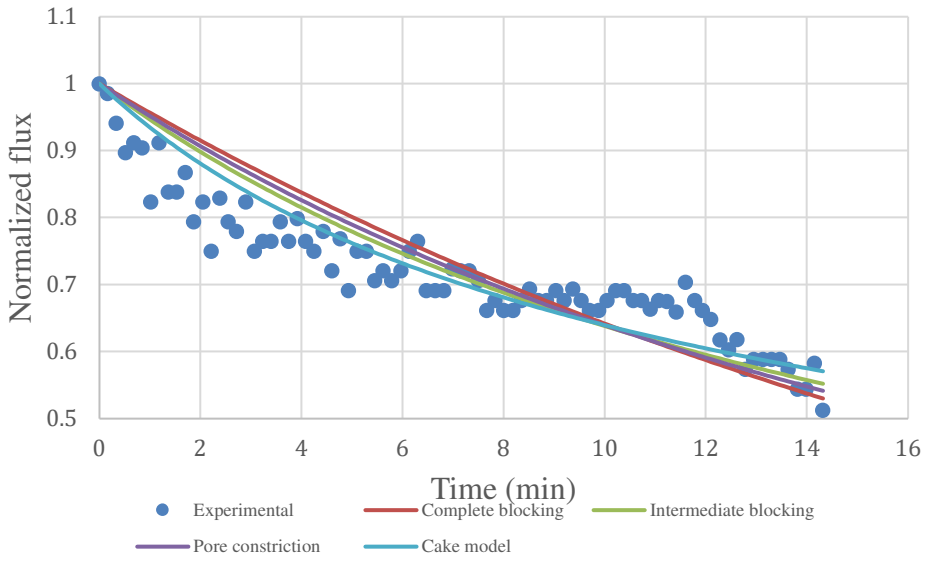

Figure A- 12: Experimental flux data at final stage (201.3 min-215.62 min) and models fitted to the data for membrane with double silver coatings (first layer was with 0.1g TAN and 0.0267g Ag_2O; second layer was with 0.1g Ag_2O only).

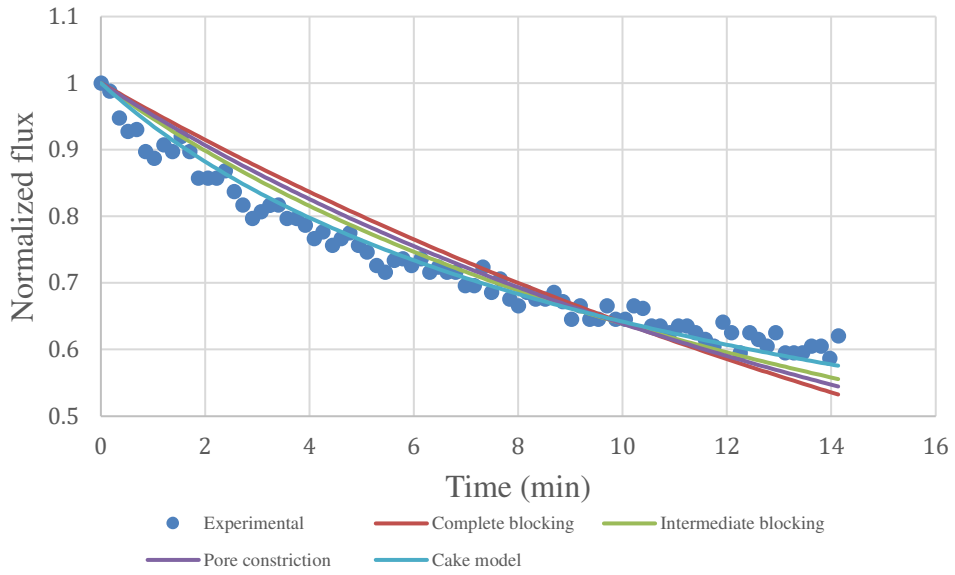

Figure A- 13: Experimental flux data at initial stage (10.72 min-24.85 min) and models fitted to the data for 0.013g TAN on 1.4 µm ceramic support using 5wt% silica as the binding agent.

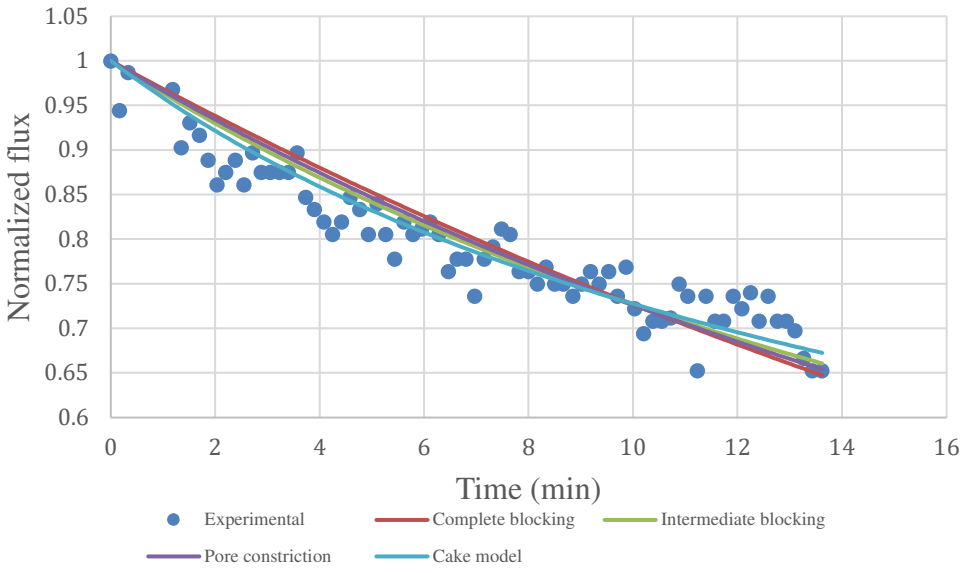

Figure A- 14: Experimental flux data at middle stage (108.33 min-121.95 min) and models fitted to the data for 0.013g TAN on 1.4 µm ceramic support using 5wt% silica as the binding agent.

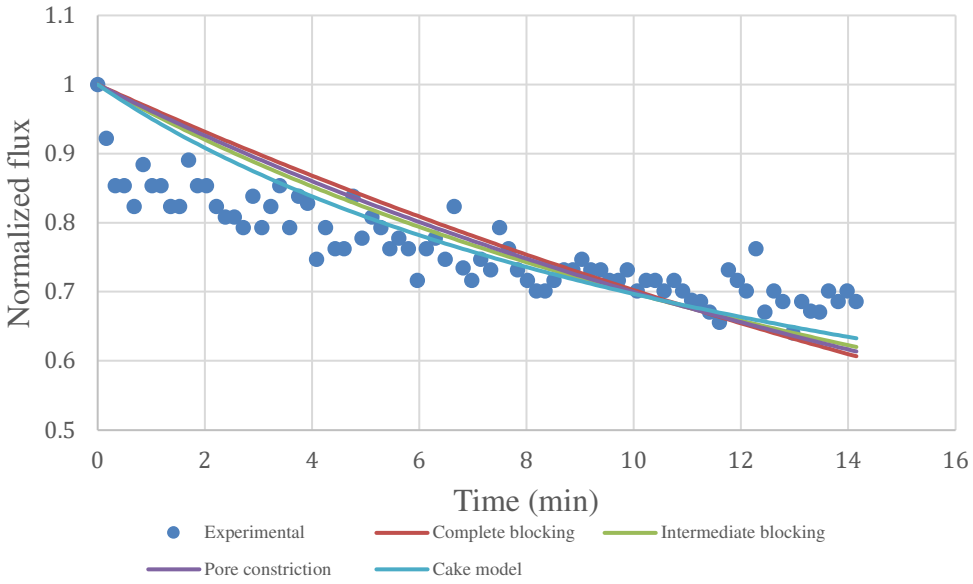

Figure A- 15: Experimental flux data at final stage (205.75 min-219.9 min) and models fitted to the data for 0.013g TAN on 1.4 µm ceramic support using 5wt% silica as the binding agent.

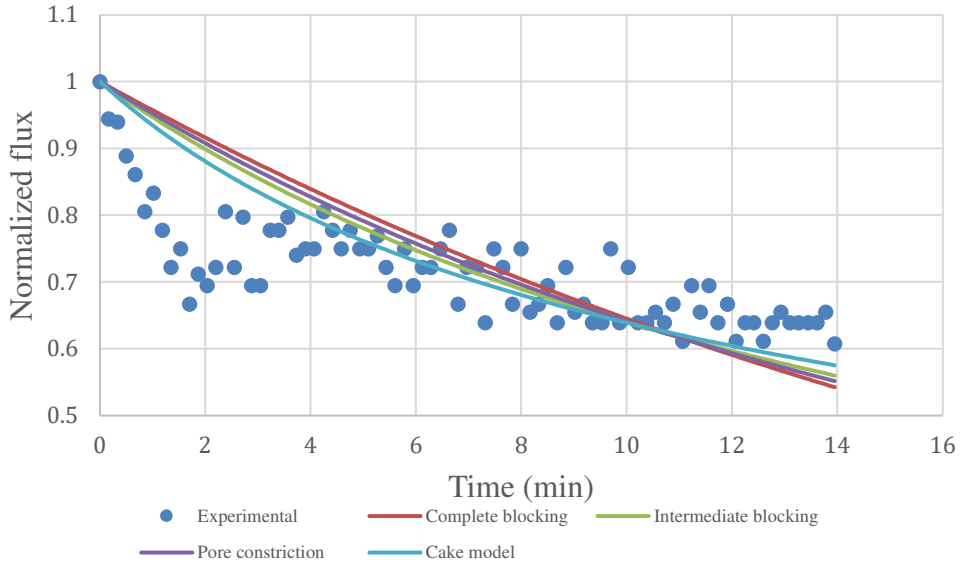

Figure A- 16: Experimental flux data at initial stage (5.22 min-19.17 min) and models fitted to the data for 0.05g TAN on 1.4 µm ceramic support using 10wt% silica as the binding agent.

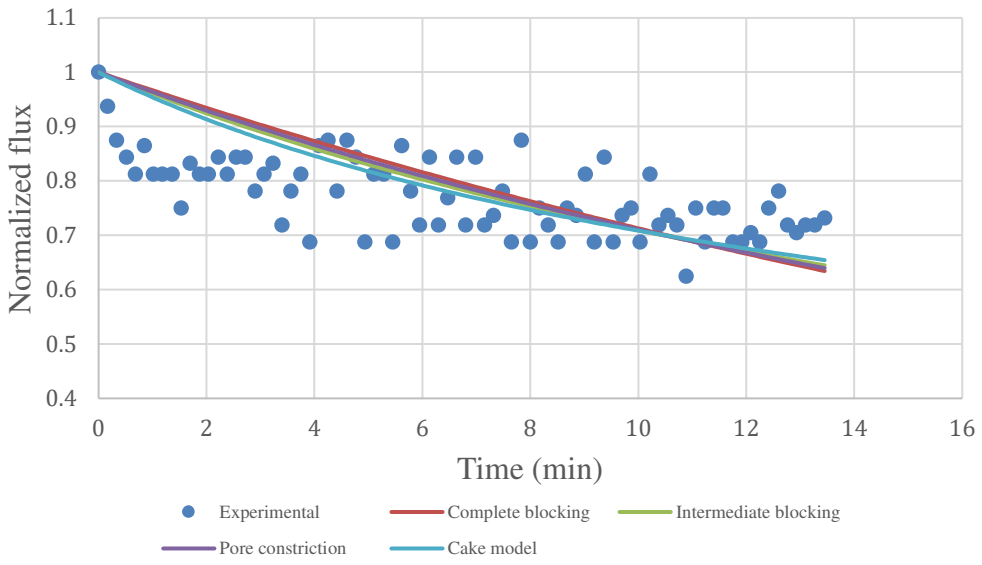

Figure A- 17: Experimental flux data at middle stage (22.07 min-35.52 min) and models fitted to the data for 0.05g TAN on 1.4 µm ceramic support using 10wt% silica as the binding agent.

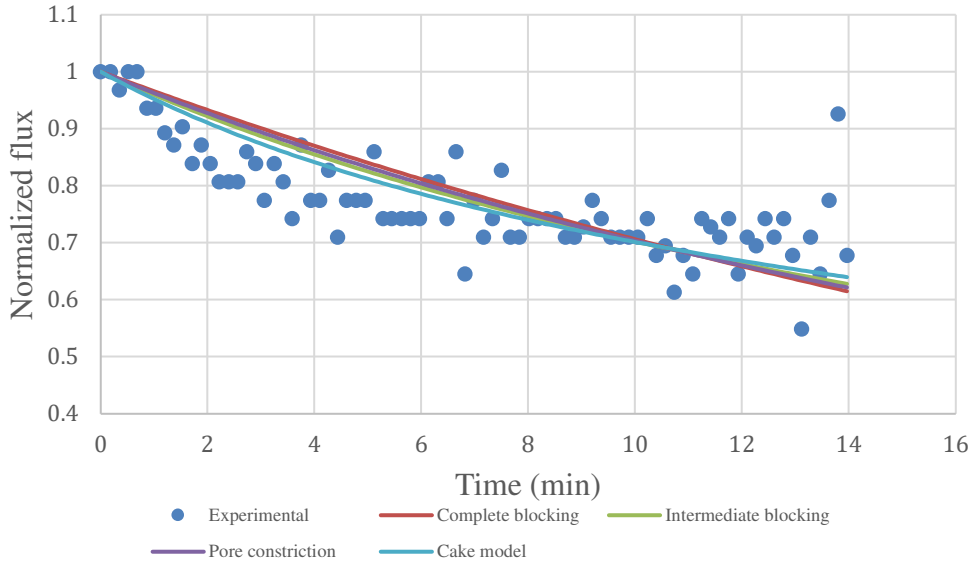

Figure A- 18: Experimental flux data at final stage (37.72 min-51.69 min) and models fitted to the data for 0.05g TAN on 1.4 µm ceramic support using 10wt% silica as the binding agent.

Appendix B

SEM images of the synthetic membranes at various magnifications.

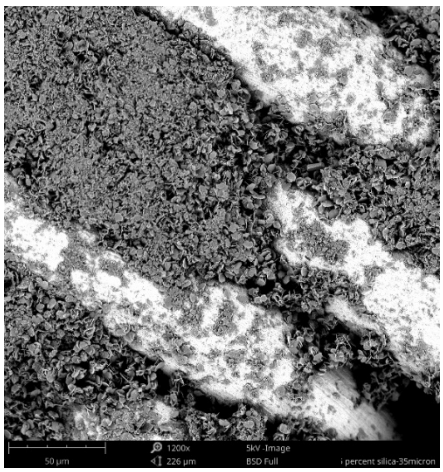

(a)

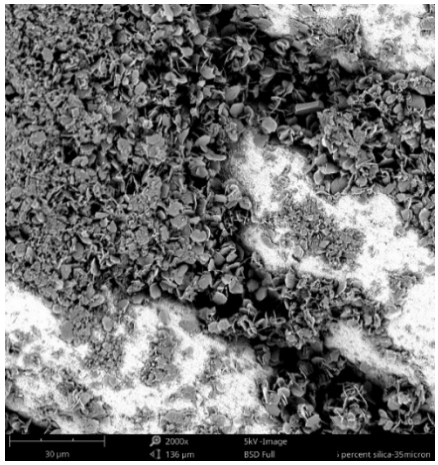

(b)

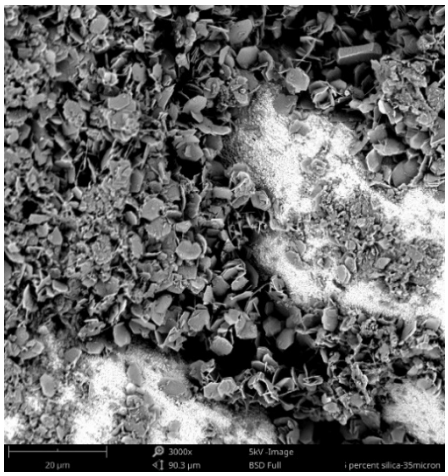

(c)

(d)

Figure B- 1: SEM images showing TAN supported on SS mesh with a silica concentration of 2.5wt%, recorded at different magnifications (a) 1200x (b) 2000x (c) 3000x (d) 4800x (taken after the filtration of 10 ppm bentonite suspension).

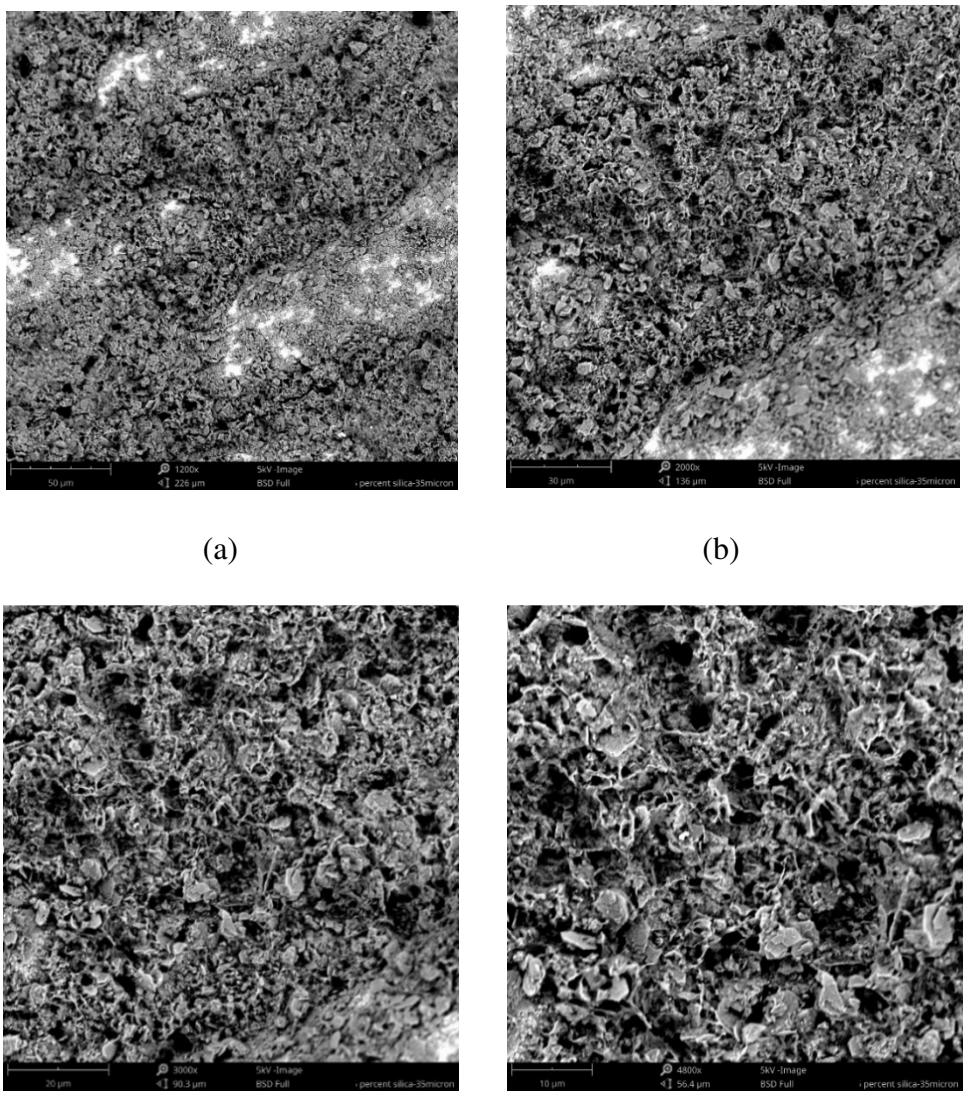

(a) (b)

(c) (d)

Figure B- 2: SEM images showing TAN supported on SS mesh with a silica concentration of 5wt%. recorded at different magnifications (a) 1200x (b) 2000x (c) 3000x (d) 4800x (taken after the filtration of 10 ppm bentonite suspension).

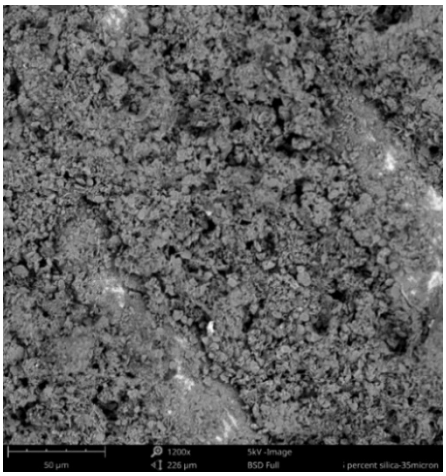

(a)

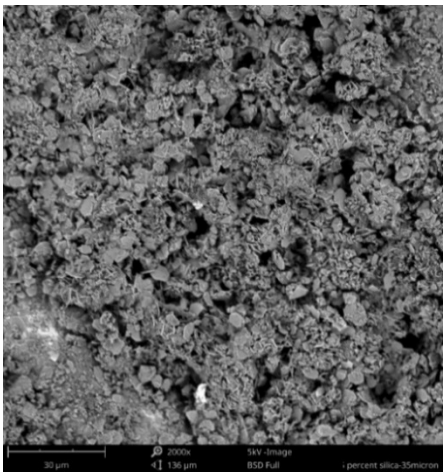

(b)

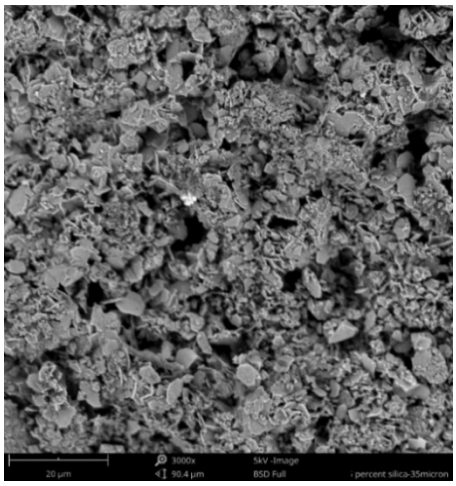

(c)

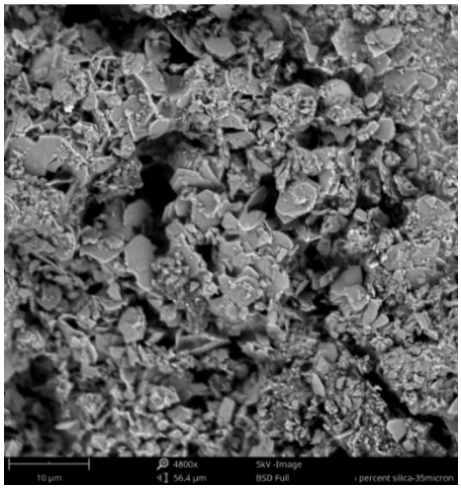

(d)

Figure B- 3: SEM images showing TAN supported on SS mesh with a silica concentration of 7.5wt%, recorded at different magnifications (a) 1200x (b) 2000x (c) 3000x (d) 4800x (taken after the filtration of 10 ppm bentonite suspension).

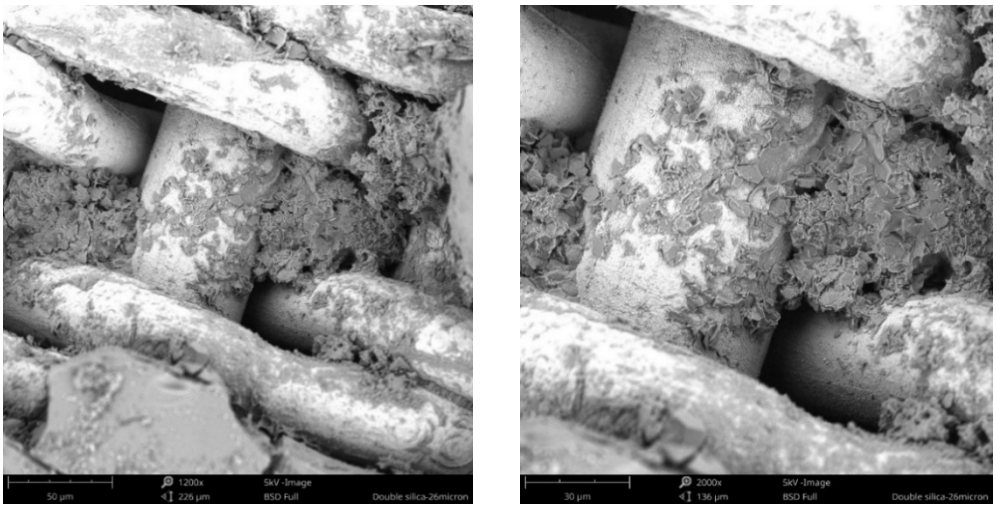

(a) (b)

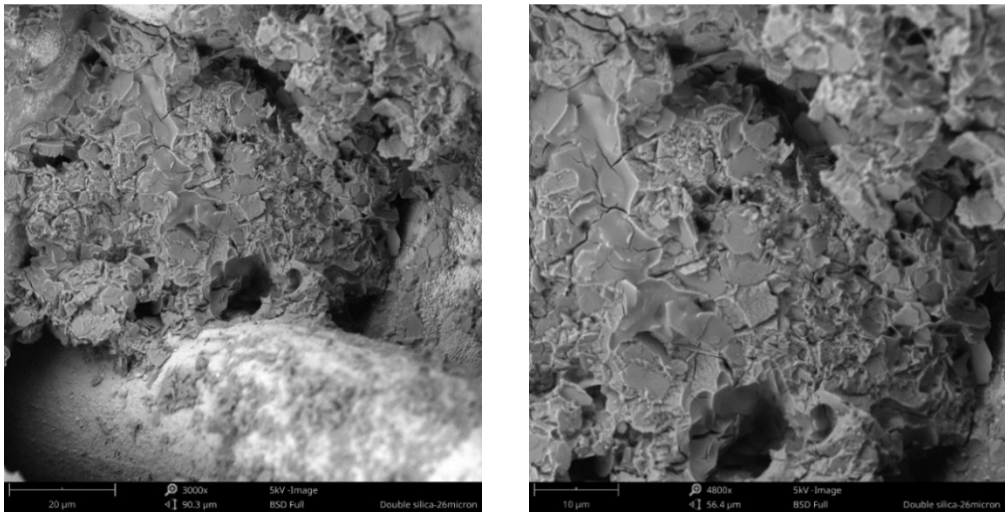

(c) (d)

Figure B- 4: SEM images showing double coated membrane (first layer of 0.078g TAN, 10wt% silica and second layer of 0.0029g TAN and 5wt% silica) on 26µm stainless-steel mesh support, recorded at different magnifications (a) 1200x (b) 2000x (c) 3000x (d) 4800x (taken after the filtration of 10 ppm bentonite suspension).

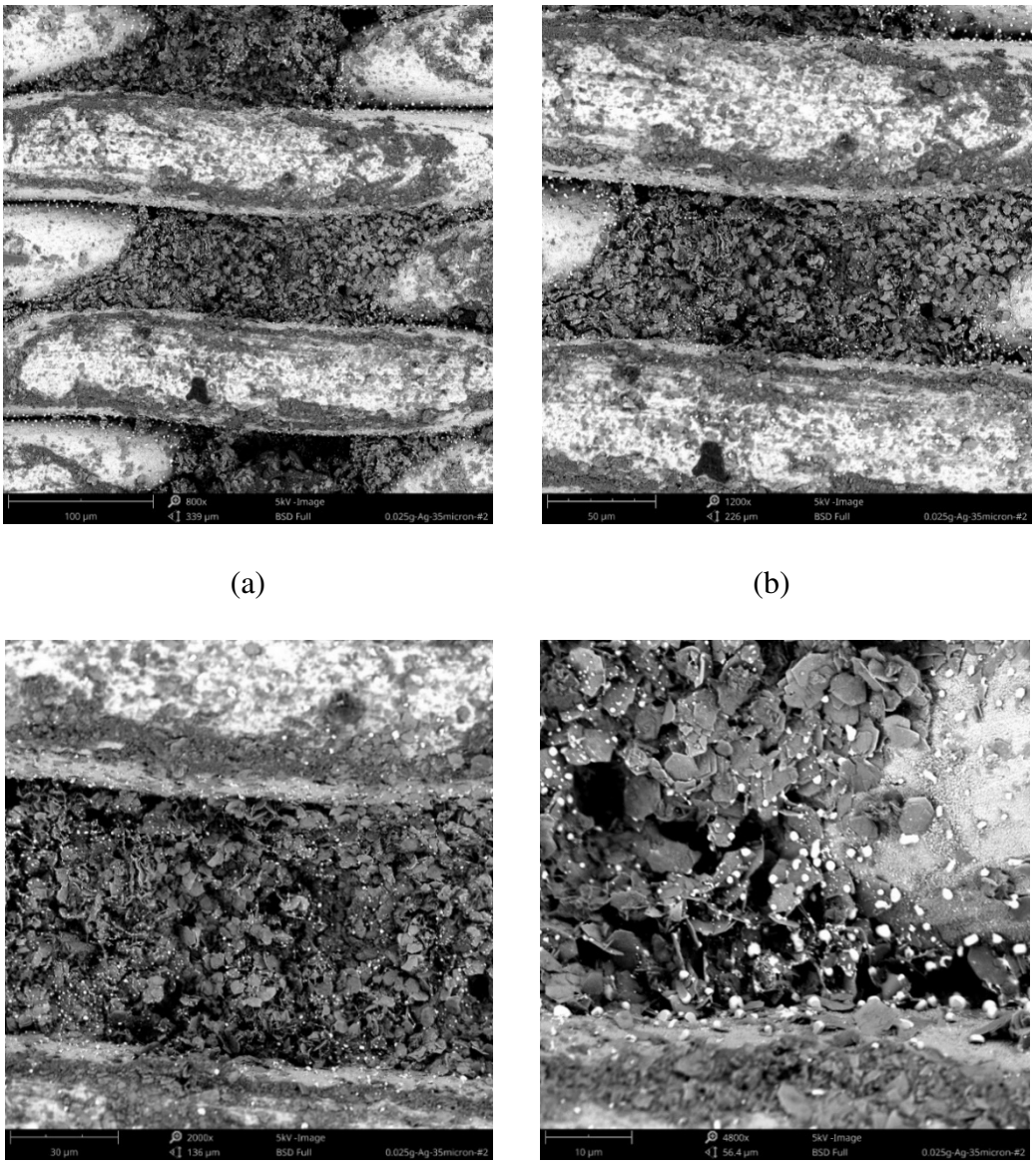

(a) (b)

(c) (d)

Figure B- 5: SEM images showing TAN on 35µm stainless-steel mesh using 0.025g silver as binding agent, recorded at different magnifications (a) 800x (b) 1200x (c) 2000x (d) 4800x (taken after the filtration of 10 ppm bentonite suspension). TAN on 35µm stainless-steel mesh using 0.025g silver as binding agent

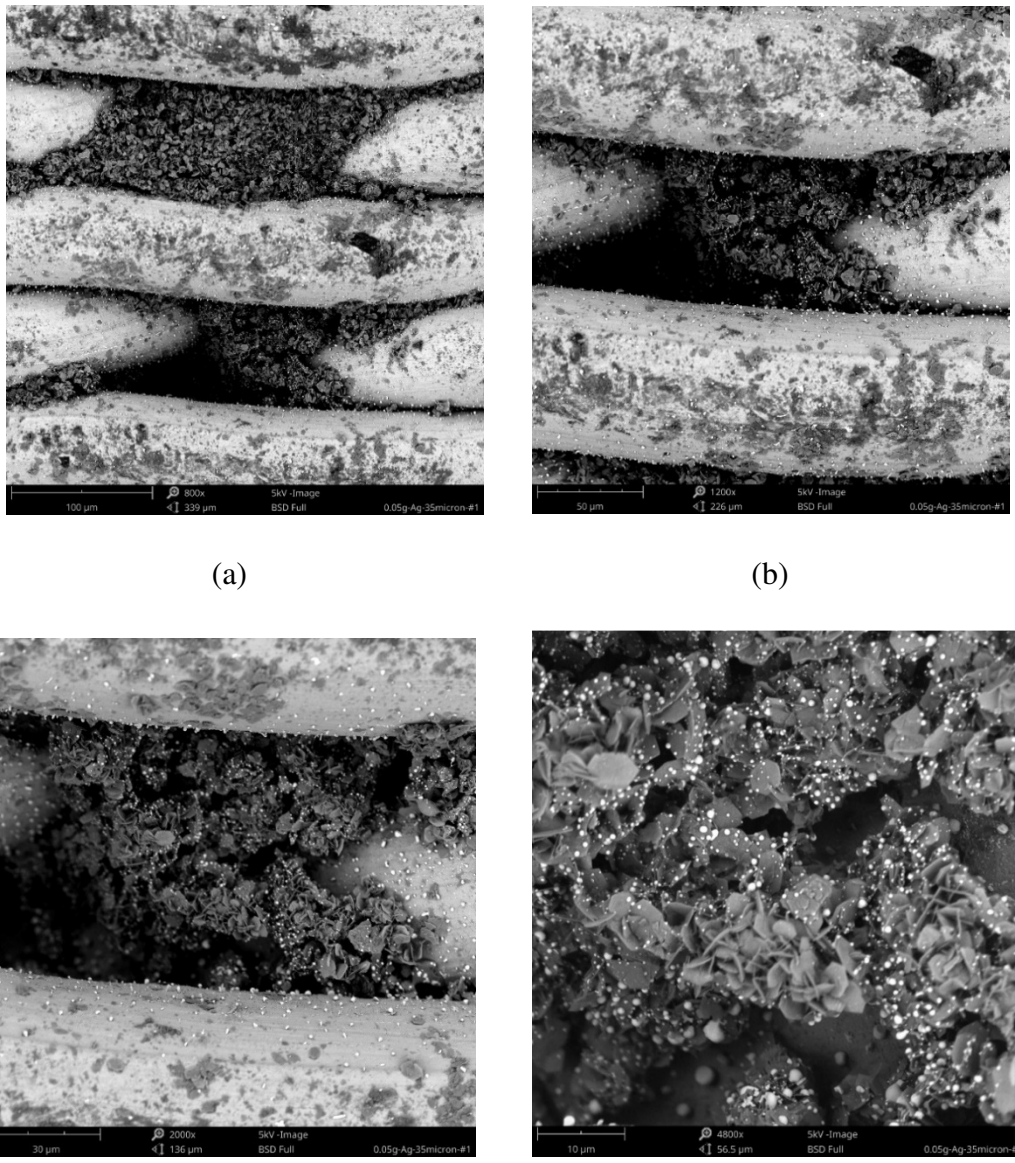

(a) (b)

(c) (d)

Figure B- 6: SEM images showing TAN on 35µm stainless-steel mesh using 0.05g silver as binding agent, recorded at different magnifications (a) 800x (b) 1200x (c) 2000x (d) 4800x (taken after the filtration of 10 ppm bentonite suspension).

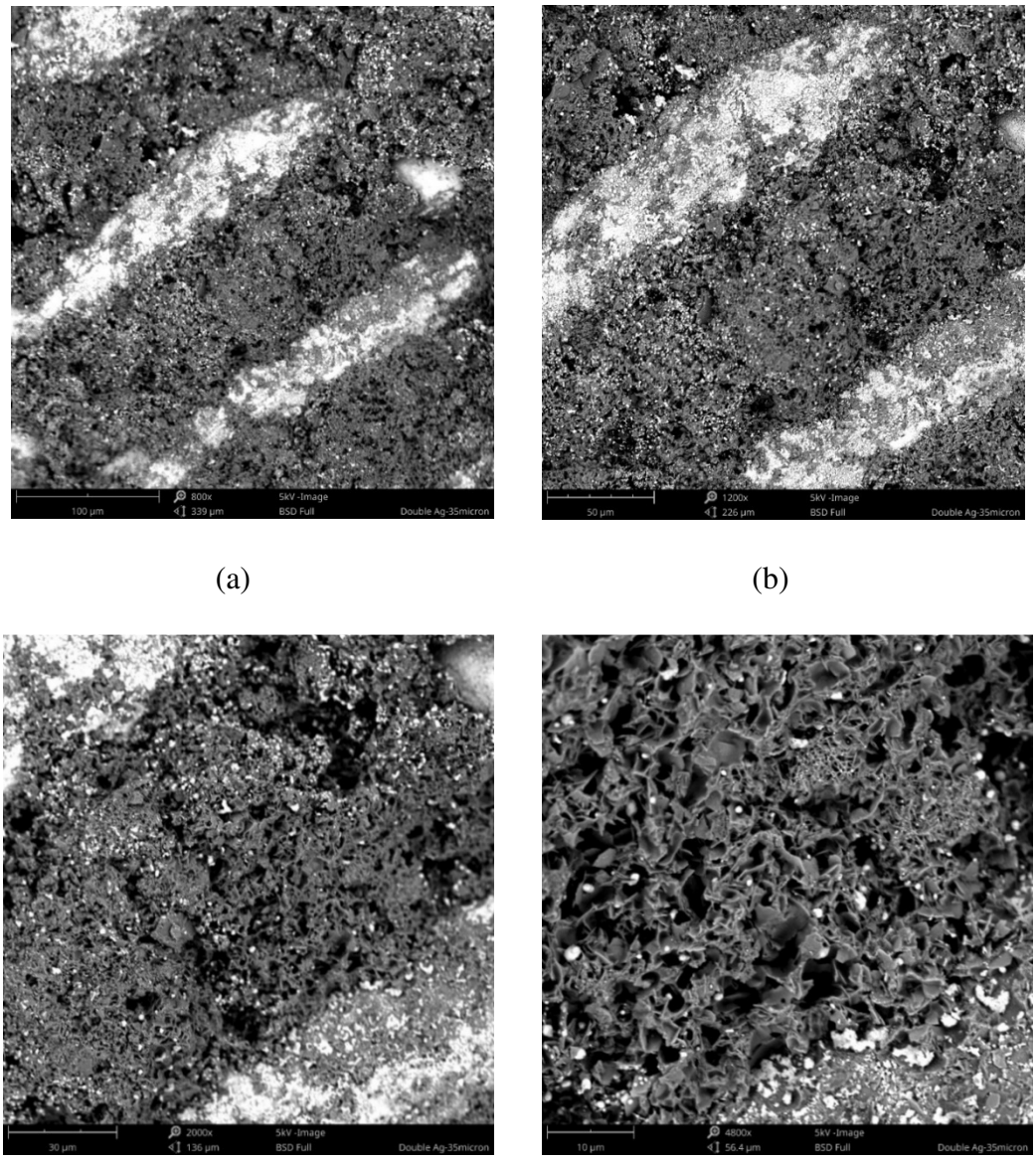

(a) (b)

(c) (d)

Figure B- 7: SEM images showing TAN with double Ag_2O coatings (first layer was with 0.1g TAN and 0.0267g Ag_2O ; second layer was with 0.1g Ag_2O only) on 35µm SS mesh, recorded at different magnifications (a) 800x (b) 1200x (c) 2000x (d) 4800x (taken after the filtration of 10 ppm bentonite suspension).

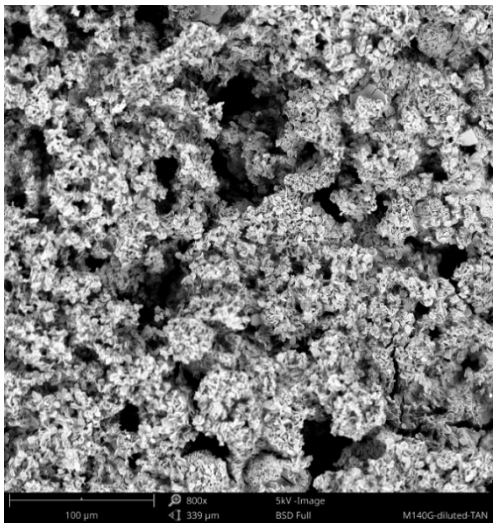

(a)

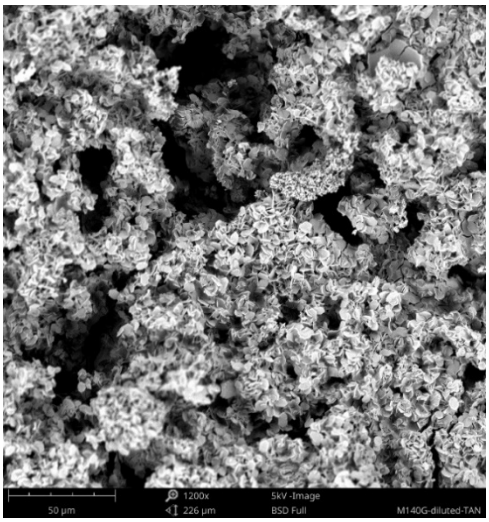

(b)

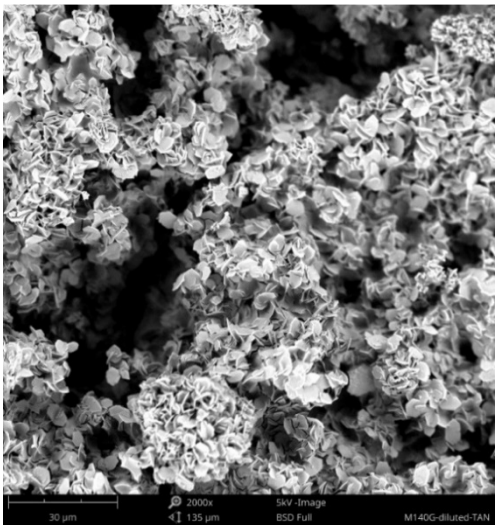

(c)

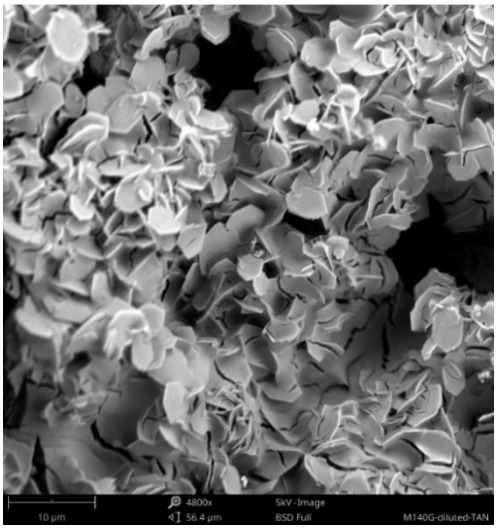

(d)

Figure B- 8: SEM images showing 0.013g TAN and 5wt% silica on a ceramic support, recorded at different magnifications (a) 800x (b) 1200x (c) 2000x (d) 4800x (taken after the filtration of 10 ppm bentonite suspension).

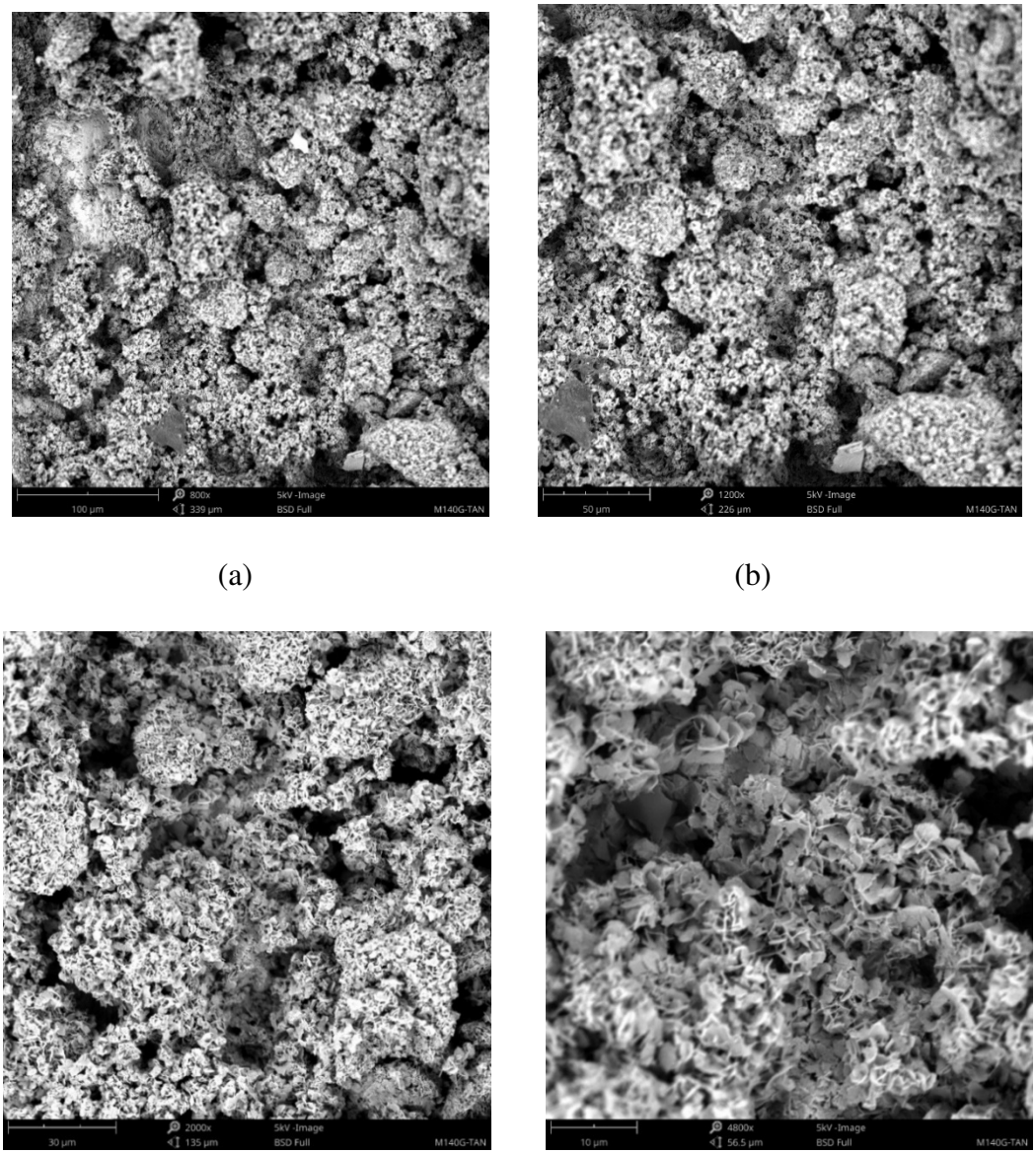

(a) (b)

(c) (d)

Figure B- 9: SEM images showing 0.05g TAN and 10wt% silica on the ceramic support, recorded at different magnifications (a) 800x (b) 1200x (c) 2000x (d) 4800x (taken after the filtration of 10 ppm bentonite suspension).